EPJ A
Hadrons and Nuclei

EPJ.org
your physics journal

Eur. Phys. J. A (2015) **51**: 91 DOI 10.1140/epja/i2015-15091-2

Weakly bound Borromean structures of the exotic ^{6,8}He nuclei through direct reactions on proton

Valérie Lapoux and Nicolas Alamanos

Società Italiana di Fisica

Springer

Eur. Phys. J. A (2015) **51**: 91
DOI 10.1140/epja/i2015-15091-2

THE EUROPEAN PHYSICAL JOURNAL A

Review

Weakly bound Borromean structures of the exotic ^{6,8}He nuclei through direct reactions on proton

Valérie Lapoux[a] and Nicolas Alamanos

CEA, Centre de Saclay, IRFU, Service de Physique Nucléaire, F-91191 Gif-sur-Yvette, France

Received: 13 February 2015 / Revised: 21 May 2015
Published online: 30 July 2015 – © Società Italiana di Fisica / Springer-Verlag 2015
Communicated by U.-G. Meißner

Abstract. The data set of the direct reactions induced by the radioactive nuclei ^{6,8}He can be used as benchmarks to test the validity of the microscopic structure theories. The reactions were analyzed and compared to microscopic calculations including various structure inputs. The interpretation for the structure of He isotopes is compared to the ones proposed via other probes. The consistency of the various data sets and of the reaction analysis using structure models is discussed. The root mean square radii of the matter and neutron densities, and the multipole moments $M_{p,n}$ and $B(E2)$ values are extracted in our approach and compared to the previous experiments and to the theories. From this comparison, we can discuss and point out the microscopic inputs of the models (like correlations, continuum-coupling effects), which are required to reach a consistent understanding for both the radii and the spectroscopy of the nuclei close to the drip-line.

1 Exotic nuclei, questions and observables

In this section, we introduce the context of our study, we recall the main questions presented by the exotic nuclei, and we underline the important achievements obtained these last years in the understanding of the nuclear observables. The progress made in the spectroscopic measurements and in the calculation frameworks, as well as the renewal of nuclear physics concepts applied to finite nuclei give rise to theories with new insights into the evolution of the nuclear shell structure throughout the nuclear chart. In particular, the weakly bound helium isotopes represent test case examples on which complete information can be extracted on the structure and spectroscopy via direct reactions. The comparisons between the experimental results and the most advanced theoretical works will both underline the success of the present theories and give insight onto the further requirements, to reach a complete understanding of the whole set of observables collected on these isotopes. The perspectives offered by this study will be explained in the light of the expected evolution of the theory concepts, including *ab initio* interactions.

The nuclear models are evolving to increase their predictive power on the nuclear properties throughout the nuclear chart, expanding the description from the stable to the weakly bound nuclei and to the unbound nuclear states. Since the first developments of the radioactive beam facilities in the 1980s, opening the path to the discoveries of new isotopes and of the nuclear properties in new regions, the exploration of the characteristics of the very neutron-deficient or -rich nuclei has turned out to be an asset to amplify the variation of the isospin-dependent terms of the nuclear interaction and to probe the evolution of the nuclear properties along extended isotopic chains.

By going from the valley of stability to more and more neutron-deficient, or more and more neutron-rich isotopes we reach nuclei less and less bound —up to the limit of binding with respect to the nuclear interaction. The boundary limits of existence on the nuclear chart are the proton and neutron drip-lines defined by the last bound neutron-deficient and neutron-rich nuclei, respectively. In 2013, experimentally, the limit of the proton drip-line is determined up to $Z = 91$ (protactinium), while for the neutron drip-line it is only up to $Z = 8$, with the last bound oxygen isotope at $N = 16$, that is ^{24}O. Theoretically, there is at present no unique determination of the location of the drip-lines. The discrepancies between the calculations result both from the lack of knowledge of the form of the nuclear interaction at play between the nucleons inside the nuclear edifice, and to the complexity of the many-body treatment of the nucleus, seen as a set of nucleons ruled by quantum mechanics and interacting by the exchange of virtual particles, like the meson first introduced by Yukawa to explain the nuclear binding [1]. The nuclei at the limit of the nuclear binding, with large

[a] e-mail: vlapoux@cea.fr

ratio N/Z compared to their stable isotopes, may have new structures and properties qualified as "exotic":

- At large neutron numbers, sizes may be different from what is expected from the short range of the nuclear force and correlations play an important role,
- The decay to cluster states is favoured;
- Proton and neutron fluids may behave differently in terms of excitation, density distributions;
- Phenomena related to the halo or neutron-skin structures of the light nuclei can be shown. For instance, the one-neutron halo in ^{11}Be, or the 2 neutron-halo found in ^{6}He [2,3], and in ^{11}Li [4–6] correspond to the probability to find one or 2 valence neutrons at large distances (few fm) from the core nucleus $A-2$; this is large compared to the short-range of the nuclear interaction ($\simeq 1.2$ fm).
- In contrast with the shell closures and magic numbers well established in the valley of stability, which were the foundations on which the shell model was built [7], the usual shell structures associated to the standard magic numbers $N = 2$, 8, 20, 28, 50 and 82 may not be observed anymore; new local shell structures associated to new magic number may emerge like at $N = 16$ [8,9], for which the role played by the spin-isopin term of the nuclear force was discussed.

These exotic nuclei are changing the normal rules of our text books of nuclear physics. During these last 30 years, the interpretations of the data collected using radioactive beams have given rise to a renewed vision of the shell model picture and more generally of the correlations at play in the nuclear edifices. The various properties of the "exotic" nuclear structures, encountered in the region of the light neutron-rich nuclei —like haloes or neutron-skins, the change of standard shell ordering— were attributed to the interplay between mean field and correlations, cluster and shell structure. In 1968, Ikeda suggested that clusters fragments constituted by α particles could be found in the light stable nuclei for high enough excitation energies [10], in the vicinity of the fragment emission thresholds. For instance, one of the most studied cluster state, both experimentally and theoretically, was the three α cluster state of ^{12}C located at energy 7.27 MeV [11]. The "Ikeda-diagram" he built [10] was established on the mass excess of the nuclei. In the light weakly bound nuclei, due to the weaker excitation energies a new diagram was proposed, with cluster states predicted for stable and radioactive nuclei, following the new scheme of the Von Oertzen-Ikeda's rule [12, 13]. These approaches based on the alpha-cluster correlations [14] gave a comprehensive view of the behaviour of the cluster structures explored in the exotic nuclei [11], as a function of the decreasing binding energy when approaching the drip-lines.

However, to calculate the evolution of the binding and excitation energies towards the drip-line, and to understand the structure of the exotic nuclei, the original nuclear theory concepts have been deeply reexamined. This has led to the developments of more complete theories able to explain the various aspects (spectroscopy, correlations) of the unusual structures discovered in the exotic nuclei: amongst the most challenging effects which are required to reach a deeper understanding of the phenomena, we can underline i) the three-nucleon forces ($3NF$s) and ii) the continuum effects as striking recent exemples of the successful implementation of fundamental terms and treatments in the nuclear models, respectively, giving rise to a substantial increase of our understanding of the microscopic description of the nuclear structure.

The $3NF$s were originally discussed in ref. [15] as coming from a virtual excitation process implying 3 nucleons, seen as composite particles. We can highlight the following cases showing the impact of the $3NF$ to explain the observables collected on the exotic nuclei, and in particular the structure evolution towards to the drip-lines:

- to account for the location of the experimental drip-line in the oxygen isotopes, it was shown that the contribution of the $3N$ forces was needed; the $3NF$s derived from chiral Effective Field Theory (EFT) have been recently implemented within *ab initio* shell model calculations [16], Coupled-cluster theory [17], calculations with extended valence space [18];
- phenomenologically, the importance of the $3NF$s was shown previously within the calculations using the nuclear interaction deduced from the free NN scattering [19–21]; it was shown that the $3NF$ contributions were needed to reproduce the binding energies and the spectroscopy of the light nuclei;
- the impact of the $3NF$ is also considered as a key to explain the evolution of the shell structure and of the magic numbers [16,18]; it was also shown to be strongly influenced by the $3NF$ contributions within *ab initio* many-body calculations [22] using the $2N$ and $3N$ interactions obtained from the chiral EFT framework;
- in the spectra of the light nuclei (like ^{10}B and ^{13}C) it was shown that the spin-orbit splitting and the spin sequence of the low-lying states could be understood within the *ab initio* No core Shell Model approach using the chiral NN and $3N$ interactions [23].

For the exotic nuclei with low particle threshold (S_n or $S_p \simeq 0$), the probability to have excitations to the continuum states is large compared to the case of the stable nuclei (*e.g.*, S_n or $S_p \simeq 8$ MeV); the spectroscopy, the structure and the reaction observables may be deeply modified by these continuum-coupling (CC) effects. To treat explicitly the coupling to continuum, resonant and scattering states [24] in the calculations of the low-lying spectroscopy of the exotic nuclei, several theories have been developed like the Gamow Shell Model (GSM) [25–27].

1.1 Questions

The location of the experimental drip-lines and the observation of the exotic structure are stringent tests for the theories. The related questions are: how to explain microscopically the evolution of the binding energies and of the shell gaps as the neutron number evolves? How to describe microscopically the properties of nuclei close to the drip-line? The exotic nuclei have weak binding energies producing diffuse nuclear structures and nuclear states close

to the continuum. How to determine precisely the binding energies and to deduce the limit of existence? Moreover, in the case of the lightest nuclei ($A < 12$), the small number of nucleons offers the numerical possibility to make extensive tests of the theories in *ab initio* frameworks, using microscopic interactions and many-body methods. In this spirit, it can be said that the light exotic nuclei represent a laboratory for the exploration of the nuclear forces, in the case of the neutron-rich nuclear matter at low density.

Amongst the species of the nuclear chart, the isotopic chain of the helium nuclei offers benchmark data to test the nuclear theories and to check their abilities to reproduce the weak-binding energies and the corresponding structure properties. ^{6}He and ^{8}He can be considered as very unique test nuclei for our understanding of the nuclear interactions:

- they are extreme cases of the nuclear binding and isospin ($N/Z = 2$ and 3); and their properties may give insight on the nuclear interactions at play in the low-density neutron-rich nuclear matter;
- they differ by 2 neutrons however their matter rms radii are similar, which constitutes a stringent test for the understanding of the role of the pairing correlations in the neutron-rich systems;
- the various aspects of the nuclear modelling can be tested in these few-body systems, like the interplay between correlations, cluster and shell-model;
- they have no bound excited state and low-lying resonances. Due to the low threshold energies, the resonant and scattering states are close to the ground state, the treatment of the continuum effects is an additional challenging task for the nuclear theories;
- the various structure and spectroscopic aspects can be probed through the reactions induced by the radioactive beams of ^{6,8}He in various energy regime allowing us to probe several domains of the wave functions.

There is a complex subtle interplay between correlation effects producing the sequence of ^{6,8}He slightly bound, with ^{5,7}He being unbound: how to give an overall description of the ground and excited state properties of these nuclei; how to be able to calculate the direct reactions induced by ^{6,8}He beams?

To answer to these questions, we will include in our analysis and discussions the whole nuclear data set collected from direct reactions of the ^{6,8}He nuclei on proton. We will consider the new data sets, provided not only for the excited states but also for the angular distributions of the elastic scattering and transfer on proton target. The experimental studies for ^{6,8}He were extended to reveal new aspects of the spectroscopy and of the wave functions of these nuclei. The improvement of the quality of the data in terms of granularity, of the extension of the angular range, and of the resolution have given new information on these nuclei. Moreover, the data set were completed and other energy regimes were accessible for the $(\mathrm{p}, \mathrm{p}')$ studies and the one and 2n-transfer reactions. We now have an impressive complete data set in terms of angles, energies and variety for direct reactions on the proton target. We can both check the consistency of the data set and the validity of the nuclear models used for the interpretation, and explore the structure of ^{6,8}He within microscopic reaction and potential frameworks, We can compare the density inputs provided by the microscopic structure theories, confront the interpretation. Finally we will determine the characteristics of the structure and spectroscopy of the He nuclei, and discuss the main microscopic inputs needed for a good description within the nuclear models. The questions raised by these nuclei are presented in sect. 1.1, and the observables considered for the test cases are given in sects. 2–2.4. In this article, the structure of the neutron-rich ^{6,8}He nuclei will be discussed and taken as a benchmark for the nuclear structure and reaction models, the observables will be compared, via a reaction model, to the theoretical calculations presented in sect. 3. We will select the microscopic nuclear structure models which include as much as possible the effects identified as crucial for the understanding of the drip-line exotic nuclei, like three-body forces and continuum-coupling effects. Experimentally, one of the simplest process to investigate the nuclear properties of the low-lying spectroscopy (for states at excitation energies typically below 10 MeV) is to measure direct reaction observables on a proton target using radioactive beams, this will be presented in sect. 4. This guarantees that the reaction data set is collected using 1) a well-defined probe and structureless target, in our scale of incident energies up to $100\,A \cdot$ MeV and 2) that the mechanism corresponds to direct nuclear reactions on proton for which a microscopic framework can be developed for the interpretation and can provide a full understanding both of the structure and of the reaction probabilities, as we show in sect. 4. The new structure properties can be investigated by proton elastic and inelastic scattering data, provided we take into account the effects due to coupling to continuum and to the main contributions of reaction channels in the reaction framework [28].

In sects. 5 and 6, we present the reaction studies done to investigate the structure of ^{6,8}He, and the consistency of the analysis is examined by checking the origin of the coupling effects due to reaction channels other than $(\mathrm{p}, \mathrm{p}')$, like the (p,d) and (p,t) transfer reactions. We confront the direct reaction data with the recent microscopic structure calculations, which do not limit *a priori* the degrees of freedom and the many-body correlations of the nucleons forming the nucleus.

1.2 Borromean structures of the helium nuclei

^{6}He and ^{8}He are very weakly bound nuclei, with one-neutron separation energy S_n well below the mean 8 MeV nucleon separation energy value of the stable nuclei; the 2n separation energies $S_{2\mathrm{n}}$ are 973 keV [29–32] and 2.1 MeV [31–33], respectively. A picture for ^{6,8}He was emerging from the interaction σ_I and reaction σ_R cross sections measurements done in the 80–90 s [2,4]. The Helium chain is particularly interesting with the sequence of odd unbound and even weakly bound isotopes, ^{6,8}He. These two isotopes are said to be "Borromean", as a reference to the emblem of the Borromeo family with three

rings, interlocked in such a way that, if one is removed, the other two are not linked anymore. This property is also found in other drip-line light nuclei such as ^{11}Li, ^{14}Be. Starting from the tightly bound stable alpha particle, adding one neutron, there is the unbound ^{5}He, with one more, it produces the ^{6}He "Borromean" nucleus with a half-life of $T_{1/2} = 807$ ms [29,31,32], none of its binary subsystem (n + n or α + n) is bound but the 3-body correlations α + n + n produce a weakly bound structure; then ^{7}He is not bound, With one neutron more, another Borromean structure is produced by the nuclear correlations: ^{8}He ($T_{1/2} = 119$ ms) [30,33], which has the largest ratio $N/Z = 3$ amongst the known nuclei. It is the last bound He isotope, however it is more bound than ^{6}He.

From the interpretation of the σ_I data [2] within the Glauber model [34], it was found that the matter root mean square (rms) radii for ^{6,8}He were equal to 2.48(3) and 2.52(3) fm [35], respectively, in contrast with the standard evolution law: $r_o A^{1/3}$ (with r_o ranging from 1.1 to 1.2, fixed in mass regions of the nuclear table), observed in the stable nuclei. These large spatial extensions found also in ^{9,11}Li and ^{12,14}Be nuclei [35] were seen as indications of a more dilute nuclear matter than in the case of the stable isotopes. The matter rms radii found for the light nuclei were reevaluated afterwards [36], and even found larger using comparison with renewed reaction calculations or using other probes, as will be discussed in sect. 3.2. This large enhancement of the matter rms radii with increasing mass number was interpreted as due to the spatial extension of the neutron densities: the formation of a neutron "halo" with respect to the nuclear core is a process ruled by quantum mechanics and it can be easily interpreted as a phenomenon directly produced by the weak binding energies of the valence neutrons, allowing the wave functions to extend far from the core potential [37,38]: in the case of ^{6}He, the "halo" nucleus can be described as an α core with two neutrons, having a high probability of being far apart from the core.

The definitions and conditions of occurrence for halo and neutron-skin were discussed theoretically in refs. [39, 40], with criteria on the radii and on the binding potentials. Neutron-halos are associated to states for which the wave function of the nucleus can be decomposed with one or a few neutrons decoupled from the other remaining particles forming the core; the large spatial extension corresponds to a large probability (> 50%), for these particles, to be outside the binding potential [39]. It was shown [40] that the halo formation was associated to very low values of the total excitation energy with small binding energy of the halo state. As can be seen in fig. 1, for radii above 3 fm, the ^{6,8}He densities, compared to the ^{4}He one, present two kinds of nuclear extension: for ^{6}He the halo density extends at large radii, this tail corresponds to the significant probability of finding one or two neutrons outside the core. In ^{8}He, the neutron-skin density extension involves 4 neutrons and the density is larger than the ^{6}He one for radii up to 5.4 fm but rapidly decreases for $r > 5.4$ fm. The neutron-skin thickness is defined as: $\Delta R = r_n - r_p$ with r_n, r_p, the neutron and proton density rms radii, respectively. For the lightest nuclei, stable or close to stability

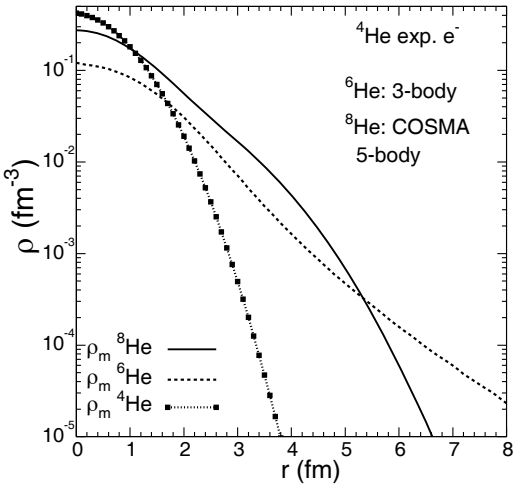

Fig. 1. Comparison of the matter densities of the ^{4,6,8}He isotopes. The ^{4}He density is the experimental one (deduced from electron scattering) and the ^{6,8}He densities are obtained from the few-body calculations discussed in the text.

this value remains < 0.1 fm; for stable medium-mass or heavy nuclei, the value is found between 0.1 and 0.3 fm. For instance, in ^{208}Pb (N-Z = 44) the value deduced from comparison between theory and experiment is found around 0.16 fm [41][1]. The neutron-halo or skin in ^{6,8}He corresponds to $\Delta R > 0.7$ fm [48] (more than 10% of the value of their rms matter radius r_m).

The small separation energies and the large matter rms radii of the ^{6,8}He have triggered the development of the few-body models with He systems built upon an "α" inert core, actually a core formed by 2 protons and 2 neutrons, with similar quantum numbers $[\nu(2s)^2\mu(2s)^2]$ as the ^{4}He particle. In these models, ^{6,8}He are found to develop large spatial extensions of their neutron distributions with 2 and 4 neutrons respectively, surrounding the "α" core, and producing a halo in the case of ^{6}He [38,42]. These pictures were successful to explain a category of phenomena like break-up reactions and the observed parallel momenta [3]. For ^{6}He, amongst the various sets of 3-body calculations presented in ref. [36], if we select the one corresponding to the S_{2n} energy closer to the experimental value (density denoted as "$fc6$" below), the matter rms radius is of 2.53 fm. Within the 5-body α + 4n *COSMA* (Cluster Orbital Shell Model A) model [43], 4 valence neutrons occupying a full $1p_{3/2}$ subshell is assumed for ^{8}He and the

[1] The value is 0.16 ± 0.042 fm, obtained from the study of the antianalogue Giant Dipole resonance (AGDR) deduced experimentally from the inelastic scattering. It was compared to the value obtained via the experiment of *Parity Violation in Electron Scattering* (PREX), where r_n was deduced through the measurement of the parity-violating asymmetry in the elastic scattering of polarized electrons from ^{208}Pb. For stable nuclei, it is possible to use this method to deduce the r_n value. The PREX and AGDR results are consistent within error bars, see [41], and references therein.

4-neutron separation energy S_{4n} is adjusted to the experimental value (3.1 MeV). This pure $(1p_{3/2})^4$ configuration produces the neutron-skin; the corresponding matter density has a rms radius of 2.52 fm. For comparison, the matter rms radius value for the stable nucleus ^{12}C, having twice the number of nucleons of ^{6}He, was deduced from the charge rms radius of 2.471(6) fm [44,45]: $r_m \simeq 2.3$ fm [46]. The matter density for ^{4}He is deduced assuming a Gaussian function density, with the proton density obtained from the charge density extracted from the electron scattering distributions [44,45]. These charge/matter densities are considered as experimental densities, the rms radii for the charge distributions is of 1.676(8) fm and of 1.46 fm for the matter density [47]. In fig. 1, the matter densities for ^{4,6,8}He are presented: the experimental one for the alpha particle; the model distributions for ^{6,8}He, obtained from the calculations assuming the structures of the 3 (2n-halo) or 5-body (neutron-skin of the *COSMA* model), respectively, based on the "alpha" core.

The pictures given initially for the halo and neutron-skin nuclei were mainly established on the assumptions of an inert core and with simplified correlations. However, the validity of the core assumption was discussed in ref. [48], using combined measurement of cross sections for the ^{4,6,8}He nuclei and for the 2 and 4 neutron removal cross sections from ^{6,8}He: they were shown to give good insight onto the neutron-skin in ^{6,8}He, applying the relationship between σ_{-2n} and σ_I; for ^{8}He, it was shown that ^{6}He could not be considered as the core nucleus. The Glauber theory for loosely bound nuclei was developed in the theory work done in ref. [49] for ^{11}Li and it was also applied to ^{6,8}He in ref. [50].

At present, with the new dataset collected with better experimental conditions (resolutions, angular range and statistics), the initial few-body structure models are oftenly found too limited to explain the characteristics related to the low-lying spectroscopy and to the many-body correlations. Another scenarios for the production of the halo or neutron-skin structures in ^{6,8}He are now proposed within various microscopic frameworks, involving also it *ab initio* interactions, this will be explained in sect. 8.1. New extended data to probe the He structure are also available to test the validity of the nuclear models and to understand the neutron correlations in the exotic nuclei.

2 Observables and probes

If we wish to have an "identity card" of the nucleus of interest, we have to consider the data available to obtain the bulk nuclear properties:

- The lifetime from Doppler time of flight techniques for bound states; the half-life, obtained via beta-decay measurements.
- The binding energies and its one- and two-neutron separation energies, obtained from the mass measurements done by time-of-flight techniques, using ion traps, storage rings or, for nuclear masses far from stability, with cyclotrons or high-resolution spectrometers [51].
- The nuclear sizes like charge and matter radii, which can be obtained from laser measurements and proton elastic scattering or reaction cross sections, respectively.
- The nucleon configurations, deduced from the studies of wave function (wf) overlaps between the A nucleus and the neighbor ($A-1$ and $A+1$) isotopes or isotones; these configurations can be studied using the one-nucleon transfer reactions from the nucleus of interest or populating states in this nucleus, so as to deduce if possible the spin and parity of these states.

Via the combination of various reaction data, our aim is to obtain the characteristics (like the density profile, the moments of the distributions) of the spatial repartition of the nucleons of the nuclei, namely the densities, ground state (gs) and transition densities to the first excited states. The goal is to compare them to the structure models. We first define these quantities, and give an overview the various interaction fields which can be used to probe the nuclear densities. This leads us to select and discuss the direct reactions on proton target. In this section, we will indicate how we carry out the structure studies, by measuring the direct reactions on proton target in inverse kinematics. To discriminate between the various models, we rely on the following observables: the energy excitation spectra of the nuclei produced in the exit reaction channels, compared to the spectroscopy of low-lying states proposed by the theories, and the corresponding angular differential cross sections, compared to the reaction calculations done using the microscopic densities.

2.1 Wave functions, nuclear densities and inelastic form factors

With Ψ_{gs} the gs wf, the radial gs density is given as: $\rho(r) = \langle \Psi_{gs} | \delta(\vec{r} - \vec{r'}) | \Psi_{gs} \rangle$. In general, the proton or neutron transition density between a state Ik to $I'k'$, noted as $\rho^{\tau}_{Ik,I'k'}$ ($N_\tau = Z$ or N, respectively, for $\tau = p$ or n), is defined with:

$$\rho^{\tau}_{Ik,I'k'}(\vec{r}) = \langle \Psi^{\tau}_{Ik}(\zeta) | \sum_{i=1}^{N_\tau} \delta(\vec{r} - \vec{r_i}) | \Psi^{\tau}_{I'k'}(\zeta) \rangle. \quad (1)$$

The radial component of the transition density, $\rho^{\tau(\lambda)}_{I,I'}(\vec{r})$ can be expressed as

$$\rho^{\tau}_{Ik,I'k'} = \sum_{\lambda,\mu=1,1}^{N_\tau} (I'k'\lambda\mu|Ik) \rho^{\tau(\lambda)}_{I,I'}(\vec{r}) Y^*_{\lambda\mu}(\hat{r}). \quad (2)$$

The matrix element of the multipole operator with multipolarity λ is [52, 53]: $M^{(\lambda)}_\tau = \widehat{I} \int \rho^{\tau(\lambda)}_{I,I'}(r) r^{\lambda+2} \mathrm{d}r$. If we note $\rho^{tr}_{fi}(\vec{r})$ the transition density from the states i to f, with the initial and final wfs of the nucleus, Ψ_i and Ψ_f respectively, we can write it as $\rho^{tr}_{fi} = \langle \Psi_f | \delta(\vec{r} - \vec{r'}) | \Psi_i \rangle$, and it may be expressed as an integral form using radial coordinates, with $\vec{r}$ the position of the nucleon with respect to

the center of mass of the nucleus:

$$\rho^{tr}_{fi}(\vec{r}) = A \int \phi^*_f(\vec{r}, \vec{r_2}, \ldots, \vec{r_A})\phi_i(\vec{r}, \vec{r_2}, \ldots, \vec{r_A})\mathrm{d}\vec{r_2} \ldots \mathrm{d}\vec{r_A}. \tag{3}$$

The gs or transition densities (with $\tau = p$ or n) from the 0^+ gs to the first 2^+ state can be given in terms of the operators

$$\rho_{\tau(\lambda=0)}(\vec{r}) = \sum_{i=1}^{N(Z)} \langle 0^+ | \frac{1}{r^2} \delta(\vec{r} - \vec{r_i}) Y_{00}(\widehat{r_i}) | 0^+ \rangle, \tag{4}$$

$$\rho^{0^+ \to 2^+}_{\tau(\lambda=2)}(\vec{r}) = \sum_{i=1}^{N(Z)} \langle 2^+ | \frac{1}{r^2} \delta(\vec{r} - \vec{r_i}) Y_{20}(\widehat{r_i}) | 0^+ \rangle. \tag{5}$$

The $2^+ \to 2^+$ reorientation transition term is defined by replacing in eq. (5) the 0^+ state by 2^+. The matrix elements can be related to the radial transition densities of protons and neutrons. If the proton and neutron transition densities from states i to f are written in terms of radial functions $\rho^{tr}_{n,p}(r)$, respectively, the transition matrix elements M_n and M_p can also be defined as the radial moments of these densities:

$$M_{n,p} = \int \rho^{tr}_{n,p}(r) r^{\lambda+2} \mathrm{d}r, \tag{6}$$

where l is the multipolarity of the transition.

2.2 Coulomb and nuclear excitations

The transition densities for neutrons and protons are defined independently of the probe used to excite the nucleus, so are the transition matrix elements $M_{n,p}$. But the contributions of the protons and of the neutrons to the excitation of the nucleus do depend on the probe, and the transition matrix element M is defined as a linear combination of M_n and M_p:

$$M = b_n M_n + b_p M_p,$$

with b_n et b_p the interaction intensities between the particle probe and the neutrons or the protons of the nucleus. In the case of an excitation via electron scattering, $b_n = 0$ and $b_p = 1$. For a Coulomb excitation, the part of nuclear excitation is weak but *a priori* it cannot be neglected, and it should be taken into account in a complete analysis. Since the NN effective interaction is dominated by the isoscalar channel $^3S_1$, the proton scattering mainly probes the neutron density (and the M_n value); similarly the neutron scattering probes the proton density. Microscopic calculations would give directly the compared strengths of the proton/neutron excitations depending on the energy and density-dependent interaction potentials. From this analysis discussed in sect. 4.2, the set of (M_p, M_n) values can be tested. Table 1 presents the b_n/b_p ratio for various particle probes [54]. With this table, our only purpose is to present the sensitivity of the probes, on the basis of the usual phenomenological models. We can see that the neutron inelastic scattering is more sensitive to the $B(E2)$ value than the proton scattering. This property is an indication that the proton inelastic scattering provides M_n values, while it is difficult to obtain reliable $B(E2)$ values. In the framework of a model with collective vibrations in a nuclear homogeneous fluid, the p and n transition densities are considered as similar (isoscalar mode): $\rho^{tr}_p(r) = (Z/A)f^{tr}(r)$, and $\rho^{tr}_n(r) = (N/A)f^{tr}(r)$ In this case, the M_n and M_p factors are related by the equation: $M_n/M_p = N/Z$. The M_p factor for a J_i to J_f transition is directly related to the corresponding $B(E\lambda)$ transition strengh value. $B(E\lambda)$ is an observable, which can be obtained by an electromagnetic experiment, Coulomb excitation, lifetime measurement. In the case of a stable nucleus, it can be deduced using the electron scattering. We adopt here the following convention for the relationship between $|M_p|$ and $B(E\lambda)$:

$$B(E\lambda, J_i \to J_f) = e^2 \frac{1}{(2J_i + 1)} |M_p(T_z)|^2, \tag{7}$$

with J_i and J_f the spins of the initial and final states, respectively. Similarly a transition strength related to neutron matrix element M_n can be defined. It quantifies the neutron contribution to the excitation, which may be dominated by the nuclear interaction for instance in the case of the $(\mathrm{p}, \mathrm{p}')$ reactions for incident energies between 10 and 50 MeV. The transition matrix elements M_n, M_p can be obtained by combining the measurements of an electromagnetic excitation with the ones using an hadronic probe.

Table 1. Ratio of the intensities of neutron and proton interactions for various interaction fields [54].

Particles	Energy (MeV)	b_n/b_p
Electromagnetic		0
protons	10–50 MeV	3
protons	1 GeV	0.95
neutrons	10–50 MeV	1/3
α	all	1
π^+	160–200 MeV	1/3
π^-	160–200 MeV	3

2.3 Reaction probes

Stable nuclei can form targets: in the twentieth century, their nuclear structure has been obtained through electron and hadron scattering experiments [55]. The charge distributions were obtained from the very well known electromagnetic interaction process through the elastic and inelastic scattering of electrons. The proton gs and transition densities (distributions of the centers of mass of the protons inside the nucleus) were deduced from the measured (e, e') cross sections by unfolding the finite size of the charge distribution of the proton, $\langle r^2 \rangle_P \simeq 0.76\,\mathrm{fm}^2$ [56] ($\simeq 0.88\,\mathrm{fm}^2$ [57] from recent reevaluation) from the charge

distribution of the nucleus. The incident energy of the electron beam determines the radial range which can be probed inside the nucleus. The matter density distributions were deduced [58] by using the following hadronic probes:

- The proton. In the energy regime less than few hundreds of MeV the proton may be considered structureless for the (p, p') scattering analysis.
- The no-spin α particle. For reaction studies we have to take care of its composite nuclear structure.
- The pion, which interacts strongly with the nuclear matter.

From the combination of various probes and energies, a complete mapping of the radial charge [45] and of the matter density distributions of the stable and long-lived nuclei was obtained in terms of global parameterizations or analytical series given in tables. To probe the neutron densities, we select the direct reactions of the nucleus with a proton: it represents a good tool, since, as indicated in table 1, the observed sensitivity to the neutron densities is increased due to the interaction strength of nearly 3, in the energy domain preferably between 10 and 50 MeV. The proton elastic scattering data can be compared to a reaction framework using various assumptions on the neutron densities, to probe the nuclear structure. Various nuclear model calculations can provide the proton and neutron density distributions to be used to generate microscopic proton-nucleus density-dependent interaction potentials. These various potentials are included for reaction calculations of the elastic scattering. In principle, from the comparison to the elastic data, it is possible to discriminate between the various densities, at least with a sensitivity corresponding to a variation of ± 0.1 fm of the matter rms radii for the tested densities. The proton scattering was extensively used to obtain the neutron densities of the stable nuclei. The analysis were done by measuring the angular distributions with a large angular domain and by varying the momentum transfer of the proton projectile, from which it is possible to investigate various spatial ranges of the wave functions. With high statistics, if a large transfer momentum is covered, it is possible to extract accurately from (p, p') data the radial structure of the nucleus, as was done in the case of ^{18}O in ref. [59].

2.4 (p, p') observable for exotic nuclei and sensitivity to the nuclear structure

Far from the valley of stability, the species are short-lived radioactive nuclei and cannot form targets so we need to rely on the simplest probe, protons, used as target in inverse kinematics experiments. Experimentally the difficulty is to work with radioactive beams having lower and lower intensities as moving towards the driplines. For most of the cases, the elastic data set are obtained for a reduced range of energies (since the incident energies are related to the production modes of the exotic nuclei, in-flight fragmentation or isotopic separation on line) chosen so as to maximize the intensities. As a consequence, the data set for one exotic nucleus corresponds to a small range of momentum transfer and this limits the regions of the wf that may be investigated. Moreover, for radioactive beams, generally, the poor statistics do not allow to give precisely the gs and transition densities as a function of the radial coordinate.

Nevertheless, the (p, p') data are a good tool to constrain the structure models proposed for the exotic nuclei: the angular cross sections can be calculated using the microscopic inputs of the gs and transition densities; from the comparison with the data, it is possible to know if the description of the densities is valid and if a change may be needed, for instance, in the modelling of the shell structure. Different scenarios can be investigated, for instance the role of the deformation in the shell ordering, or various core polarization mechanisms, depending on the neutron and proton interactions with the core, the role of the 3-body forces and tensor interactions in the modification of the shell effects, the coupling from gs to excited states, the continuum coupling description, with possible coupling to the resonant, non-resonant, scattering states. During the last twenty years, Coulomb excitation (Coulex) and elastic and inelastic (p, p') scattering were carried out using the radioactive beams, to have insight on the proton and neutron excitations and to study the evolution of the proton and neutron transition probabilities with the isospin degree of freedom.

It is important to note that the reaction data analysis provides a test of the densities but not a direct information. With radioactive beams, through the (p, p') data we have to test both the assumptions on the proton and the neutron densities. We rely on the assumptions made in the nuclear reaction models for the interaction between the probe and the nucleus and we are sensitive only to a part of the radial densities. Other probes may provide complementary observables: for instance, we will discuss in sect. 3.3 the proton rms radius estimated within a 0.02 fm sensitivity from the isotopic shifts measured in the laser spectroscopy recently applied to ^{6,8}He isotopes and reported in refs. [60, 61]. The proton rms radii are used to select the microscopic theories; however, the studies with the proton hadronic probe are also required to bring constraint on the matter densities; in sect. 4.6, we will discuss the sensitivity of the (p,p) scattering to the rms radii and to the nuclear density profile. In the case of the exotic nuclei, we also have to question the reaction framework usually applied for interpretation of the data. We specially need to care about the new reaction effects which may arise from the low threshold energies of the radioactive species: during their interaction with a target, the ground state system can easily couple to excited or continuum states, and these coupling should be considered *a priori* in the reaction formalism, but the theoretical difficulty is to treat accurately the possible reaction and excitation couplings. To overcome this problem, the phenomenological approach consists in reproducing the elastic data to obtain the entrance channel potential. To go beyond phenomenology for these calculations, and to be able to extract unambiguously information on the structure, we would need to consider a more complete reaction

Table 2. Ground-state characteristics with the previous AME2003 [30] and new AME2012 [31, 32] evaluations of the binding energies and the first 2^+ energies for ^{6}He [29] and ^{8}He [33, 63].

A	Mass excess	E_B	S_n	S_{2n}	2^+ E_x, width Γ
	MeV	MeV	MeV	MeV	MeV
^{6}He [30]	−17.595	29.269	1.86	0.972	1.87
[31, 32]	−17.592	29.269	1.71	0.975	0.113(20)
^{8}He [30]	−31.598	31.408	2.57	2.140	3.57 (12)
[31, 32]	−31.609	31.396	2.53	2.13	0.6(2)

formalism involving the description of inelastic and transfer reactions. These questions are explained in sect. 6.4 in the case of the ^{8}He(p, p) and direct reactions studied at low incident energy, 15.7 $A \cdot$ MeV.

3 Observables versus structure models: ground state properties of the He nuclei

In the next subsections, we will give an overview of the *gs* characteristics of the He isotopes known experimentally and compare them to the structure model calculations.

3.1 Binding energies of He: Experiment versus theory

3.1.1 Mass evaluation

The experimental values of the binding and excitation energies are presented in refs. [29, 33]. Recent direct mass measurements for ^{6}He and ^{8}He were reported in ref. [62] and the corresponding value for the binding energy of ^{6}He was found at 4σ compared to the previous evaluations [30]. These values and the particle thresholds from the recent "Atomic Mass Evaluation" AME2012 [31, 32] are given in table 2.

The first excited state 2^+ is at 1.87 MeV for ^{6}He [29] and $\simeq$ 3.6 MeV for ^{8}He [33, 63]. The other excited states found for ^{6,8}He will be discussed in sect. 7.2.

3.1.2 Structure models for light nuclei

First, we recall the context of the nuclear structure models developed during these last 30 years for the structure studies of the light neutron-rich nuclei, before discussing the interpretations proposed by the most recent theories. The exotic nuclei were investigated by a large variety of models, to explore the interplay between many-body correlations, mean-field and cluster effects, and the initial goals were to have insight onto the nuclear interactions, and *in fine* to be able to constrain the nuclear interactions and the models by comparison to the nuclear observables. For instance, the evolution of the binding energies towards the drip-lines has constituted a stringent test for the models. In particular, within the Quantum Monte Carlo (QMC) approaches starting from free NN interactions, it was shown that the $3N$ interactions were needed to have a correct description of the *gs* and first excited states of the light nuclei [21]. To have a description of both structure and spectroscopy of the exotic nuclei, specific models were developed, taking advantage of the small number of correlated nucleons in these nuclear systems. The models developed for light nuclei ($A < 12$) can be classified in categories depending on their assumptions, on their microscopic inputs and on the practical methods of the frameworks: the few-body, cluster with *a priori* on the cluster structure decomposition of the nucleus will be discussed in sect. 3.2; the other ones were developed with no *a priori* on the structure. For the no *a priori* model, no preliminary cluster decomposition is assumed and the calculations are carried out using A-body basis states. Various models were developed, depending on the choice of these basis states which are parity and angular momentum projected Slater determinants of single-particle states:

- The Antisymmetrized Molecular Dynamics (AMD) models, with the wf defined as a Slater determinant of Gaussian-basis wave packet functions [64]. Recent calculations for the study of dineutron correlations in ^{6,8}He were undertaken within the AMD framework [65, 66] and will be discussed in sect. 7.1.
- The Fermionic Molecular Dynamics (FMD) calculations [67, 68], using effective interactions based on the Argonne V18 interaction; within the Unitary Correlation Operator Method (UCOM), the short-range correlations (from central and tensor terms) can be treated explicitly. This approach can provide the rms radii and binding energies in good agreement with the experiment, through calculations with multiconfigurations and the dipole and quadrupole moments as generator coordinates.
- The No-Core Shell Model (NCSM), in contrast with the usual shell model, in this model there is no decomposition between core and valence nucleons, all nucleons are allowed to be active in the nuclear field, this means also that no effective charge is needed to fix the interaction between predefined subsets. Initially, the NCSM calculations were applied to light p-shell nuclei and gave relatively good results for the spectroscopy of the neutron-rich nuclei [69] but the binding energies were generally underestimated within the *ab initio* NCSM using 3NF [70]. To improve the description of the spectroscopy and of the densities [71], new theoretical inputs were developed in this framework, they will be discussed in the next sections.
- Hartree-Fock models including specific correlations. For instance, the wfs of ^{6,8}He were calculated using the same method applied in ref. [72, 73] for the cases of the neutron-halo nuclei ^{11}Li and ^{11}Be, starting from a HF model, with the occupancy probability for the valence neutrons calculated from the shell model. The experimental value S_{2n} is a parameter of this model and it is shown to influence directly the extension of the neutron halo and of the neutron rms radius. The

two-particle correlations were also calculated recently for ^{6}He [74, 75] and ^{8}He [76] by solving the few (respectively 3, 5) body Hamiltonian in the Hartree-Fock-Bogoliubov (HFB) approximation and using a density-dependent contact interaction.
– Hyperspherical Harmonics (HH) method was applied to H and He isotopes in the shell model approach and compared to the experimental values [77]. Using very simple NN interactions, a satisfactory agreement was found between experiment and theory for the binding energies.

Those models used initially effective NN interactions but other microscopic interaction terms were included recently, with the scope to improve the calculated binding energies. Their results, compared to observables, will be discussed in sects. 5 and 6. Another category of frameworks called *ab initio* models take as inputs the nuclear interactions obtained from the free NN scattering data, and they include $3N$ terms adjusted on the nuclear binding energies of the light nuclei. We present these approaches in the next sect. 3.1.3.

3.1.3 Quantum Monte Carlo and GFMC

Theoretical approaches called *ab initio* have been developed to describe the light nucleus from the NN free interactions: *nn* (not directly known), *pp* and *pn*. The *ab initio* assumption is to consider that the nucleus can be described as composites of A-bodies bound by a "free" NN force. A part of the terms used to build the NN interaction are deduced from the scattering data of proton-proton and neutron-proton obtained in various energy domains. The Argonne V_{18}, built in 1995, results from a direct adjustment on 4300 NN data in the Nijmegen-basis. Initially, in this framework, it was possible to describe only the very light nuclei due to the computer power requested to make the full calculations. To understand and to account for the observed spectroscopy of the light nuclei, it was shown that the inclusion of higher-order correlations like 3-body forces was needed. For the $A < 7$ nuclei, QMC calculations were done [78,79], a Variational Monte Carlo (VMC) method was applied with an hamiltonian including the 3-nucleon Urbana IX (UIX) potential and the 2-nucleon V_{18} interaction. To obtain the nuclear spectroscopy, the Green Function Monte Carlo method (GFMC) was developed, combining the wf of the VMC calculations to the propagation in the imaginary time dimension. Today, with the available computational power, the time needed to obtain the configurations of the nuclei limits the calculations up to nuclei of mass $A = 10$ [20]; recent adaptations of the NCSM using *ab initio* nuclear interactions were done and calculations were pushed up to ^{13}C. The experimental binding energies of the light nuclei, particularly the helium isotopes, were underestimated by the initial calculations [78, 79]. To reproduce them, additional correlations were introduced in the model, in the form of a new 3-body interaction [19]. The parameters were expressed with pion-exchange terms and obtained fitting the results of the GFMC calculations on the data set of 17 energies of bound and resonant states (resonances with small width) for nuclei of masses between $A = 3$ and 8. The error of the fit was less than 2%. With these adjusted interaction terms the weak binding energies of the light exotic nuclei were successfully reproduced. However, once the parameters of the 2- and 3-body forces are adjusted, the question is to know whether the hamiltonian is predictive for the spectroscopy of other new states found for the nuclei in the mass range $A < 10$. In ref. [21] the QMC calculations were done with the $2N$ Argonne (AV18) and the $3N$ interactions (either UIX or IL2-Illinois), the results provided by this technique will be compared to the data set of the Helium isotopes in sect. 7.2.

In the case of QMC calculations [20] using $2N$ and $3N$ interactions, the excellent agreement obtained for the spectroscopy of the light nuclei does not seem to give new insight and predictive power for the binding energies outside from the regions of higher A. This is due to the fact that the representations of the $3NF$ terms were mainly deduced phenomenologically by considering a set of nuclear data (including binding energies and first excited states of the light nuclei).

The model ambiguities could be found not only in the definition of the $3N$ terms but also in the uncertainties in the expression given to the $2N$ interaction. Calculating the binding energy *ab initio* remains a difficult task. Recent attempts were done with improved 3-body forces leading to a significant improvement over the earlier descriptions. A true derivation of the nuclear interaction from the first principles was lacking in the various model approaches initially developed for the light exotic nuclei. At present it appears that, with the recent developments of the chiral EFT calculations [80], the light nuclei could actually represent the benchmark for the microscopic calculations: the chiral EFT interactions can be expressed in terms of NN to the N^{3}LO and $3N$ to the N^{2}LO; all the parameters can be constrained using only few-nucleon data. Compared to the other structure models or the *ab initio* QMC, the chiral EFT represents a model-independent approach to nuclear interactions. Within chiral EFT calculations the spectroscopy of ^{23}O was studied in ref. [18], and it was found that, by including the $3NF$ contributions, the spectrum is significantly improved in comparison with the experiment. It has to be underlined that it is the comparison between experiments and theories, and the need to explain the weak binding energies of Helium chain or the anomaly of the O chain —with ^{24}O weakly bound and ^{28}O unbound— which has triggered crucial changes in the microscopic models. For instance, as discussed previously, the NCSM framework was initially developed for the light nuclei of the p-shell [69]. In this model, the sensitivity to the effective interactions can also be studied, and various types of effective $2N$ interactions can be tested, or the $2N$ and $3N$ interactions [81–83], derived from the ones proposed within the *ab initio* framework. In table 3 we compare experimental $|E_B|$ to the calculated energies given by the models discussed in sect. 3.1.2 and by: i) the QMC method noted QMC04 using the AV18/IL2 hamiltonians, or ii) the NCSM with several sets of interactions, one (that we note below as "V3eff") the combination of Argonne

Table 3. Experimental [31–33, 62] *versus* calculated binding energies (in MeV) $|E_B|$ of the ^{4,6,8}He *gs*, given by the models discussed in the text and noted below with specific labels: QMC04 for the GFMC calculations using the AV18/IL2 hamiltonians in [21]; and the NCSM calculations NCSM$_{v3\text{eff}}$ using $V_{3\text{eff}}$ interaction ($6\hbar\omega$, 14 MeV for ^{6}He; $4\hbar\omega$ for ^{8}He, 13 MeV) [70], NCSM$_{cd}$ and NCSM$_{inoy}$ done with with CD Bonn and TNI interactions [84], respectively.

	Exp	QMC04	NCSM $_{v3\text{eff}}$	NCSM $_{cd}$	NCSM $_{inoy}$
^{4}He	28.296	28.37	–	26.16	29.10
^{6}He	29.269	29.28	28.19	26.9	29.38
^{8}He	31.396	31.72	22.87	26.0	30.30

NN AV8' and TNI Tucson-Melbourne TM'99 [70, 71], or iii) NCSM with CD Bonn 2000 realistic NN interactions or iv) the INOY including TNI force [84]. With the TNI force INOY ^{8}He is found bound, contrarily to the calculations done using the CD Bonn, but $|E_B|$ (^{4}He) is overestimated (with r_m^α found too small). The NCSM is based on a large-basis Hamiltonian diagonalization, but the extensions of the wfs in the NSCM model are limited by the size of the space allowed for the calculations.

However, the light nuclei close to the drip-lines have low particle threshold energies and few bound states. Several aspects cannot be merely explained by using the standard cluster, shell model or mean-field approaches even with sophisticated interactions, or adjusted correlations. The treatment of the continuum states has to be discussed.

3.1.4 Models including continuum treatment

To reach a more complete understanding of the nuclear systems close to the dripline, and to describe the structure of the *gs* and of the resonances, other theoretical approaches have to be considered, which combine complex aspects mixing discrete, continuum and scattering states. The need to incorporate on the same footing both the discrete and the continuum states in the calculations has triggered important renewal or developments in the models treating explicitly the continuum coupling (CC) of bound and scattering states [24]. These models calculate the excited states in the complex plane, using various techniques. In particular, to discuss the resonant excited states of ^{6,8}He, we focus on the following CC models:

- the Continuum Shell Model (CSM) [85], where two (correlated) particles are treated in the continuum;
- the Gamow Shell Model (GSM) framework, described in refs. [25–27] with many-body treatment of particles in the continuum. Recently these calculations were applied to ^{6,8}He using effective interaction techniques [86] and a finite-range modified Minnesota interaction [87];
- the Complex Orbital Shell Model (COSM) using the Complex Scaling Method (denoted below CScM) applied to ^{6,7}He [88, 89] and to ^{8}He [90];

Table 4. Calculated energies (*in MeV*) for the *gs* and for the first 2^+ state of ^{6,8}He given by the models discussed in the text and noted below with specific labels: QMC04 for the GFMC calculations, *GSM03, 05, 10 and 11* for Gamow Shell Model calculations.

Model	Ref.	^{6}He		^{8}He	
		S_{2n}	$E_x(2^+)$	S_{2n}	$E_x(2^+)$
FB	[42]	0.93	1.9	–	–
HF corr	[72]	0.93	1.91	2.34	–
HFB FB	[74, 76]	0.93	1.91	2.34	2.22
AMD-m56	[65]	1.1	1.40	2.0	3.9
FMD	[67]	0.7	–	2.6	–
QMC04	[21]	0.910	1.98	2.44	4.72
CSM	[85]	1.38	1.91	2.21	3.78
COSM	[88]	0.974	1.8	–	–
COSM-Cscm	[90]	0.790	2.1	2.15	–
TOSM MN	[91]	1.0	2.8	3.0	3.8
GSM03	[26]	0.974	2.3	0.7	3.6
GSM05	[86]	1.0	2.1	–	–
GSM10	[27]	0.974	1.797	–	–
GSM11	[87]	0.97	1.82	2.1	–

- the Tensor Orbital Shell Model (TOSM) Method [91] using UCOM (and AV8' bare NN interaction) was applied to the spectroscopy of ^{5,6,7,8}He; but it underbinds ^{6,8}He by more than 5 MeV; the TOSM applied using the 2-body Minnesota (MN) interaction reproduces the binding energy of ^{4}He and of ^{6}He, and overbinds ^{8}He;
- the NCSM was recently improved to treat explicitly the CC effects, by using the Resonating Group Model (RGM) formalism. We denote below this model by "NCSMc" [92].

Table 4 gives an overview of the binding energies and 2^+ states calculated within the different frameworks discussed above. The model calculations will be discussed in sect. 7.2 in comparison with the experimental spectra.

3.2 Matter rms radii from experiments and few-body analysis

3.2.1 Interaction and reaction cross sections

The matter r_m were obtained via model-dependent analysis of the interaction cross sections, σ_I measured at high incident energies by Tanihata *et al.* [2, 4] (see table 5).

The interpretation was based upon the Glauber analysis. Employing the Glauber theory [34] in the optical limit [48,93], Tanihata *et al.* obtained the matter rms from the interaction cross sections measurements [2]: 1.57 (4) 2.48 (3) and 2.52 (3) fm for ^{4,6,8}He, respectively.

The proton elastic scattering of ^{6,8}He nuclei [94] at high energy ($700\,A\cdot$MeV) was also analyzed within a Glauber model; the rms radii deduced initially from this

Table 5. Rms radii of the matter r_m, proton r_p and neutron r_n distributions estimated from reaction cross sections (σ_I by Tanihata *et al.* [2]) and rms from proton scattering at high incident energy [94]; "FB" corresponds to the values obtained within the reanalysis in refs. [96,97].

Nucleus	σ_I, σ_R	(p,p) at $700\,A\cdot$MeV
	r_m (fm)	r_m (fm)
^{4}He	1.57 ± 0.04 [93]	1.49 (3) [94]
^{6}He	2.33 ± 0.04 [48]	2.30 ± 0.07 [94]
^{6}He	2.48 ± 0.03 [93]	
FB	2.52 ± 0.06 [96]	2.5 ± 0.1 [97]
^{8}He	2.49 ± 0.04 [48]	2.45 ± 0.07 [94]
^{8}He	2.52 ± 0.03 [93]	
FB		2.6 ± 0.1 [97]

analysis are given in table 5. Parametrizations for the nuclear distributions were also tested in ref. [94], assuming that the protons were located inside the core ($N = 2$, $Z = 2$) of these nuclei. With the proton radius equal to the core radius, they found the following rms radii values for the p, n distributions: $r_p = 1.88$ (12), $r_n = 2.48$ (11) fm for ^{6}He, $r_p = 1.55$ (15), $r_n = 2.67$ (5) fm for ^{8}He. In the case of the stable ^{4}He nucleus, a reference value (from EM probe) can be considered: the r_m radius was obtained from the evaluations of (e,e) scattering data with a value of 1.46 (5) fm [44,47]; it is underestimated by the radii extracted from reaction models, as given in table 5. This shows that the systematical errors due to the reaction models are larger than indicated in the Glauber model works, and mostly of the order of 0.1 fm.

In sect. 8.1.1, an overview of the rms radii obtained by various technics will be discussed and compared to our findings. In general, the reliability of the extraction and both the mean values and systematic error bars have to be put into question within the Glauber approaches. The ambiguities in the interpretation of the cross sections and of the (p,p) scattering at $700\,A\cdot$MeV rely on the assumptions made for the reaction mechanisms and for the density distributions: the analysis within the Glauber theory is done in the optical limit; the error bars quoted in these studies are of the order of ± 0.04 fm, but these approaches tend to underestimate the systematical error bars due to the model limitations. The main systematical uncertainty is not included in the final values given in the tables: it is due to the assumptions that the projectile has no cluster structure and that the trajectories can be considered as straight lines. It was mandatory to reinvestigate the whole set of data (cross sections, angular distribution on proton target) using approaches combining both a microscopic description of the densities, and a more refined optical model to investigate the cluster structure of the neutron-rich He nuclei. A reinterpretation of the data sets was proposed in refs. [95,96]: an improved Glauber S-matrix approach was developed to take into account the few-body structure of the nuclei having extended nuclear densities. Through this few-body analysis, the values of the ^{6,8}He rms matter radii were re-extracted from the σ_I interaction and σ_R reaction cross sections [96]. The observables of the elastic proton scattering of ^{6,8}He at $700\,A\cdot$MeV were also reinvestigated within this modified cluster Glauber theory [97]. From these reanalysis, the final values of 2.5 ± 0.1 fm were found for the r_m radii of ^{6,8}He. For the next discussions on the comparison between structure models and observations made on He isotopes, we have to take into account two main consequences of this reinterpretation of the σ_I results and of the elastic observables at high incident energies:

- In the case of the more neutron-rich nuclei, the cluster structure has to be taken into account. The rms values r_m for these weakly bound nuclei can be extracted using the Glauber approximation, but this has to be reformulated within the Glauber few-body approach analysis, otherwise the rms values may be underestimated by more than 0.2 fm (see rms ^{8}He 2.2 instead of 2.5).
- the r_m values are given with a sensitivity of ± 0.1 fm, corresponding to the systematical error bars due to the model approach. It means that, in general, the realistic error bars which should be considered for the rms radii extracted from high energy proton elastic scattering or σ_I values are of the order of ± 0.1 fm rather than the lower values quoted in the original articles giving the experimental σ_I as well as the tables for the "experimental" values of the r_m radii.

The result for the matter rms radii of ^{6,8}He shows that, although having 2 more neutrons than ^{6}He, ^{8}He has almost the same size. To have an insight on the neutron extension itself and on the correlations at play, we will discuss below other observables adding constraints on the r_p and r_n values.

3.2.2 Few-body or cluster models

Several microscopic models adapted to the observation of the specific structure characteristics related to the clustering phenomena observed in the light nuclei [11] were built. Amongst the ones developed to describe the specific structure of the He isotopes, assuming cluster states, we can mention:

- few-body models using α-n and nn interactions discussed previously in sect. 3.2;
- the Resonating Group Model (RGM) [98] using an effective NN potential (fitted to the most important NN phase shifts), it gives an overall good description of the properties of the ground and 2_1^+ excited states for ^{6,8}He;
- the 3-body cluster models for ^{6}He [99] and ^{8}He (with ^{6}He-like core) [100]; for ^{8}He, the ^{6}He core excitations are included in the model with the wf defined using the Generator Coordinate Method (GCM).

The matter rms value obtained from the wf calculated by the models are correlated with the neutron separation

Table 6. Rms radii for p, n and matter density distributions of ^{6}He within various frameworks, discussed in the text. The notations for the models are similar to the ones of table 4. FB $fc6$ is given by the 3-body model; the NCSM$_{V3\text{eff}}$, CD and INOY values are the calculations done within the NCSM framework with the $V_{3\text{eff}}$ (6 or 10$\hbar\omega$, 13 MeV [70,71]), CD Bonn and INOY interactions, respectively.

Density model	Ref.	r_p fm	r_n fm	r_m fm	Δr fm	r_m^α fm
FB $fc6$	[36]	1.94	2.79	2.53	0.85	1.49
HFcorr	[72]	1.91	2.34	2.22	0.43	1.50
AMD-m56	[65]	1.90	2.49	2.31	0.59	1.64
NCSM$_{V3\text{eff}}$	[70, 71]	1.76	2.36	2.18	0.60	1.45
NCSM$_{\text{CD}}$	[84]	1.89	2.67	2.41	0.78	1.45
NCSM$_{\text{INOY}}$	[84]	1.76	2.55	2.29	0.79	1.37
FMD	[67]	1.92	2.57	2.42	0.65	1.45
COSM	[90]	1.90	2.49	2.37	0.59	1.46
TOSM	[91]	–	–	2.27	–	1.52
GSM11	[87]	1.89	2.60	2.38	0.71	1.46

energies. More generally, depending on the assumptions made on the microscopic parameters, and on the choice of the core-valence neutrons and nn correlations, a whole set of wfs is generated within the few-body model calculations, and it corresponds to different values for the observables (S_n, r_m). In some of the few-body or cluster models, when one of the neutron separation energies (S_n or $S_{2\text{n}}$ or $S_{4\text{n}}$) is a free parameter, it can be tuned to the experimental value. This is the case in the 5-body $\alpha + 4$n *COSMA* model discussed in sect. 1.2. To discuss the realistic values of the rms radii for the matter densities of ^{6,8}He, we may select the ones produced with the $S_{2\text{n}}$ and $S_{4\text{n}}$ values closer to the experimental ones, that is 978 keV and 3.1 MeV, respectively. In the 3-body $\alpha + 2$n cluster model using phenomenological NN interactions, the size of the neutron halo is directly correlated to the 2-neutron separation energy. For instance in the set of wfs generated by the 3-body model, for $S_{2\text{n}}$ varying from 1.6 MeV to 700 keV, the r_m radii are found to vary between 2.2 up to 2.7 fm [36]. If we consider the density $fc6$, corresponding to the $S_{2\text{n}} = 930$ keV value, closer to experiment, the corresponding r_m radius is found at 2.53 fm.

3.2.3 About the sensitivity of the data to the rms radii and to the cluster structure

The rms radii of the densities calculated with the various models discussed before are presented in table 6, with the r_m for ^{4}He, r_m^α given in comparison. The many-body correlations considered within the microscopic structure approaches produce various sets of proton and neutron densities, when we compare these sets, significant difference (more than 0.2 fm) can be observed for the rms r_p and r_n radii although the corresponding matter r_m radii do not differ by less than 0.1 fm. The experimental determination of the r_p, r_n values may help to discriminate between the theoretical inputs related to the interactions and pairing. An important effect has to be underlined: within the mean-field model, an anti-pairing halo was demonstrated in ref. [101]: for weakly bound systems the size of the wf (seen through rms radii) does not expand as the $S_{2\text{n}}$ is decreasing. It means that, for the ^{4,6,8}He isotopes, not only the sequence of the binding energies is crucial to assess the validity of the interactions used in the models, but also the rms radii are needed to check if the theories have a "realistic" treatment of the nuclear correlations and pairing.

The question is now to discriminate between the various structure models proposed for ^{6,8}He and to select the probes and reactions which could give us a sensitivity on the proton and neutron rms radii difference. As discussed in sect. 2.4, the (p, p') observables should provide the sensitivity to the neutron density distributions and it should be possible to test the validity of the nuclear models by comparing their calculated neutron r_n radius with the value deduced from the (p, p') analysis with an accuracy better than 0.3 fm. First, in sect. 3.3, we will examine the r_p radii deduced from the measurement of the charge rms radii. In the next steps: i) The gs and transition densities given for ^{6,8}He within the *ab initio* NCSM [83] will be used to generate the JLM microscopic density-dependent potentials and transition form factors as described in sect. 2.1. ii) Using these potentials, the (p, p') cross sections will be calculated within the optical model approach and compared to the data in sect. 4. iii) Various sets of nuclear densities will also be tested, and the microscopic structure consistent with the data will be discussed; the range of the rms matter radii and of the inferred neutron rms radii will be given.

3.3 Charge rms from laser spectroscopy

In nuclear structure theories, the spatial distributions of protons and neutrons are calculated treating both as point particles. From the rms charge radius ($\langle r_{ch}^2 \rangle^{1/2}$) (denoted also below as r_{ch}), the point-proton radius ($\langle r_{po}^2 \rangle^{1/2}$) can be extracted by the relation recently discussed in ref. [102] including also the terms coming from the spin-orbit (SO) correction:

$$\langle r_{po}^2 \rangle = \langle r_{ch}^2 \rangle - \langle r_P^2 \rangle - r_{DF}^2 - \frac{N}{Z} \langle r_N^2 \rangle - \langle r^2 \rangle_{so}, \qquad (8)$$

where

– $\langle r_P^2 \rangle$ and $\langle r_N^2 \rangle$ are the mean-square charge radii of the proton and neutron, with $\langle r_P^2 \rangle = 0.769\ (12)\ \text{fm}^2$ and $\langle r_N^2 \rangle = -0.1161\ (22)\ \text{fm}^2$ as given in the 2006 evaluation of ref. [56][2], $\langle r_P^2 \rangle = 0.877\ (7)\ \text{fm}^2$ as given in 2010 in ref. [57];

[2] See, for instance, ref. [103], for possible explanations about the negative value of $\langle r_N^2 \rangle$; in a simplified approach, it may reflect the internal distribution in terms of charged quarks, with u quark pushed to the center, dd quarks to the edge.

Table 7. Charge rms radii evaluated from e-scattering or laser spectroscopy for ^{4,6,8}He isotopes, as discussed in the text, and the corresponding proton rms radii, two evaluations are given using the values $R_P = 0.877(7)$ fm from ref. [57] or $R_P = 0.84184(67)$ fm from ref. [105], and also considering the new mass evaluation for the isotopes.

Nucleus	r_{ch} (fm)	r_p (fm) PDG 2010 [57]	r_p (fm) 2010 [105]
^{4}He	1.673 (1) [106]		
	1.676 (8) [44]	1.46 (5) [44]	
	1.681 (4) [107]		1.511
^{6}He	2.054 (14) [60]		2.30 ± 0.07
	2.068 (11) [61]		
New mass	2.060 (8) [62]	1.938 (23)	1.953 (22)
^{8}He	1.93 (3) [61]		
New mass	1.959 (16) [62]	1.885 (48)	1.901 (48)

- r^2_{DF}, known as the Darwin-Foldy (DF) term, is the relativistic recoil correction or a nuclear finite-size shift contribution equal to $[3/(4M_p^2)] = 0.033\,\mathrm{fm}^2$ [104];
- and r^2_{so} is expressed as a charge-density correction due to the nuclear SO interaction.

The value of the mean square radius of the proton was also given with higher accuracy as: $\langle r^2_P \rangle = 0.84184\ (67)\,\mathrm{fm}^2$ [105]. Note that the r^2_{so} value is obtained in ref. [102] at $-0.08\,\mathrm{fm}^2$ for ^{6}He and at $-0.17\,\mathrm{fm}^2$ for ^{8}He but the calculations are done for the extreme cases, assuming, respectively, a pure p-wave and full $p_{3/2}$ configuration —this assumption will be discussed in sect. 7.1. The nuclear charge radii of the ^{6,8}He nuclei were extracted from the isotope shifts [60, 61], measured with respect to ^{4}He, the values were obtained using precision atomic theory calculations, neglecting the r^2_{so} term, and taking into account the DF term. The ^{4}He charge radius was measured to be 1.673(1) fm in ref. [106] (from the spectroscopy of muonic ^{4}He atoms) and 1.681(4) fm from precise reevaluation of the data sets of electron scattering experiments [107]. In ref. [61], the rms charge radii for ^{6,8}He are extracted using, for the ^{4}He charge radius, the value of 1.676(8) fm from ref. [44]. For ^{6}He, the value: $r_{ch} = 2.054 \pm 0.014$ fm was first given in ref. [60]. For ^{8}He, the value $r_{ch} = 1.93(3)$ fm was extracted in ref. [61]. In the experiment reported in ref. [61], both ^{6,8}He beams were produced at GANIL with the SPIRAL facility; the rms charge radius for ^{6}He was remeasured giving the new value: 2.068(11) fm, found in good agreement with the previous one measured at Argonne [60].

Using the new mass values obtained for ^{6,8}He, the authors of ref. [62] have re-evaluated the r_{ch} radii extracted from the isotopic shifts to 2.060(8) and 1.959(16) fm. Taking into account the SO correction as well as the DF term, they have deduced the r_{po} radii. The r_{po} radii of ^{6,8}He were also deduced in ref. [62] with this new evaluations of $\langle r^2_P \rangle$, as shown in table 7. The significant contributions are from $\langle r^2_{P,N} \rangle$. For the precise discussion of the charge radii, it is interesting to note that the shell configurations for ^{6,8}He have to be determined to calculate the r^2_{so} term precisely. This value is influenced by the neutron configurations which can be deduced from the direct reactions. However, if we discuss the rms radius value of the matter, neutron and proton densities to the level of a 0.1 fm accuracy due to the theoretical undetermination of the matter rms related to the neutron correlations the formula (8) can be approximated to: $\langle r^2_{po} \rangle = \langle r^2_{ch} \rangle - \langle r^2_P \rangle - (N/Z)\langle r^2_N \rangle$.

When the microscopic theories give the point nucleon radius r^{po}_p or r^{po}_n calculated from the nucleon wfs, the point nucleon distributions have to be folded with the nucleon matter distribution (for which $\langle r^2 \rangle \simeq 0.8\,\mathrm{fm}^2$). Hereafter, we always consider the r_p or r_n values, not the point distribution radii for the comparison to the experimental values of the r_p, r_n radii.

4 Direct reactions on proton: experimental tools and reaction models for the analysis of proton elastic and inelastic scattering

Detailed spectroscopic information can be deduced from complementary studies of direct reactions:

- elastic and inelastic (p, p′) scattering to probe wfs and neutron excitations;
- one-nucleon transfers (p,d), (d,p) ($E \sim 10$–$30\,A\cdot$MeV) on proton or deuteron targets to probe the single-particle shell structure and overlap wfs;
- (p,t) reactions ($E \sim 10$–$100\,A\cdot$MeV) to obtain information on pairing correlations as well as on 0^+ excited states.

We start describing the experimental tools developed for the measurements of these direct reactions on light targets. In sect. 4.3 we present the reaction model combining microscopic optical potentials and coupled channels; it provides a first direct approach for the investigation of the microscopic parameters of the nuclear structure at low energy. We will confront the interpretation of the new extended data set obtained at low energy, $\sim 15\,A\cdot$MeV, with the ones available in the literature at higher energies.

4.1 Experimental technique for the direct reactions on proton target in inverse kinematics

Several experimental devices were developed these 10 last years, to identify and measure the characteristics of the recoiling light charged particles produced in the nuclear direct reactions induced by radioactive beams on proton or deuteron targets, using mainly solid target foils of $(CH_2)_n$ polypropylene or CD_2 respectively, for incident beam energies between 10 and $100\,A\cdot$MeV. Arrays of telescope modules, composed of silicon-strip array of large active area, followed by second and third stages for E-DE PID, were specifically designed, with the related specific electronics, to detect with high granularity and energy resolutions the light charged particles. Amongst the

devices offering comparable range of applications and similar conception, we can mention the ones used at GANIL: MUST [108], MUST2 [109][3] and TIARA [110], and, at MSU: HIRA [111]. MUST and MUST2 correspond to two generations of detector modules of three-stage telescopes (a set of 300 μm thick Double-Sided Si-strips Detector-DSSD, followed by SiLi and CsI detectors) measurement of direct reactions: the 8 DSSDs ($6 \times 6\,\mathrm{cm}^2$ active area each) MUST modules [108] and from 2007, the device of MUST2 modules [109] (each one of $10 \times 10\,\mathrm{cm}^2$ area), extended to 8 modules in 2013, to increase the performances for the angular coverage, the particle identification detection (PID) and the granularity. It has to be underlined that both HIRA and MUST2 have three square stages with double sided Si detectors, but MUST2 has the larger active area (10 by 10; HiRA is $6.25 \times 6.25\,\mathrm{cm}^2$) and the higher granularity, with $128X$ by $128Y$ Si-strips (32 by 32 for HiRA). Moreover, the MUST2 has an innovative electronics, based on the ASICs (Application Specific Integrated Card), which gives the time and energy measurements for each strip, and the E-TOF PID for low-energy particles. With all these characteristics, MUST2 appears as a rather unique device to carry out a complete reconstruction of the direct reaction kinematics.

In this review article, we focus on the results obtained with the GANIL/SPIRAL beams of ^{6,8}He, using the MUST, MUST2 arrays. These telescopes have threshold energy of $\sim$ 300–400 keV. For a full reconstruction of the reaction kinematics, the Si-strip devices are combined with two beam tracking detectors located upstream of the target, the multi-wire chambers CATS [112], (*Chambres à trajectoires de Saclay*), to detect event by event the position of the incident beam particles. From the reconstruction of the trajectories on the target, the incident angles and impact position of the beam on the target can be obtained. The typical resolution (FWHM) for the position reconstruction is of 0.6 mm, the reconstruction efficiency of the ^{8}He trajectory is obtained at 94%. the intrinsic resolution of the detectors obtained from the alpha calibration are between from 35 to 50 keV (FWHM). The resolutions in the excitation energy spectra ΔE^* achieved during experiments using CH_2 targets from 1.5 to 10 mg/cm^2 are ranging between 400 to 700 keV (FWHM). Energy, time of flight (between Si-strips and CATS with a FWHM resolution of 1.2–1.4 ns for $Z = 2$ particles) and position of the light charged particle are measured in the Si-CsI array detector, allowing for an identification of the light particles and for a full reconstruction of the (p, p$'$) kinematics, which are the correlations between the total kinetic energy of the proton and its scattering angles.

At the GANIL accelerator facility (*Grand Accélérateur National d'Ions Lourds*, Caen, France), the MUST and MUST2 arrays were intensively used with the exotic beams of ^{6}He and ^{8}He, to measure a whole set of direct reactions on proton in the following experiments:

– (E293) experiment (MUST array) for the $\mathbf{^6He(p, p')}$; the ^{6}He secondary beam was produced at 40.9 $A \cdot$ MeV at an intensity of 1.8 10^5 pps by fragmentation of a primary ^{12}C projectile at 75 $A \cdot$ MeV on the target of the SISSI device; the experimental set-up, the analysis for the extraction of the (p, p$'$) cross sections are described in ref. [113].

– E347 (MUST) for the $\mathbf{^6He(p, t)}$ and the (p,p), using the ^{6}He secondary beam produced at 10^5 pps and at 25 $A \cdot$ MeV [114].

– E405S (MUST): the $\mathbf{^8He(p, p')}$ scattering was measured using an ^{8}He beam produced at 15.7 $A \cdot$ MeV by the SPIRAL facility with an intensity of 1.3 10^4 pps. From the proton kinematics obtained in coincidence with the He isotopes, the excitation functions were obtained. From the coincidence between protons and the ^{8}He heavy ejectile, the elastic scattering yield can be deduced, and with ^{6}He or ^{4}He coming from the 2^+ unbound state of ^{8}He, it provides the determination of the inelastic scattering yields. The spectroscopy of ^{7}He was also measured from the (p,d) reaction [115], and the (p,p) elastic and (p,d) transfer were analyzed in the coupled reaction framework in ref. [116]. With the same set-up, the (p,t) [117, 118] reactions were measured as by-product data set but with a very limited angular coverage.

– E525S (MUST2): to explore the spectroscopy of ^{6}He and to find new low-lying resonant states populated by the 2n-transfer from the ^{8}He beam, the $\mathbf{^8He(p, t)}$ reactions were measured at 15.4 $A \cdot$ MeV using the large angular coverage MUST2. With this improved setup, it was possible to detect all the light charged particles (p,d,t) produced by the ^{8}He + p reactions, in coincidence with the ^{4,6}He particles. The measurements and the analysis are explained in the article [119].

The whole experimental set-up and the analysis done to extract the energy excitation spectra and the cross sections for ^{8}He(p, p$'$), ^{8}He(p,d) (p,t) at 15.7 $A \cdot$ MeV and (p,t) at 15.4 $A \cdot$ MeV are fully described in the above references. The set-ups with the MUST and MUST2 arrays, for the E405S and E525S experiments, are presented in fig. 2. For E405S, data were taken with a 8.25 mg/cm^2 thick $(CH_2)_n$ target, and, to measure the (p, p$'$) at angles below $40^\circ_{c.m.}$, a thinner one (1.48 mg/cm^2) was used. For E525S, the 4.48 mg/cm^2 thick (50 μm) $(CH_2)_n$ was employed for the dedicated (p,t) measurement. For the ^{8}He + proton reactions at 15.7 $A \cdot$ MeV, the calculations of the kinematics are presented in fig. 3. The black, red and blue lines correspond to the (p,p), (p,d) and (p,t) reactions to the states of ^{8,7,6}He nuclei, respectively. The excited states of ^{6,8}He are unbound, they decay through particle emission: the ^{8}He excited states may decay into ^{6}He + 2n or have a sequential decay into ^{7}He (unbound)+n then to ^{6}He + 2n; for states above the S_{4n}, the decay may be into α + 4n particles. In the case of the ^{8}He(p,d) reactions to the ^{7}He ground and excited states [115] the particles in the exit channels correspond to ^{6}He + 2n or α + 3n. For ^{8}He(p,t) to the ^{6}He ground or excited states, the particles produced in the exit channels are: ^{6}He + 2n or α + 4n.

[3] MUST2 web site: `http://must2.cea.fr`.

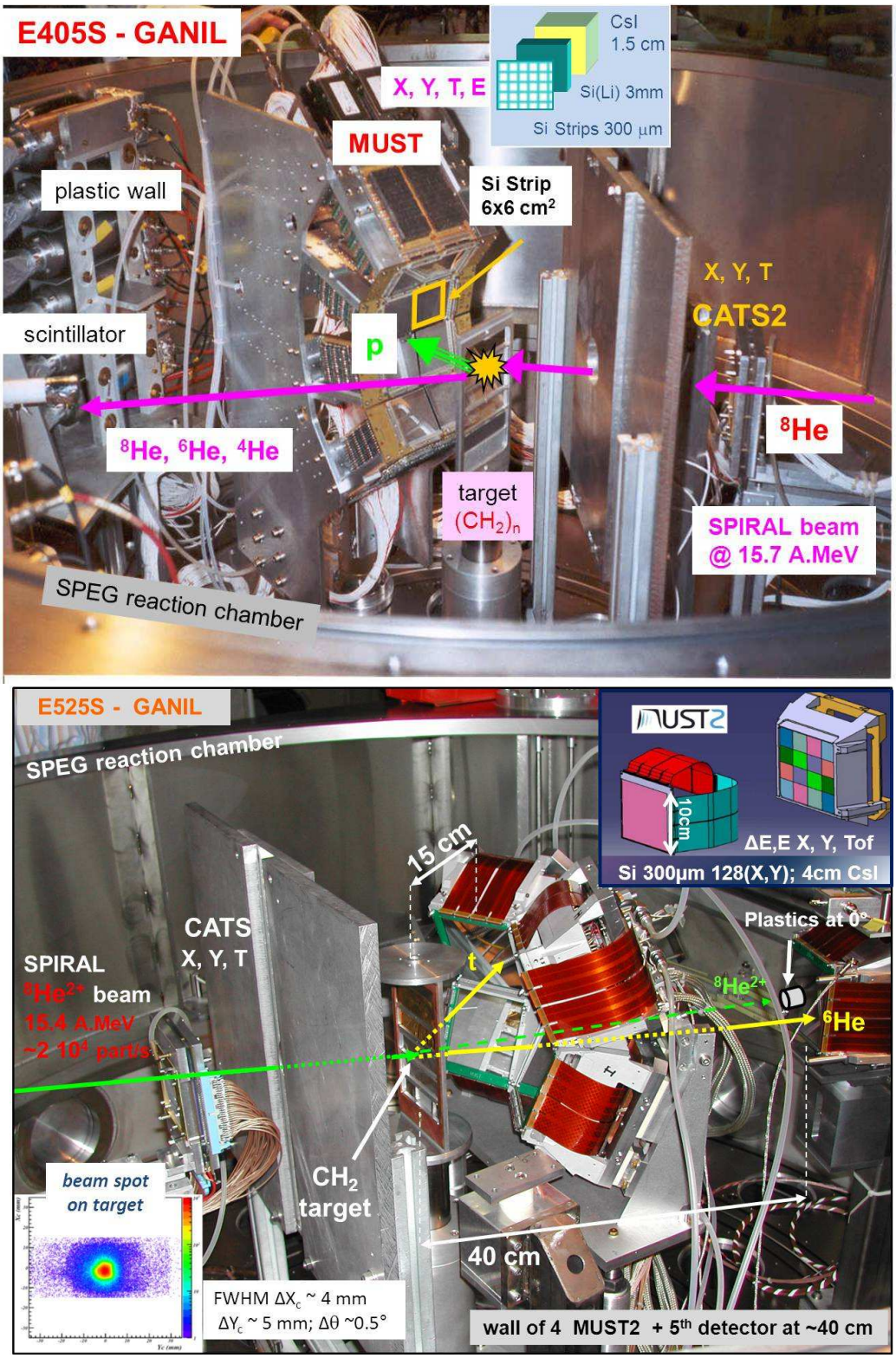

Fig. 2. Experimental set-up at GANIL with the MUST (top) and MUST2 (bottom) telescopes used for the E405S and E525S experiments described in the text. (Top) The MUST array was assembled in a wall configuration, located at 15 cm from the target. It was placed in two positions with the vertical axis rotated by angles of 50° and of 65°, with respect to the beam axis in the laboratory frame. (Bottom) The MUST2 array was assembled in a square wall of 2 by 2 detectors. A fifth detector was located at 40 cm behind the wall, with a plastic scintillator placed in front of this telescope to shelter it and to collect the beam particles and the reaction ejectiles produced in the most forward direction around 0 degrees. Two CATS detectors were located upstream of the target; the one closer to the target can be seen in the left (right) side of the top (bottom) figure, respectively.

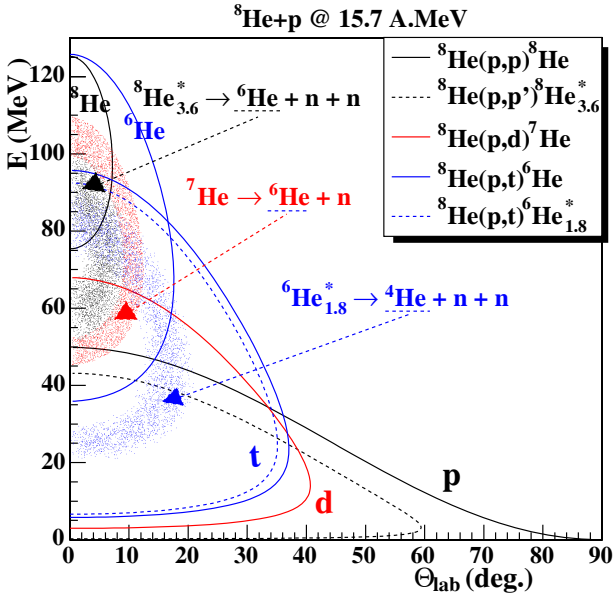

Fig. 3. Calculated kinematics for the direct reactions of ^{8}He on protons at 15.7 $A\cdot$MeV: the (p,p), (p,d) and (p,t) channels to the *gs* (plain line) and first excited (dotted line) states of ^{8}He, ^{7}He and ^{6}He are shown with the black, red and blue curves, respectively. The charged particles α or ^{6}He produced by the decay of the unbound states are indicated with the cloud of points.

The excitation energy spectra for the ^{6,7,8}He nuclei are obtained via missing mass method and the reconstruction of the relativistic kinematics of the light charged particles, triton, deuton and proton, respectively. The kinematics are obtained through the measurements of the position, momentum and total kinetic energies of the particles detected in the Si-strip telescope array.

For a reaction of particles labelled 1 to 4, of incident beam (1) on target nucleus (2) producing ejectile (3) and scattered light partner (4) —like the p, d, or t particles— the excitation energy of "3" is expressed as: $E_{\rm exc} = (m_r - m_0)c^2$ with m_0c^2 the *gs* mass of the ejectile "3" (for instance He isotopes), and m_r the recoil energy deduced from: i) the kinematical characteristics (total energy E_4, momentum p_4, of the light charged particle detected in the Si-array, $\theta_{\rm lab}$ its angle with the beam axis in the laboratory frame and iii) the energies and momentum of the beam "1" ($E_1 = T_1 + m_1c^2$, $T_1 = T_{\rm beam}$ kinetic energy, $p_1 = p_{\rm beam}$) following the relationship:

$$(m_rc^2)^2 = (E_1 + m_2c^2 - E_4)^2 - p_1^2 - p_4^2 + 2p_1p_4\cos(\theta_{\rm lab}), \quad (9)$$

deduced from the relativistic invariant applied for particle 3 using the energy and momentum conservation laws of the reaction. The dashed (black and red) lines corresponds to the loci of the (p, p′) to the 2_1^+ excited state of ^{8}He and (p,t)^{6}He(2_1^+).

In fig. 3 the calculated kinematics, correlation spectra between E and $\theta_{\rm lab}$, are presented for the particles p, d, t produced by the main direct reactions of ^{8}He on proton, the (p, p′), the (p,d) and (p,t), respectively. In figs. 4 and 5, the kinematical plots show the yields of the detected particles p, d, t produced in the reactions induced by the ^{8}He beam on proton during the E405S and E525S experiments, at incident energies of 15.7 and at 15.4 $A\cdot$MeV, respectively. The extraction of the excitation energy spectra for ^{6}He and of the differential cross sections (p,t) are

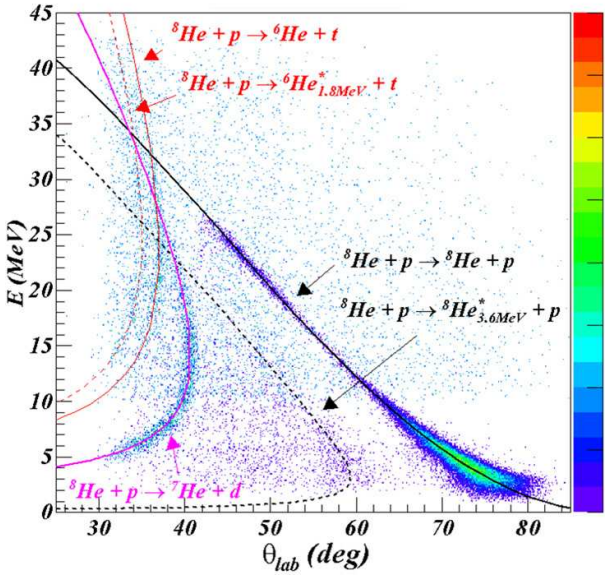

Fig. 4. Reconstructed kinematics for the direct reactions of ^{8}He on protons at 15.7 $A\cdot$MeV, (p, p′), (p,d) and (p,t) measured on the 1.5 mg/cm^2 thick $(CH_2)_n$ target using the MUST array in the experiment E405S. See details in the text.

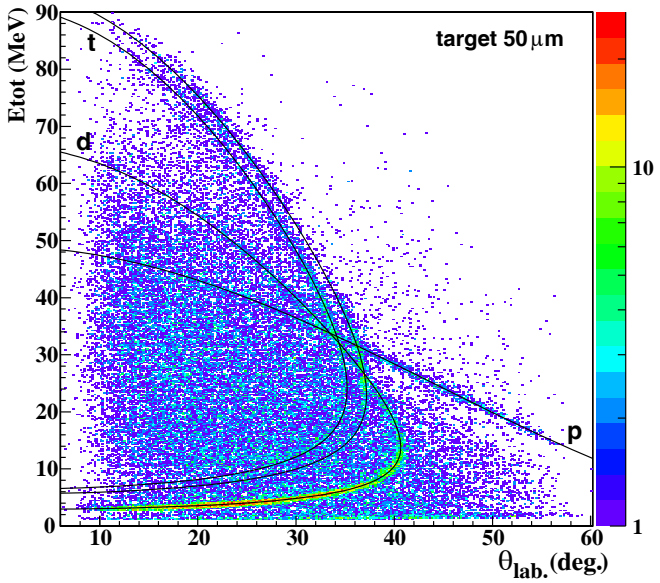

Fig. 5. Same as in fig. 4 for ^{8}He at 15.4 $A\cdot$MeV in the E525S experiment, with the MUST2 array and the 4.48 mg/cm^2 thick $(CH_2)_n$ target.

explained in ref. [119]. With these data at hand, complete in terms of the number of reaction channel involve in the ^{8}He + p process, and for the angular coverage, the objectives are: i) to have a consistent extraction of the structure inputs from all existing data on proton target; ii) to obtain new spectroscopic data for the excited states of ^{6,8}He.

4.2 Optical model framework using phenomenological potentials

The reaction formalisms were mainly developed for nuclei close to the valley of stability. In general, the description of direct nuclear reactions is established on optical models, using local potentials [28]. To take into account the global properties of the nuclear interaction between projectile and target during the elastic and inelastic scattering, the potentials are built with the following characteristics: attractive, uniform for small radii (interior of the nucleus) and decreasing as radius increases from the center to the surface of the nucleus. The potentials defined as a combination of Woods-Saxon (WS) functions are mostly used and their parameters are adjusted on the geometrical properties of the interacting nuclei and on the energy of the system to describe the scattering quantitavely. The surface and the SO potentials are expressed as second order terms, expressed as derivative of WS potentials. We note below $f(r, R, a)$ the WS form factor function of the r radial coordinate, with parameters R_f, radius, and a_f the diffuseness is defined as

$$f(r, R_f, a_f) = \left[1 + \exp\left(\frac{r - R_f}{a_f}\right)\right]^{-1}. \quad (10)$$

From R_f we define the reduced radius r_f as: $R_f = r_f A^{1/3}$ in the case of the nucleus-nucleon scattering. In the optical model approach, the standard complex potential $U(r)$ is expressed as: $U(r) = V(r) + iW(r) + U_{SO}(r) + V_C(r)$, with V, W the real and imaginary parts (volume and surface), V_{so}, W_{so} for the spin-orbit potential, and V_C the Coulomb potential. The general forms for the real V, imaginary W and SO parts are written as

$$V(r) = -V_v f(r, R_v, a_v) - (4a_{vs})V_S \frac{\mathrm{d}}{\mathrm{d}r} f(r, R_s, a_s) \quad (11)$$

$$W(r) = -W_v f(r, R_w, a_w) - (4a_{ws})W_S \frac{\mathrm{d}}{\mathrm{d}r} f(r, R_{ws}, a_{ws}) \quad (12)$$

$$U_{SO}(r) = -2(V_{so} + iW_{so}) \left(\frac{-1}{r}\right) \frac{\mathrm{d}}{\mathrm{d}r} f(r, R_{so}, a_{so})(\boldsymbol{l} \cdot \boldsymbol{\sigma}). \quad (13)$$

Global parameterizations were elaborated to describe the nucleon-nucleus potentials and to calculate the elastic scattering using as inputs the (A, Z) and the incident energy E of the nucleus. The dependence (A, Z, E) of the potential parameters were obtained by fitting a wide range of nuclear data with prescriptions on the R_i, a_i and energy-dependence. For instance, we may consider the phenomenological CH89 [120] potential, which was shown to provide a good description of the nuclear data, even when the calculations were extrapolated for an energy range and a nuclear domain outside from the initial domain of validity, due to the data set used to build the global potential (E_p from 16 to 65 MeV and A from 40 to 209). CH89 gives good extrapolation of the nuclear potential for exotic nuclei due to its parameterization taking into account the asymmetry: $\epsilon = (N - Z)/2$. The potential is defined with V, W_v, W_S depending on E, Z and ϵ, no real surface term and no imaginary SO part ($V_S = 0$, $W_{so} = 0$). V_{so} is fixed to 5.9 MeV $\cdot$ fm^2, the radii are function of $A^{1/3}$, $R_w = R_{ws}$, and the diffuseness parameters a_v, a_w and a_{ws} are fixed to 0.69, a_{so} to 0.63 fm; for the Coulomb potential, $a_C = 0.75$ fm. The Coulomb potential is written as: for $r \geq R_C$, $V_C = Ze^2/r$ and for $r \leq R_C$, $V_C(r) = \frac{Ze^2}{2R_C}\left[3 - \left(\frac{r}{R_C}\right)^2\right]$ [52]. For the proton-nucleus scattering, in general R_C can be taken as equal to the uniform charge radius deduced from measurements (electron scattering in the case of the stable nuclei): $R_C = (\frac{5}{3}\langle r^2\rangle_{ch})^{1/2}$.

At an incident energy regime corresponding to direct processes mainly at the surface, and for stable projectile-target systems, the standard approach to describe the inelastic reactions is the Distorted Wave Born Approximation (DWBA) using deformed potentials, with the optical potential written as: $U(r) = U_0(r) + \Delta U$, where U_0 is the spherical potential for the elastic scattering and ΔU the deformed one for the inelastic process.

In a macroscopic approach, the excitation of the nucleus is considered as a deformation of its surface expressed as a variation of its radius R, function of the spatial coordinates (θ, ϕ). Following this deformation, the resulting potential can be expanded in series of Taylor around the central equilibrium radius [58]. The validity domain of this phenomenological model and the procedure steps for the inelastic scattering calculations using the DP are given in Satchler's textbook [28]; the assumptions are discussed in refs. [28,121]. The deformed potential (DP) is usually written as the first-order Taylor expansion of the potential used for the elastic channel U, which is either microscopic or a phenomenological one. The deformed potentials are defined as

$$U_i^{\mathrm{def}} = \beta_i * R_i \frac{\mathrm{d}U_i(r)}{\mathrm{d}r}, \quad (14)$$

with $\delta_i = \beta_i * R_i$ the deformation lengths for the potential term i.

The deformation lengths for the nuclear and Coulomb potentials are usually expressed as: $\delta_N = \beta_N^v R_V = \beta_N^w R_W$ and $\delta_C = \beta_C R_C$. The deformed Coulomb potential is defined introducing the deformation length $\beta_C R_C = \delta_C$. The deformation parameter β_C is usually defined in a collective excitation model-dependent approach, it relies on the assumption that the charge distribution is uniform inside the radial volume $R(\theta, \phi)$ and 0 beyond. The relationship between the Coulomb excitation and the deformation can be expressed as, for a multipolarity l, with δ_l^p the proton

deformation length and R_C the radial parameter:

$$B(El) = \left(\frac{3R_C^{l-1}\delta_l^p}{4\pi} \right)^2 (Ze)^2.$$

In general, the adopted value is $R_C = r_0 A^{1/3}$ and $r_0 \simeq 1.2$–1.3 fm (the larger value r_o, 1.3 fm, is for light nuclei). In ref. [121], it is shown that: "a more realistic approach takes account of the rounded surface of the proton distribution" and that R_C has to be l-dependent, Only for $l = 2$ "acceptable results" are obtained with the simple formula for the $l = 2$ transition from gs to 2^+ state, that is

$$B(E2, 0^+ \to 2^+) = \left[\frac{(3R_C^2)}{(4\pi)} \right]^2 (Ze)^2 \beta_C^2.$$

In ref. [28], it is also underlined that the relationship between the deformation parameters of the densities and of potentials is not straightforward; they are not similar simply because, in the realistic case, the nucleus is not a point-like particle, the interaction is density-dependent and has a finite range. This approach is oftenly used to make easily comparisons of the potential deformations between nuclei, and in particular to check the trend of the macroscopic potential deformations along isotopic chains, but these parameters do not correspond to the microscopic deformations of the nuclear density itself. It means that the most direct and unambiguous way to check the validity of sets of nuclear transition densities with various assumptions on the proton and neutron density deformations is to use a microscopic approach with a density-dependent potential, thus, the data can be interpreted quantitatively to infer the deformation parameters of the nucleus wf itself. This microscopic folding approach FA will be described in sect. 4.3, it gives a transition potential by folding an effective NN interaction over the target gs and the transition density of the excited nucleus. It is also explained in ref. [121] that, in general, both methods, the FA and the DP have different l dependence, with "obvious differences arising from finite-size effects (finite size of the probe nucleus and finite range of the effective interaction). These effects result in a strong l-dependence in the shape of the folded transition potential even if the transition density is independent of l, whereas the transition potential from the DP model has a shape that is l-independent".

4.3 Optical model framework using microscopic potentials

Two main formalisms were developed to describe the reaction observables with a microscopic potential model:

- The $\mathcal{N}$-body theories developed for the scattering studies, for instance, by Watson [122], Kerman, McManus et Thaler (KMT) [123], and the Glauber theory [34].
- The G-matrix formalism [124–126], which was intensively used for the scattering of a large range of nuclei.

In the few-body reaction models [36, 96], the calculations are done using the assumption of an *a priori* cluster structure and reducing the possible degrees of freedom. The cross sections (interaction, elastic, inelastic) are calculated using the scattering amplitude decomposition on the various clusters of the nuclear system. In the case of halo nuclei, these calculations usually consider an inert core and valence nucleons. Few-body models were built to treat more specifically the case of the light exotic nuclei [127], for instance the ^{6,8}He [97] and ^{9,11}Li proton scattering.

The validity of these approaches depends on the characteristics of the system (like total kinetic energy, S_{1n} or S_{2n} energies, relative mass between valence particles and core) and due to the various assumptions corresponding to an inert core and to frozen degrees of freedom (adiabatic case), it is in general more adapted to a higher energy domain (typically above $100\,A \cdot$ MeV) and for loosely bound nuclei. For the energy domain in which we are interested in, ranging from 10 to $100\,A \cdot$ MeV, we prefer to adopt the optical model approach, using a nucleus-proton interaction deduced from the G-matrix calculations: the validity of the Local Density Approximation (LDA) is assumed to evaluate the optical potential for finite-size nuclei from the nuclear matter calculations, whereas for other formalisms, the finite-range aspects are included from the beginning of the calculations, to build the scattering model. Within this G-matrix approach, it is possible to test various structure model assumptions and the radial densities provided by the nuclear theories, without any *a priori* on the composite structure of the nucleus. The nucleon-nucleus potential used in this study is the microscopic, complex and parameter-free JLM (Jeukenne, Lejeune and Mahaux, from the authors's names) potential [125,126]. It is based upon infinite nuclear matter calculations and it is built on the Reid hard-core Nucleon-Nucleon (NN) interaction, using the Brueckner-Hartree-Fock approximation. An "improved" (with smoothing function) LDA is applied to derive the potential in the case of a finite-range nucleus of density ρ, with neutron ρ_n and proton ρ_p densities; the resulting potential can be written with local densities $\rho(r)$. The choice of the JLM potential was driven by two main criteria: 1) it is complex, microscopic meaning that both the real and imaginary parts of the potential are calculated, using the nuclear densities; and 2) because it was shown since its birth in 1976, that it could give a good understanding of elastic and inelastic scattering for nucleon-nucleus and successfully reproduce a large set of data in terms of mass region and incident energies [128,129]. The JLM potential was parameterized for incident nucleon energies up to 160 MeV. It depends only on the incident energy E and on the neutron and proton densities of the nucleus. In general, the normalization factors for the real and imaginary parts, λ_V and λ_W, are introduced to adjust the optical potential calculations to the data:

$$U_{JLM}(\rho, E)(r) = \lambda_V V(\rho, E)(r) + i\lambda_W W(\rho, E)(r), \quad (15)$$

λ_V and λ_W are found close to 1 for all stable nuclei and, for $A \geq 20$, it was shown that the JLM potential has to be only slightly modified (less than 10%) to fit the nucleus-nucleon data. It was also shown that usually in the case of

light nuclei ($A \leq 20$), the data are better described adopting: $\lambda_W = 0.8$ [128]; this was attributed to a correction of the finite-range effect in the case of the light nuclei. Below, the $\lambda_V = 1.0$, $\lambda_W = 0.8$ normalization is considered as the "standard" JLM for the light nuclei. A careful analysis of the elastic scattering is required in the case of weakly bound nuclei in order to have a correct treatment of the coupling effects, as will be explained in sect. 4.5. In the general case of a collective description of the inelastic $(\mathrm{p}, \mathrm{p}')$ scattering, the transition potentials can be expressed with the elastic potential $U(\rho, E)$ as

$$U^{tr}_{\mathrm{inel}}(\rho^{tr}, E) = \frac{\mathrm{d}U}{\mathrm{d}r} = \frac{\delta U(\rho, E)}{\delta \rho} \rho^{tr}_{fi}. \tag{16}$$

As done in the case of the elastic potential, the LDA is applied to transform the transition potential $U_{in}(\rho^{tr}, E)$ into $U^{fi}_{in}(r) = U^{tr}_{in}(\rho^{tr}, E)(\boldsymbol{r})$ and it is folded with a Gaussian form factor (usually with range $t = 1.2\,\mathrm{fm}$) to take into account the finite-range properties of the interaction:

$$U^{tr}_{fi}(r) = \frac{1}{(t\sqrt{\pi})^3} \int \rho^{tr}_{fi}(\boldsymbol{r'}) U^{tr}_{in}(\rho(\boldsymbol{r'}), E) \times \exp\left[-\frac{(\boldsymbol{r} - \boldsymbol{r'})^2}{t^2}\right] \mathrm{d}\boldsymbol{r'}.$$

The $U(r, E)$ and $U^{fi}_{in}(r, E)$ potentials can be generated using various sets of nuclear *gs* and transition densities. To calculate the elastic and inelastic cross sections, the potential form factors can be used in the DWBA framework, for instance with the Tamura DWBA code [130] dedicated to the form factors of the JLM potential. In general, the Coupled-Channel (CC), coupled reaction channels (CRC) frameworks can be useful and needed to understand the interplay between various reaction channels, and the cross sections are calculated using the reaction codes developed to take into account the CC or CRC: the ECIS [131] or the Fresco codes [132]. As explained in sect. 2.2 the calculated inelastic $(\mathrm{p}, \mathrm{p}')$ cross sections are sensitive to the M factor, defined in eq. (7) as a combination of the M_n and M_p moments. The models of elastic and inelastic scattering on proton, including the potential JLM through DWBA calculations, were proven to be reliable to extract the fundamental quantities such as M_n/M_p without ambiguity for the stable nuclei [129] as well as for the exotic nuclei [133–135]. In sects. 5 and 6, the $^{6,8}\mathrm{He}(\mathrm{p}, \mathrm{p}')$ calculations carried out using the DWBA or CRC frameworks will be discussed.

4.4 ^{6}He gs densities within various structure models

To study the sensitivity of the proton elastic scattering with the nuclear shapes of the matter distributions, various density functions can be used to calculate the proton-nucleus interaction potential and the elastic scattering. For the calculations presented in sect. 4.6, we will consider the following structure models:

– Densities from the *HF corr* model [72] discussed in sect. 3. The halo effect with the spatial extension of the neutron densities is taken into account in this model via the S_{2n} adjusted at the experimental value.
– Densities from the 3-body model calculations, in the version $fc6$ of ref. [36];
– Densities from the NCSM calculations, in the version $V_{3\mathrm{eff}}$, $4\hbar\omega$ (with $\hbar\omega = 13\,\mathrm{MeV}$) [71].

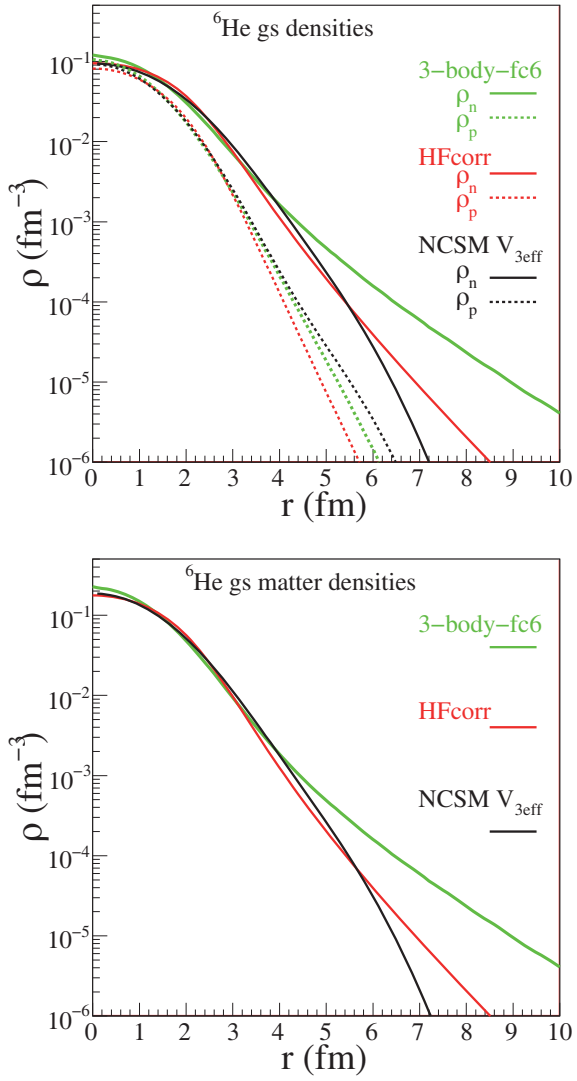

Fig. 6. Nuclear matter (top) and proton, neutron (bottom panel) densities of ^{6}He within various frameworks: NCSM, HF (with correlations) denoted as *HF corr*, few-body model ($fc6$).

We have selected the $fc6$ density which corresponds to an energy of $S_{2n} = 0.93\,\mathrm{MeV}$, consistent with the experimental value. The rms radii are: $r_p = 1.94\,\mathrm{fm}$, $r_n = 2.78\,\mathrm{fm}$, the corresponding rms values for the core extension and for the valence neutrons are: 1.49 fm and 3.42 fm. The matter rms radius is 2.53 fm, consistent with the value discussed in sect. 3.2 for the high-energy $^6\mathrm{He} + \mathrm{p}$ data and also with the value checked in the interpretation of the $^6\mathrm{He} + ^{12}\mathrm{C}$ elastic scattering data [136]. The neutron, proton, and matter density distributions for these calculations are compared in fig. 6.

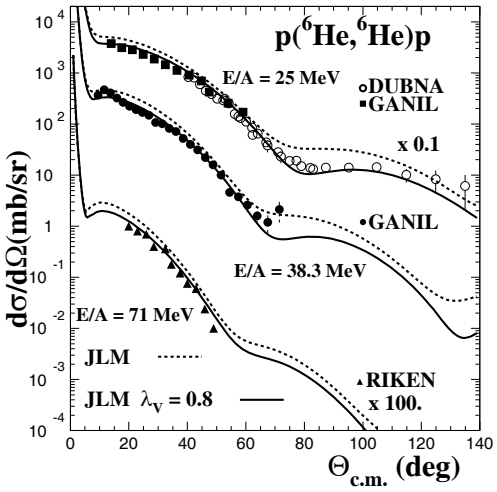

Fig. 7. Worldwide data for the elastic scattering ^{6}He(p, p) between 25 and 100 $A \cdot$ MeV.

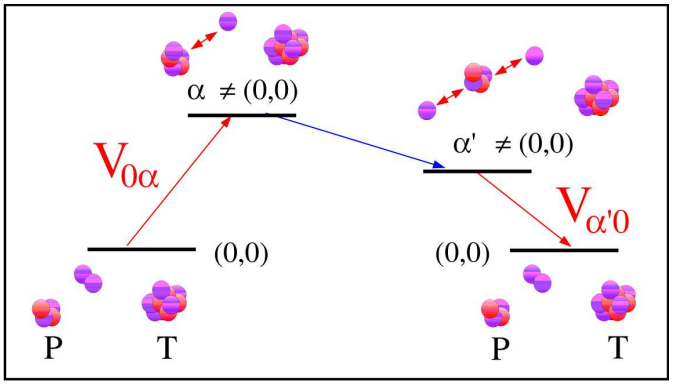

Fig. 8. Scheme of the virtual coupling potential arising from the transitions during the elastic process as formulated in the Feshbach's formula (eq. (17)) expressed for the effective interaction potential between projectile P and target T.

4.5 Coupling effects and Feshbach reaction theory

In an earlier work, we have shown [137] that the angular distributions of ^{6}He on proton are better reproduced with a reduction of the real part of the JLM optical potential, corresponding to 20%. This is illustrated in fig. 7: the worldwide set of ^{6}He(p,p) elastic data, measured at proton energies from 25 A to 73 $A \cdot$ MeV, is compared with the calculations done using the JLM potential generated with the $fc6$ halo-density. When the cross sections are calculated with the standard ($\lambda_V = 1$) entrance channel potential, the data are overestimated. Reducing the JLM real part with $\lambda_V = 0.8$, the calculations are in agreement with the data, and this is observed for the whole range of incident energies. The origin of this effect was discussed in ref. [138]: in general, to calculate the interaction potential for elastic scattering, one should include all possible virtual couplings between the gs and higher excited states, or reaction couplings. These processes remove flux from the elastic channel. This effect is negligible for stable nuclei, but may become significant for weakly bound nuclei. In particular, for exotic isotopes with lower particle thresholds, the coupling effects between the gs and the continuum states are expected to increase. To understand the effects observed in the elastic scattering in the case of a weakly bound nucleus, it is useful to go back to the general expression for the effective interaction potential between a target nucleus denoted T and a projectile P.

As proposed by Feshbach in his theory and fully explained in refs. [139,140], the elastic potential may be developed with two contributions,

$$U_E = V_{00} + \lim_{\varepsilon \to 0} \sum_{(\alpha,\alpha') \neq (0,0)} V_{0\alpha} \left(\frac{1}{E - H + i\varepsilon} \right)_{\alpha\alpha'} V_{\alpha' 0}, \quad (17)$$

where the sum is taken on all the possible excited states of the nuclei. The first term V_{00} describes only the projectile-target PT interaction, for the 2 nuclei remaining in their gs ϕ_{p0} and ϕ_{t0}, the gs densities are folded with the effective in-medium NN interaction v_{NN}:

$$V_{00} = (\phi_{p0}\phi_{t0} \mid v_{NN} \mid \phi_{p0}\phi_{t0}). \quad (18)$$

The second term of the U_E potential of eq. (17) was described as a dynamical polarization potential (DPP) in ref. [138], but here, we prefer to call it the *Virtual Coupling Potential* (VCP), since it may arise from many processes such as transitions to bound, unbound or continuum states, coupling to transfer reactions. It is complex, non-local and energy-dependent. It is illustrated in fig. 8, with the parts corresponding to the transition terms $V_{0\alpha}$, $V_{\alpha' 0}$ and between $\alpha\alpha'$. The ability of the G-matrix microscopic potentials to reproduce the elastic scattering is observed when the influence of the coupled reaction channels is small, which is in general the case for stable nuclei for which the imaginary part of the potential is enough to account for the influence of the higher-order effects generated by the second term of U_E. The phenomenological imaginary part obtained for the global potentials mainly originates from this term. In the case of the proton-nucleus elastic scattering, V_{00} may be represented by the JLM potential, and the imaginary part of this potential accounts for a part of the VCP. But in general, the low-lying threshold coupling to reaction channels induces a modification of the entrance channel potential. In various approaches, starting from a microscopic density-dependent potential, if the elastic data cannot be reproduced, whatever the density inputs, it means that the reaction coupling effects have to be included, either phenomenologically (modification of the entrance potential) or microscopically (explicit treatment of the reaction channels coupling). The discrepancies observed between experimental elastic cross sections and the microscopic calculations [28] and the need to reduce the real entrance channel potential, as shown in fig. 7, are some examples for the phenomena of reaction couplings. They have to be taken into account in the reaction framework before discussing the sensitivity to the structure inputs. In the case of the exotic nuclei, the influence of the coupling effects may be larger. For instance,

due to the low particle threshold energies, the reaction channels (p,d) (p,t) may be playing a significant role in the reaction analysis of the (p,p) scattering.

The full exact microscopic calculation of the VCP remains an open question: looking at eq. (18), it would require the precise knowledge of the spectroscopy of the nucleus and of the transition strenghs to bound and continuum excited states. It is then difficult to evaluate and is not taken into account in the usual optical model approaches. It was explained in refs. [141,142] that a complex surface potential, with a repulsive real part, is expected to simulate the surface effects generated by the VCP and this corresponds to the reduction of the real part. If we focus on the direct reactions induced by ^{6}He, the first indication was given in the analysis of the elastic scattering of ^{6}He on ^{12}C using double-folding potentials [136], and in the analysis [137], with the microscopic JLM potential of the ^{6}He + p scattering measured at 71 [143], 38.3 [137] and 25 $A \cdot$ MeV [144,145]: by reducing the real part of the JLM potential, we have reproduced successfully the whole set of data. As discussed in previous works about the elastic scattering of ^{10,11}Be(p,p) [146,147], it may occur that the coupling to specific (p,d) channels has a deep influence on the elastic scattering. In the phenomenological approach, this is seen by a modification of the elastic potential, for instance a significant (20% decrease) change of the real depth. In the coupled reaction channel framework, the elastic data can be reproduced by coupling explicitly the main channels contributing to the loss of flux of the elastic channel.

4.6 Sensitivity of the (p,p) distribution to the density

To show the sensitivity of the elastic scattering to the rms radii or to the density profile of the structure inputs, we have used several sets of densities to generate the JLM potentials at 38.3 $A \cdot$ MeV. First, in fig. 9, using the standard JLM for light nuclei ($\lambda_V = 1$, $\lambda_W = 0.8$), we compare the calculated cross sections. We have considered either the microscopic densities, *HF corr* or 3-body model $fc6$ with r_m radius of 2.22 and 2.5 fm, respectively; or the standard density distributions:

- a density without neutron halo extension, obtained with the simplest form for proton and neutron densities of light nuclei; it is chosen as a Gaussian distribution function,

$$\rho(r) = \rho_0 * \exp[-(r/a)^2], \tag{19}$$

  the ρ_0 factor is normalized on the nucleon A number, and a is adjusted to have the same r_m radius as the *HF corr* one;
- a "stable-like" density with homothetical proton and neutron densities: $\rho_n = (N/Z)\rho_p$, the proton density is the one of *HF corr* case; in this case, the r_m radius is 1.9 fm. This type of density corresponds to the usual one of the light stable nuclei, for which the proton and neutron densities have similar shapes in the N/Z ratio; as a consequence the r_p, r_n and r_m radii are equal.

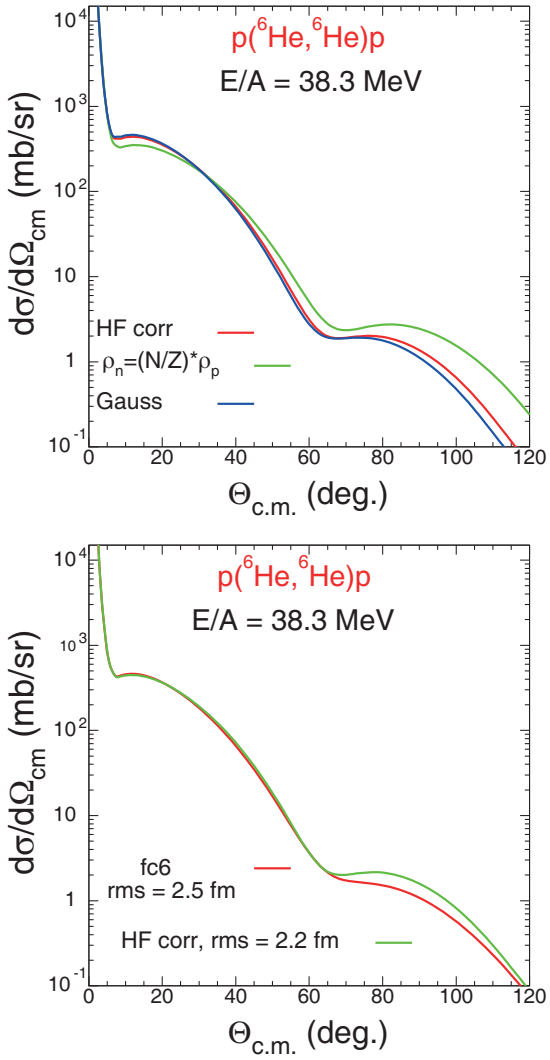

Fig. 9. Cross sections of the elastic scattering ^{6}He(p,p) at 38 $A \cdot$ MeV. comparison of the standard JLM ($\lambda_V = 1$, $\lambda_W = 0.8$) calculations done with various models for the densities: (top) *HF corr* and Gaussian (Gauss) one with the same r_m radius of 2.2 fm and a "stable-like" one with $r_m = 1.9$ fm; (bottom) $fc6$ and *HF corr*.

The Gaussian density used for the (p,p) calculations shown in fig. 9 (top) has the same shape for p and n and a rms radius of 2.22 fm. Proton and neutron densities of ^{4}He can be modelled with a similar Gaussian shape resulting in the total matter density (rms of 1.46 fm) which was shown in fig. 1 with the $fc6$ matter density. Since the core nucleus is considered as similar to the alpha particle in the FB model for $fc6$, the calculated proton density of $fc6$ is found close to the one of ^{4}He. For comparison, the r_p value of the $fc6$ density is 1.94 fm, the one of the Gaussian used for the test calculations of the (p,p) distributions is 1.9 fm.

If we consider the proton scattering distributions calculated at 38 $A \cdot$ MeV (fig. 9) and discuss the effects due to the shape of the density, rms radii:

- In fig. 9 (bottom), $fc6$ and *HF corr* both have extended neutron densities, similar proton densities and

differ by their rms radii by less than 0.3 fm; the difference in the angular distributions can be seen for angles above $60^\circ_{c.m.}$ but in this angular domain, several coupled-reaction channel effects may also play a role, and would result in larger modification of the cross sections than expected from the change of rms or shape needed in the input densities to reproduce the data. Moreover, for angles $> 60^\circ_{c.m.}$, the data are in general obtained with larger statistical error bars. The angular region on which we can rely on for our discussion of the structure effects is the one between 20 and $60^\circ_{c.m.}$.
– Between the stable-like case ($r_m = 1.9$ fm), and the *HF corr* densities ($r_m = 2.2$ fm), the difference is observed for the r_n radii, (and the r_m radii) differing by 0.3 fm. Between the *HF corr* with halo and the Gaussian-type density (no halo), the densities have the same r_m and different shapes and r_n radii.

For the quantitative discussion, to compare the calculated cross sections to the data, we will first apply the prescription related to the global effect of the VCP on the cross sections, using the modified JLM (with the reduced real part, as discussed in the previous section). The results of these calculations done using several model densities are presented in fig. 10. To discriminate between the density models —with similar r_m within ± 0.1 fm and different shapes and neutron r_n radii— we can see, in fig. 10 (top panel), that it is needed to extend the measurement for c.m. angles above 80° with small statistical error bars ($< 10\%$); but, in this range, for incident energies of few $10\,A \cdot$ MeV, the cross sections are less than 1 mb/sr, and usually the statistical error bars of the available data are larger (specially for exotic beams, with small intensities). Several shapes and extension for the rms radii were assumed (fig. 9) but the ones which correspond to a satisfactory agreement (in terms of χ^2 minimization), from 20 up to 60°, are the *HF corr* and $fc6$, excluding the "stable" density with $r_m = 1.9$ fm (fig. 9(top), fig. 10); angles between 20 and $40^\circ_{c.m.}$ are better reproduced by the densities with the larger rms, around 2.5 fm, with a sensitivity of ± 0.1 fm. In this region, a direct effect of the rms change can be observed on the magnitude of the distributions. From the comparison of the various shape/rms of the densities, the data are well reproduced using the densities associated to the neutron tail and the rms value between 2.5 ± 0.1; using the Gaussian density with the same r_m value as for $fc6$ (fig. 10), we observe discrepancies between the calculated distributions and the data, even for the angular range between 40 and $60^\circ_{c.m.}$, this density is built with a proton density having the same large rms radius, and this is not consistent with the data.

In summary, from the measurement of the (p,p) data for angles between 10 to $80^\circ_{c.m.}$, we can obtain insight onto the r_m value and check which model densities give the most consistent agreement of the calculated distributions with the data for the different angular ranges. Quantitative agreement in terms of χ^2 mean-square value between theory and data can be searched for the region where the statistics is large enough (typically between 20 and $60^\circ_{c.m.}$, where the cross sections are measured with error bars less than 10%). Through the comparison of the proton elastic data with the various calculations, depending on the r_m radii, it is possible to estimate the r_m radius with a sensitivity of ± 0.1 fm. Densities with the same rms radius but different shape (for instance considering either a halo-type density with neutron extension, or a compact Gaussian-like density) would be distinguished via comparison to data provided the measurement be done at large angles, above $80^\circ_{c.m.}$. In this region, the statistical error bars are larger; however, it may be considered for qualitative discussion on the shape of the density.

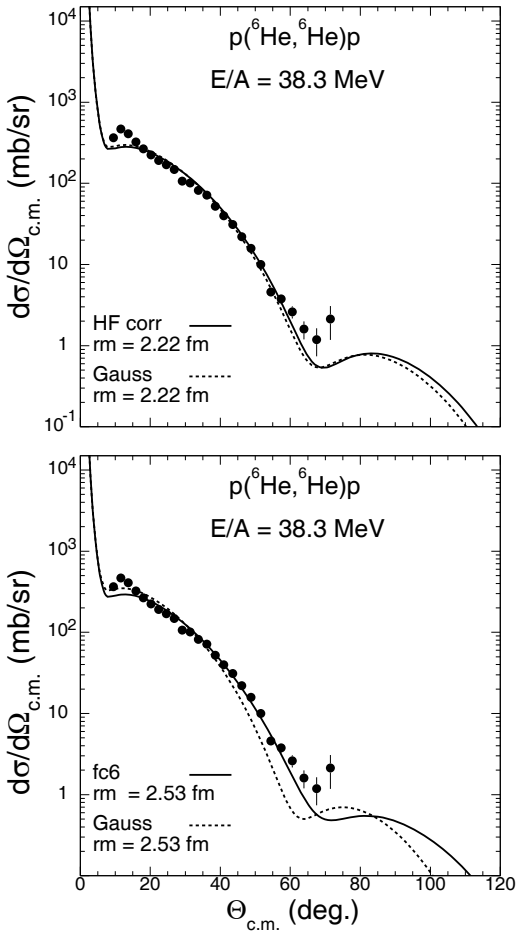

Fig. 10. Cross sections of the elastic scattering ^{6}He(p,p) at $38\,A \cdot$ MeV, comparison of the data with the calculations done using the JLM potential ($\lambda_V = 0.8$, $\lambda_W = 0.8$) with two models for the densities.

We can conclude that, in the case of the elastic ^{6}He+p, in the energy domain between $25A$ and $100\,A \cdot$ MeV, the angular distributions are well reproduced with a microscopic potential computed with a realistic (in terms of r_m radius) ^{6}He density, provided that the "bare" elastic potential be changed, with a reduction of the real part. In sect. 6.4, we will see that, for the $^8\mathrm{He} + \mathrm{p}$ data at lower incident energies, $15\,A \cdot$ MeV, the cross sections are larger than 1 mb/sr, even for the c.m. angles between 60 and 120°. In this case, the sensitivity to the neutron-proton difference can be checked. In sect. 5.3 it will also be shown

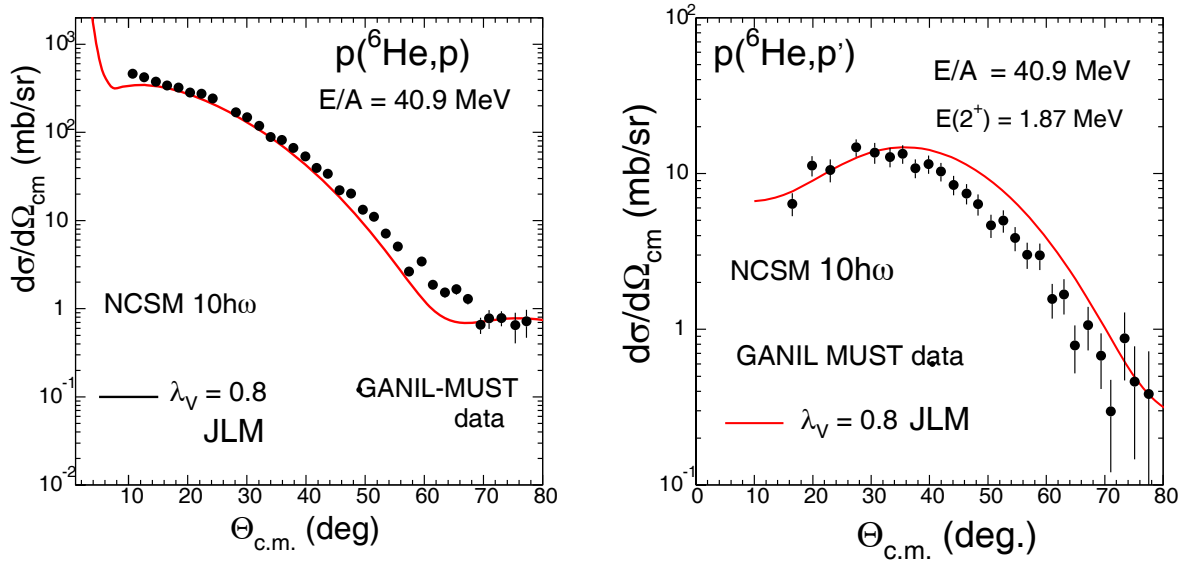

Fig. 11. Experimental and calculated cross sections for ^{6}He(p, p′) at 40.9 $A \cdot$ MeV. The data obtained at GANIL with the MUST telescopes are from ref. [113]. The JLM potential (with $\lambda_V = 0.8$, $\lambda_W = 0.8$) is generated using the NCSM densities.

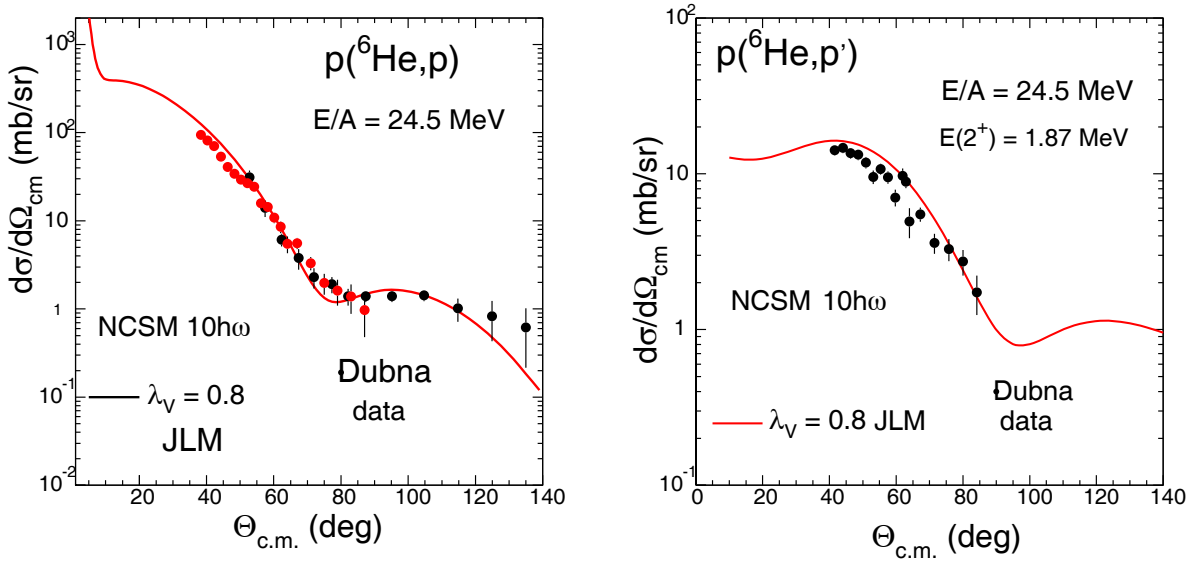

Fig. 12. Experimental and calculated cross sections for elastic and inelastic ^{6}He(p, p′) at 24.5 $A \cdot$ MeV. The data [144,145] were obtained at Dubna. The JLM potential (with $\lambda_V, \lambda_W = 0.8$) is generated using the NCSM densities. See details in the text.

that the combination of the (p,p) and (p, p′) data can give us an insight onto the r_m and r_n radii.

5 Investigation of the ^{6}He structure

5.1 Structure models for the interpretation of the (p, p′) data

The ^{6}He(p, p′) scattering data to the 2_1^+ state at 1.8 MeV were measured at 40.9 [113] and at 24.5 $A \cdot$ MeV [145]. In a first approach, the ^{6}He(p, p′) angular cross sections will be calculated using the JLM potential to generate the entrance channel and transition form factor potentials with microscopic *gs* and transition densities from the NCSM (sect. 5.2). In a second step, to test the density profiles and the $M_{p,n}$ values consistent with the data, we will adopt a set of phenomenological densities (sect. 5.3).

5.2 Analysis of ^{6}He(p, p′) using NCSM densities

The ^{6}He *gs* and transition densities included in the JLM potential are the ones deduced from the One Body Density Matrix Elements given by the large basis NCSM calculations [69, 148]. In figs. 11 and 12, we test the *gs* and transition densities predicted in the 10 $\hbar w$ NCSM [71, 81] with the characteristics given in table 8.

The solid curves are calculations using the JLM potential with the reduced real part ($\lambda_V = 0.8$), according

Table 8. Characteristics of the ^{6}He gs and transition densities, binding energy $|E_b|$ and excited state E_x calculated within the NCSM framework with 4 or $10\hbar\omega$ space [70,71].

NCSM	E_b (MeV)	r_m (fm)	r_p (fm)	r_n (fm)	Δr (fm)
$4\hbar\omega$	25.65	2.12	1.78	2.27	0.49
$10\hbar\omega$	26.7	2.18	1.76	2.36	0.60
NCSM	E_x (MeV)	$B(E2)$ e^2 fm^4	M_p fm^2	M_n fm^2	M_n/M_p
$4\hbar\omega$	2.69	0.507	−0.712	−6.58	9.2
$10\hbar\omega$	2.63	1.056	1.027	7.729	7.5

to our prescription discussed in sect. 4.5, to simulate the effect of the VCP. The transition form factor potential is calculated with the transition densities corresponding to a $B(E2)$ value of $\simeq 1.06\, e^2 \cdot \mathrm{fm}^4$, and to the ratio $|M_n/M_p| = 7.5$. This ratio is large compared to the value $(N/Z = 2)$ associated to a standard isoscalar excitation.

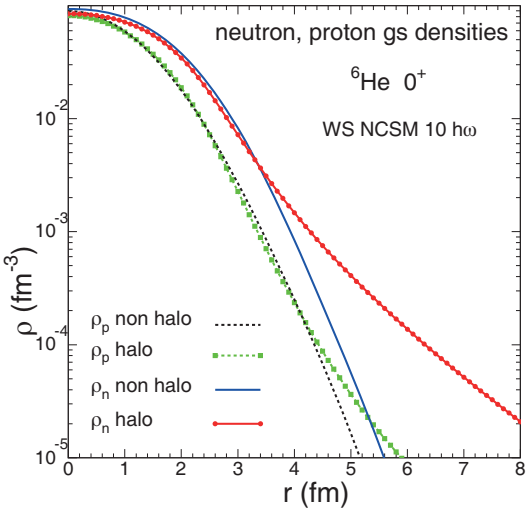

Fig. 13. Distributions of the proton and neutron densities for the ^{6}He gs, calculated from the NCSM model using WS potentials [113].

5.3 Interpretation of ^{6}He(p, p′) using Tassie-form densities

The single particle (SP) wfs which describe the nucleon bound states were generated using WS potentials for two different options [113,149]. In the first, denoted as "non-halo" case, the calculations were performed using SP wfs as specified from the simplified shell model. In the second, designated as "halo" case, the WS potentials were adjusted [149], to produce the $0p$-shell binding energy of 2 MeV, which is close to the experimental single-neutron separation energy of ^{6}He. The resulting gs densities are shown in fig. 13.

For multipolarity $l \geq 2$, a simple analysis of the (p, p′) can be performed using: i) a simple isoscalar shape vibration of the density, with the transition matter density expressed as (δ^l_m the matter deformation length),

$$\rho^{tr,l}_{p(n)}(r) = -\delta^l_m \frac{\mathrm{d}\rho_m}{\mathrm{d}r}\,, \qquad (20)$$

this is referred to as the "Bohr-Mottelson prescription" [52];

ii) the phenomenological Tassie (hydrodynamic) form [28] for the densities, for which the proton (p) or neutron (n) transition density is obtained by derivating the gs density $\rho_{p(n)}$ and it is written, with the multipolarity l,

$$\rho^{tr,l}_{p(n)}(r) = -\alpha^l_{p(n)} r^{l-1} \frac{\mathrm{d}\rho_{p(n)}}{\mathrm{d}r}\,. \qquad (21)$$

The proton density can be normalized with the α^l_p by requiring that its moment $|M_p|$ should satisfy the eq. (7) with the electric quadrupole transition probability $B(E2)$. For bound 2^+ states, the $B(E2)$ value can be obtained by Coulomb excitation measurements. $|M_n|$ can then be deduced by adjusting the calculated (p, p′) on the data. A simple form may be adapted for the gs density, for instance proton and neutron densities can be calculated using the 2 parameter-Fermi (2pF) functions, with integrals normalized to the N, Z numbers and diffuseness and radius adjusted so as to mimic the microscopic densities of fig. 13:

$$\rho_{p,n}(r) = \rho^0_{p,n}\left[1 + \exp\left\{\frac{r - R^o_{p,n}}{a_{p,n}}\right\}\right]^{-1}. \qquad (22)$$

In ref. [47], for the light stable nuclei, several nuclear density functions were tested and validated on the sets of elastic scattering data. To have a realistic description, the density function may be found close to a Gaussian shape, with parameters adjusted on the microscopic structure calculations done in an Harmonic Oscillator potential basis (*e.g.*, ^{6,7}Li, ^{9}Be), for nuclei better described with more correlations and larger sizes of the wfs the 2pF density function is widely used and can be adjusted on the structure characteristics (diffuseness, radius) found in the HF calculations. The microscopic origin of the derived 2pF functions and of their parameters was explained by Bohr and Mottelson in ref. [52]. For instance, the ^{12}C densities can be modelled as 2pF, and they are used to describe successfully the (p,p) data. By comparison of the (p, p′) data with the JLM calculations, several configurations can be tested for the gs and transition densities. We carry out a set of (p, p′) calculations using the transition densities with a Tassie-form generated from the (p) and (n) gs densities shown in fig. 13, and noted as *halo*, or *non-halo* or *halotot*. The characteristics of their rms radii values are given in table 9: in the non-halo case, the matter rms radius r_m is equal to 2.2 fm, the *halotot* density corresponds to a large extension of the neutron density ($r_n = 2.7$ fm) with r_m equal to 2.5 fm.

Table 9. Rms radii of the matter, proton and neutron 2pF distributions of ^{6}He used for the (p, p') calculations.

^{6}He	r_m (fm)	r_p (fm)	r_n (fm)	Δr (fm)
Non-halo (p,n)	2.17	2.00	2.24	0.24
Halo n	2.51	2.00	2.72	0.72
Halotot (p,n)	2.51	2.03	2.72	0.69

The interaction potential for the entrance channel (elastic) is calculated using the JLM interaction and the *gs* 2pF densities. The form factors needed for the DWBA calculations of the (p, p') scattering are obtained with the various sets of transition densities. The following cases are considered, with the M_n moment adjusted from the comparison between the data and the calculations:

- Tassie-type density *non-halo*, obtained from the *gs* noted p, non-halo and n, non-halo. The M_p (defined as in eq. (7)) is fixed to the value 1.77 fm^2, corresponding to the $B(E2)$ value of $3.1 \pm 0.6\, e^2 \cdot \text{fm}^4$ discussed in ref. [150] and inferred from the experimental studies of the ^{6}He Coulomb excitations. The M_n/M_p moment is adjusted to reproduce the (p, p') data which gives the ratio $M_n/M_p = 2.75$, corresponding to $M_n = 4.85\,\text{fm}^2$. These calculated (p, p') cross sections have the same order of magnitude as the ones (*non-halo*) calculated in the article [113].
- *halo*, obtained using Tassie-derivative form from the 2pF adjusted on the *gs* densities denoted p, non-halo and n, halo. To reproduce the (p, p') data, we have to renormalize the neutron transition densities which gives M_n/M_p equal to 4.4. The obtained value is then $M_n = 7.81\,\text{fm}^2$.
- *halotot*, density: the p,n transition densities are deduced from the *gs* densities p halo and n halo. The p transition density is normalized to $M_p = 2.44\,\text{fm}^2$ corresponding to a $B(E2)$ equal to $5.94\, e^2 \cdot \text{fm}^4$. The M_n/M_p value adjusted on the (p, p') is equal to 3.2, giving $M_n = 7.80\,\text{fm}^2$.

The various tested transition densities are presented in fig. 14, and their characteristics are summarized in table 10.

In ref. [113], it was shown that the experimental angular distributions of the (p, p') cross sections were in agreement with the non-local calculations done using the *halo* configuration for the structure inputs. Here within a local optical model approach using the JLM potential and radial densities, the calculations using spatially extended *halo* densities are in agreement with the data. The findings of ref. [113] are confirmed and we also show a realistic radial shape for the ^{6}He *gs* and transition densities. These densities can be useful for further calculations of direct reactions induced by ^{6}He based upon a microscopic density-dependent optical potential. Using this simplified approach, it was possible to explore various test cases for the shape and to vary the magnitude of the radial transition densities. In fig. 15, the dashed and solid curves are calculations done with the JLM potential, using

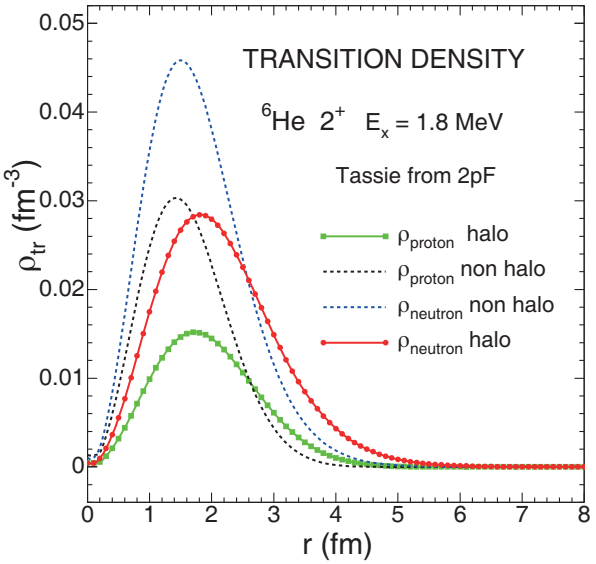

Fig. 14. Distributions of proton and neutron transition densities from *gs* to the 2$^+$ excited state of ^{6}He, obtained with the Tassie method and adjusted as explained in the text.

Table 10. $M_{n,p}$ moments of the ^{6}He densities tested in the (p, p') analysis, presented in fig. 14. They correspond to the definition in eq. (7), $B(E2, 0^+ \to 2^+) = e^2 |M_p|^2$.

Density Tassie	M_p fm^2	M_n fm^2	M_n/M_p	$B(E2)$ e$^2 \cdot$ fm^4
non-halo	1.77	4.85	2.75	3.14
halo	1.77	7.81	4.4	3.14
halotot	2.44	7.80	3.2	5.94

the prescriptions for the potential parameters: $\lambda_V = 0.8$, $\lambda_W = 0.8$, discussed in the elastic analysis. The dashed and solid curves correspond to the "non-halo" and "halo" options, respectively. Within this analysis the comparison with the data sets is in favor with the halo configuration, as in ref. [113]. Moreover, within this local microscopic approach using the JLM potential, we can provide a realistic shape for the neutron and proton *gs* and transition densities, that can be easily compared to the ones calculated for ^{6}He within various structure theories.

Another test case was considered to illustrate the weak sensitivity of the (p, p') observables to the proton transition density and to the corresponding $B(E2)$. The calculations using the "*halotot*" and "*halo*" densities are compared in fig. 16, the only change between the two cases is the proton density. The $B(E2)$ value for the "*halo*" case is twice the one of "*halotot*" but no significant change is observed for forward angles, and the modification of the p transition density does not affect significantly the (p, p') cross sections in the whole angular range covered by the data.

A precise analysis including directly the effects of the couplings to the continuum was done using the Coupled Discretized Continuum Channels calculations (CDCC) and a dineutron model for ^{6}He [151]. It was applied to the ^{6}He + p elastic, inelastic and transfer data measured

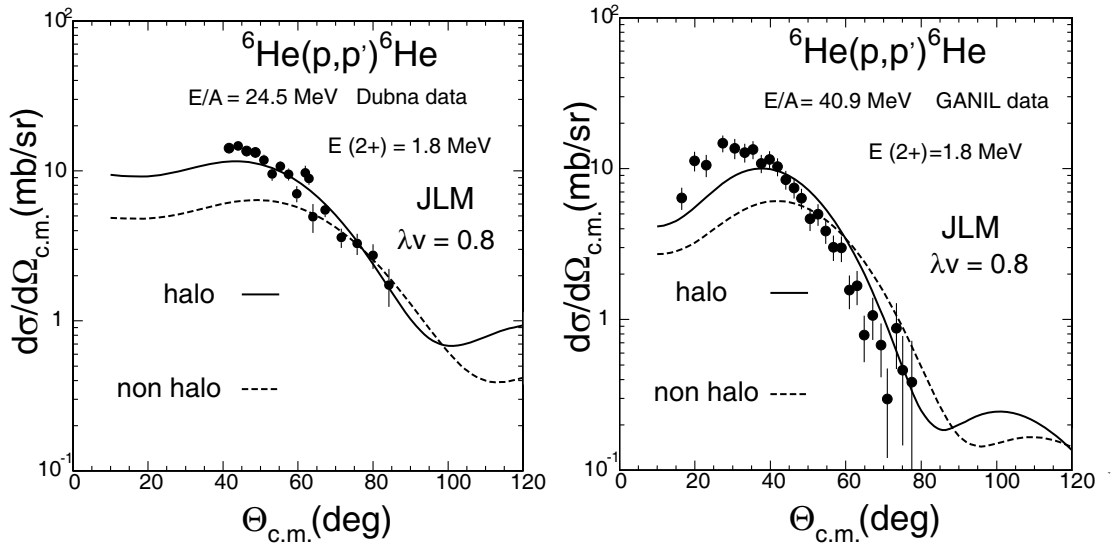

Fig. 15. Comparison between the experimental and calculated (p, p') cross sections for ^{6}He at 24.5 $A \cdot$ MeV (data: full circles [145]) and at at 40.9 $A \cdot$ MeV (data at Ganil with the Must Detector [113]), considering two types of densities for ^{6}He, denoted as *halo* (thick red line) or *non-halo* (black line).

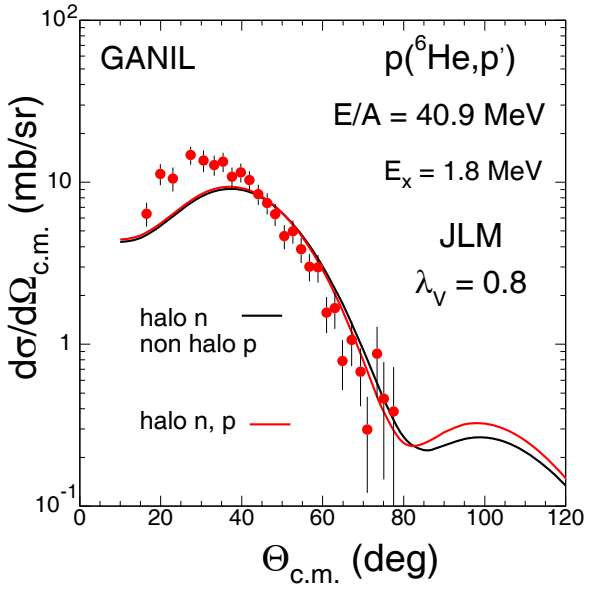

Fig. 16. Experimental cross sections for ^{6}He(p, p') from 0^+ *gs* to the 2^+, at 40.9 $A \cdot$ MeV (data points from [113]) compared to JLM calculations, one using a Tassie density noted as *halotot* (red curve) the other is the *halo* one (black). These densities are presented in fig. 14. The same neutron "halo" transition density is included in these (p, p') calculations.

at Dubna at 25 $A \cdot$ MeV. It helps in determining the influence of the coupling effects. From the explicit treatment of the coupling, the microscopic origin of the VCP term for ^{6}He + p can be shown.

From these calculations, we can directly check the sensitivity of the calculated (p, p') cross sections with the density-dependent form factors. First, we have checked the validity of the reaction model calculations, by comparing the elastic scattering data with the calculations done using the optical potential, with no explicit coupling. As we have seen before, the discrepancies indicate the possibility that the reaction fluxes in the entrance channel are modified by other processes. We may either treat these coupling explicitly, if we have an insight into the main reaction processes at play, or treat them phenomenologically: for instance, in some cases, we can simulate these effects by reducing the real part of the potential. This change of the potential may be applied for the entrance potential of the (p, p') calculations. In the present stage of the calculations, if our goal is to test the structure inputs, we can rely on a simpler approach for the potential and include implicitly the coupling effects by applying our prescription of the 20% of reduction, which was shown to be enough to understand the data collected from 20 to 75 $A \cdot$ MeV within an angular range from 15 up to $100^\circ_{c.m.}$. However, when it is possible, a better approach is to handle directly and explicitly the coupled reaction channel calculations to fix the coupling and to determine the microscopic origin of the potential. But the full calculations with (p, p') and (p,d) may turn out to be too complex due to the unknown coupling strength that we have to introduce in the complete coupling scheme. In the case of the ^{8}He data at low energy, we will see in sect. 6.3 that this simplified approach for the coupling effects with a global reduction of the real part, is not sufficient to reproduce the data. The complete framework needed in this case will be discussed.

6 Investigation of the ^{8}He structure via (p, p') scattering

To characterize the ^{8}He structure, we will analyze several data sets of ^{8}He on proton, to check the consistency of our structure inputs and reaction model framework:

Table 11. Rms radii (fm) of the calculated *gs* ^{8}He densities discussed in the text.

Density model	Ref.	r_p fm	r_n fm	r_m fm	Δr fm
COSMA	[43]	1.69	2.74	2.52	1.05
HF corr	[72]	1.95	2.67	2.51	0.72
NCSM$_{v3\text{eff}}$	[70,71]	2.00	2.59	2.46	0.59
NCSM$_{\text{cd}}$	[84]	1.88	2.80	2.40	0.92
NCSM$_{\text{inoy}}$	[84]	1.74	2.60	2.40	0.86
AMD-m56	[65]	1.96	2.63	2.48	0.67
FMD	[67]	1.97	2.67	2.53	0.70
COSM	[90]	1.86	2.75	2.52	0.89
TOSM	[91]	–	–	2.44	–
GSM11	[87]	1.88	2.77	2.58	0.89

– elastic scattering data ^{8}He(p, p), measured at 32, 66, 73 $A\cdot$MeV [143] and at 72 $A\cdot$MeV [63], the JLM calculations are discussed in sect. 6.2;
– the SPIRAL (p,p) data at 15.6 $A\cdot$MeV [116]; the phenomenological analysis is presented in sect. 6.3,
– (p,d) reaction channel measured at the same energy [115]; it is included in the CRC analysis in sect. 6.4;
– inelastic data at RIKEN (p, p′) RIKEN at 72 $A\cdot$MeV [63]; it is calculated in the JLM framework in sect. 6.6;
– the (p,t) data at 15.6 $A\cdot$MeV [117,118], and extended (p,t) data set at 15.4 $A\cdot$MeV [119], compared to calculations in sect. 7.1.

6.1 ^{8}He structure models

The characteristics of the ^{8}He densities calculated within several theoretical frameworks are given in table 11. *COSMA* is the density given by the 5-body model [43]; the results from the calculations done within the NCSM framework, using the $V_{3\text{eff}}$ ($4\hbar\omega$ space, 13 MeV), CD Bonn and INOY interactions, are noted NCSM$_{v3\text{eff}}$, NCSM$_{\text{cd}}$ and NCSM$_{\text{inoy}}$ respectively. For the elastic data analysis, the density sets from the *COSMA*, "*HF corr*" and NCSM$_{v3\text{eff}}$ models will be tested. and finally, a summary plot of the rms radii of this table, compared to the ^{8}He(p, p′) results will be presented. The p, n, and matter density profiles given by the NCSM$_{V3\text{eff}}$ are shown in fig. 17. The distributions for the 3 models are compared in the plots of fig. 18, showing difference in the behaviour of the core or tail densities between the compact α core of the *COSMA* density (well seen in the matter density plot in linear scale), and the larger n density produced by the *HF corr* model at large radii.

6.2 Analysis of the ^{8}He(p, p) proton elastic data measured at RIKEN

Elastic scattering data ^{8}He(p, p) were measured at 32, 66, 73 $A\cdot$MeV [143] at RIKEN, covering an angular domain

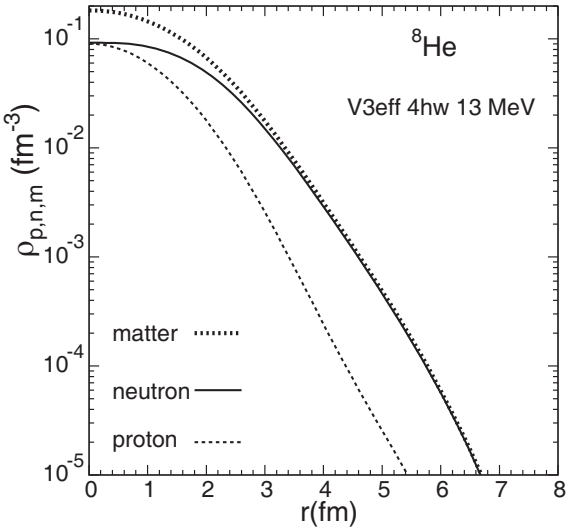

Fig. 17. Densities of ^{8}He in the NCSM model approach, calculated as explained in ref. [83] using $3N$ effective interactions and model space corresponding to $4\hbar\omega$ ($\hbar\omega = 13$ MeV).

up to $60^\circ_{c.m.}$. It was obtained around 700 $A\cdot$MeV [94] at GSI at the most forward angles. As discussed in sect. 3.2, the analysis can provide the matter rms radii but the data set lacks sensitivity to establish the tail of the wf. The microscopic JLM form factors are used to generate the entrance and transition potentials using the densities shown in fig. 18, with rms radii given in table 11. These densities are obtained with different assumptions on the *pn* correlations, which can be seen on their neutron-skin thickness $r_n - r_p$, given with the rms radii in table 11. In fig. 20, we compare the ^{8}He + p data at 72 $A\cdot$MeV [63] with the JLM calculations. The small difference of few mb/sr between the calculated cross sections cannot be separated by comparison with the data, due to the large statistical error bars at c.m. angles above $50^\circ_{c.m.}$. To investigate the sensitivity of the angular distributions to the microscopic parameters of the reaction analysis, like proton and neutron densities, data up to c.m. angles around $90^\circ_{c.m.}$ are needed with enough statistics to obtain error bars below 10% in this region.

6.3 Discussion of the ^{8}He(p, p) at 15.7 A · MeV

The data set obtained at 15.7 $A\cdot$MeV [116] at GANIL has a large angular range, from small forward (20°) to ($110^\circ_{c.m.}$) angles, which gives the possibility to have a deeper understanding of the characteristics of the entrance potential and to make tests of the density inputs. The JLM potential is calculated with the various density sets used for the analysis done at 72 $A\cdot$MeV, with the standard normalization factor of the imaginary part $\lambda_W = 0.8$ (prescription of the LDA for the light nuclei), and with the normalization factor of the real part $\lambda_V = 0.8$, to take into account the modification of the potential due to the weakly bound nature of the light nuclei, as explained previously in sect. 4.5. As illustrated in fig. 21, the (p,p) data

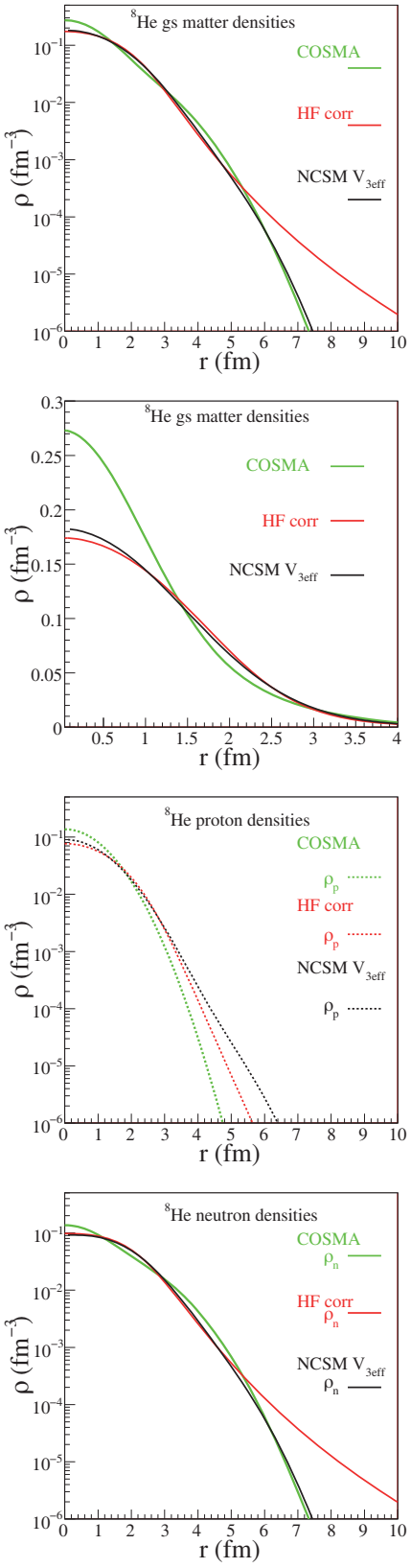

Fig. 18. Nuclear matter (top, in logarithmic and linear scales) and proton, neutron (bottom panel) densities of ^{8}He within various frameworks: NCSM, HF (with correlations) denoted as *HF corr*, few-body model (*COSMA*).

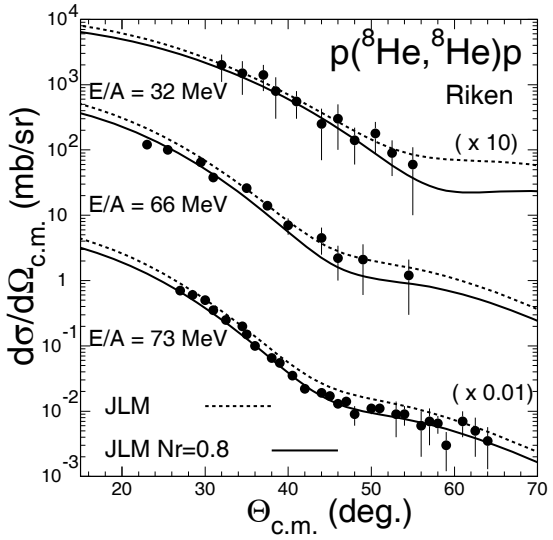

Fig. 19. Data for the elastic scattering ^{8}He(p, p) between 25 and 100 $A \cdot$ MeV, from ref. [143]. (The cross sections at 32 and 73 $A \cdot$ MeV were multiplied by 10 and 0.01 respectively.)

is not reproduced when we reduce the real part of the entrance potential (top plot), contrarily to the situation encountered for the other data set at higher energies. The data cannot even be reproduced by changing both the real and imaginary parts of the JLM potentials: a search on the normalization parameters λ_V and λ_W was made to obtain the best agreement with the data, for the various JLM calculations done using the but the most forward angles cannot be reproduced (right plot). If this part of the angular distributions, for angles between 20 and 35, is treated separately for the search, it would require change of the parameters by more than 40% (like $\lambda_V > 1.5$ and/or $\lambda_W < 0.5$), but then the data beyond $35^\circ_{c.m.}$ are not reproduced. If we adopt a stronger λ_W value, we could reproduce the larger angles but not the small angles. The forward and backward angles are not reproduced by any (λ_V, λ_W) combinations, showing that the required potential does not correspond to the modifications of the real/imaginary parts with a global reduction or increase factor. This is a signature for the strong coupled reaction channel effects that we have to take into account explicitly in the interpretation. The renormalization is only the way to simulate coupling effects of repulsive nature (for a VCP acting mainly on the real part) or stronger absorptive effects (producing larger imaginary parts).

The renormalization factor found for the energy regime above 25 $A \cdot$ MeV was roughly satisfactory (sect. 4.5, fig. 7 for ^{6}He and figs. 19 and 20 for ^{8}He). It has to be underlined that that same increase of cross sections at the most forward angles was observed in ^{6}He(p,p) at 38.3 $A \cdot$ MeV (fig. 10); this increase is beyond a simple renormalization of the real/imaginary entrance potential. Here, to describe the angular distributions obtained at lower energies, and with a wider angular extension up to $110^\circ_{c.m.}$, the simple modification of the potential, with the renormalization factor, is not enough to account for the coupling effects induced by the virtual coupling potential (VCP). Now,

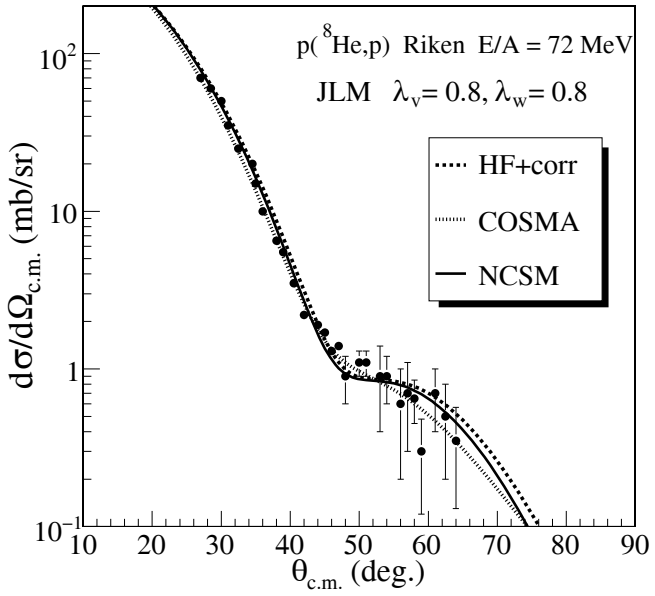

Fig. 20. Cross sections for the elastic scattering ^{8}He(p, p) at 72 $A \cdot$ MeV, comparison of the RIKEN data from ref. [63] with the calculations done using three models for the densities.

we need to decipher the origin of this VCP, and to find explicitly the reaction coupling effects which produce the deep change onto the entrance potential. It means that the interpretation should go beyond the initial optical model inputs and would require a change in the reaction model itself, to include the strong coupling effects induced on the ^{8}He + p system at 15.7 $A \cdot$ MeV. The understanding of the shape of the angular distributions and of the modification of the OMP will be obtained within the CRC model discussed in the next sections; the microscopic origin of the phenomena will be explained, and the corresponding "realistic" entrance channel potential —which gives a good description of the data on the overall angular range— will be extracted.

6.4 CRC approach of the ^{8}He(p, p) at 15.7 A · MeV

In the kinematical spectrum of fig. 5, the observed relative yields for the elastic and the inelastic scattering to the 2^+, and for the (p,d) and (p,t) reactions shows that the transfer (p,d) data is of the same order of magnitude as the elastic data for the forward angles. For nuclei close to stability, the large S_n, S_{2n} thresholds give large negative Q-values for the 1n (p,d) and 2n transfer (p,t) reactions. For weakly bound nuclei, the positive (or close to 0) Q-values may enhance the coupled reaction effects: Q-values for ^{8}He(p,d) and (p,t) are at −0.31 and 6.36 MeV respectively. This corresponds to the large yields of the (p,d) reaction we found (fig. 22), above 10 mb/sr for angles below $55^\circ_{c.m.}$, larger than the elastic cross sections. Previously, various data sets were available for (p, p′) scattering at 72 $A \cdot$ MeV [63], (p,d) transfer reaction at 35A [152], (p,t) at 61.3 $A \cdot$ MeV [153], but these transfer reactions were

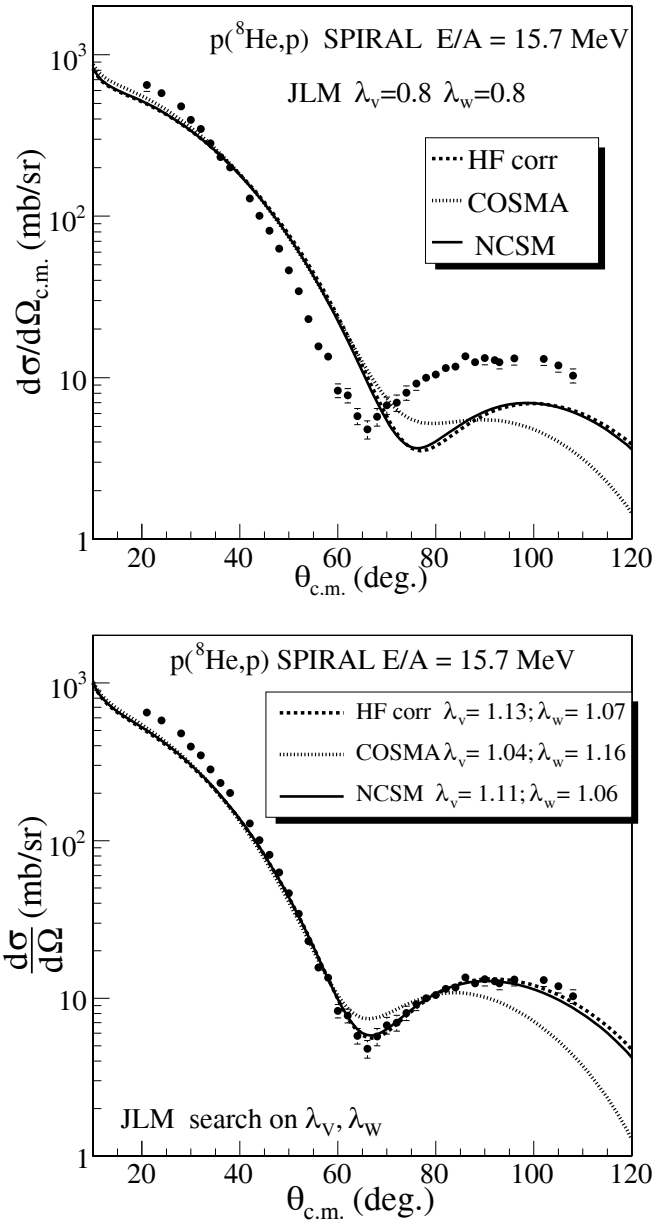

Fig. 21. Elastic scattering ^{8}He(p, p) at 15.7 $A \cdot$ MeV; the SPIRAL-MUST2 data [116] are compared to the JLM calculations done using three different densities, and the following normalized factors for real and imaginary parts: (top) parameters $\lambda_V = 0.8$ (for weakly bound nuclei) and standard $\lambda_W = 0.8$; (bottom) calculations done with the potentials resulting from a search on λ_V and λ_W, made to reproduce the data.

measured each time with different beam incident energies, without the elastic data. All these data were found consistent with the *COSMA* model, but they were not complete in terms of angular range and reaction channels, moreover the analysis in refs. [152, 153] was carried out using the limited DWBA framework. Having both (p,d) and (p,t) data measured with the (p,p) at 15 $A \cdot$ MeV, it is possible to investigate the coupling effects between the transfer and the elastic reactions.

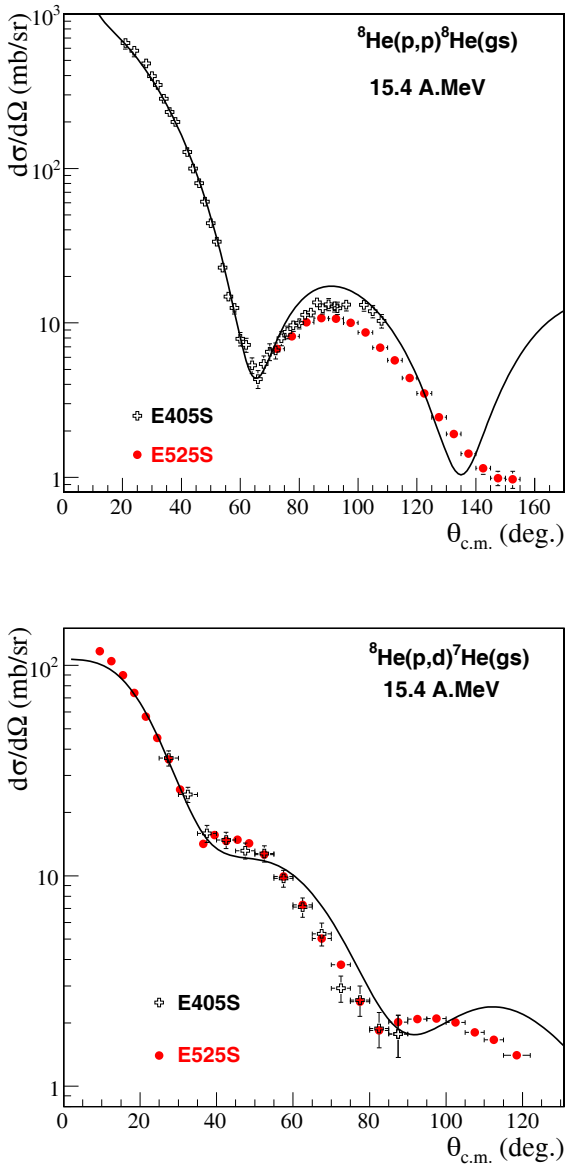

Fig. 22. Experimental cross sections for the ^{8}He(p, p) elastic [116] and ^{8}He(p, d) transfer [115] at 15.7 $A \cdot$ MeV to ^{7}He *gs*.

The microscopic densities for ^{8}He were tested by calculating the (p, p′) scattering in the CRC approach. The cross sections for ^{8}He + p at 15.7 $A \cdot$ MeV were calculated using the JLM potentials and various density sets: the *ab initio* NCSM [83], the *HF corr* and the *COSMA* ones. As shown in fig. 21, the elastic data are well reproduced by the calculations with the NCSM and the *HF corr* densities; the larger angles are not reproduced using the *COSMA* densities. At low energy, the order of magnitude for the cross sections at large angles ($> 50^\circ_{c.m.}$) is higher (around mb/sr) than it is for higher incident energies. This is combined to the good statistics of the incident beam. With small statistical error bars and the large *c.m.* extension of the elastic scattering data, we can observe the sensitivity of the cross sections to the shape of the densities at angles around $70^\circ_{c.m.}$ and it allows us to distinguish between the three cases, which was not possible at higher energies. This comparison shows that the ^{8}He is better modeled by a neutron-skin with $r_n - r_p \simeq 0.6$ fm rather than 1 fm. It means that the proton-neutron correlations needed to describe correctly the ^{8}He structure are different from the ones assumed in the *COSMA* model.

6.5 Effective potential of the ^{8}He(p, p) at 15.7 A · MeV

In principle, according to the Feshbach theory described in eq. (17), we can describe the effective potential for the elastic scattering as one term corresponding to the bare elastic scattering with no coupling to excitations and reactions, and one arising from the coupled reaction channels. The main effect which can be evaluated from the ^{8}He data set is the (p,d) coupling onto the (p,p). This effect is sizeable on our measurement of the observables: in fig. 22, we can see that the one-nucleon cross section has a large order of magnitude, (10–50) mb/sr, in the angular range between 10 to $50^\circ_{c.m.}$ similar to the elastic process. We can also observe a significant discrepancy of few 10 mb/sr between elastic data and the calculations done using the optical model approach and microscopic potentials for the entrance channel. This effect of the $p-d-p$ coupling was also studied in the case of the (p,p) elastic scattering of stable nuclei like ^{12}C or ^{24}Mg and discussed for the unstable ^{10}Be. The effective potential term arising from the p-d-p coupling can be extracted from the elastic cross sections using the S-matrix inversion, as explained in ref. [154].

This full effective potential of the entrance channel for ^{8}He + p was obtained by inverting the S-matrix (details were discussed in ref. [116]) obtained from the CRC calculations which take into account the (p,d) coupling onto the (p,p) elastic scattering. As a consequence, the potential can now be written as (we denote real potentials with V and W for imaginary ones):

$$U^{\text{eff}} = V^{JLM} + iW^{JLM} + V_{SO}^{JLM} + V^{crc} + iW^{crc} + V_{SO}^{crc}.$$

The JLM potential calculated for the ^{8}He + p reaction is shown in fig. 23. In fig. 24, the CRC calculations (solid line) reproduce the elastic scattering using the bare JLM potential; for comparison, the calculation done using the same bare potential but without coupling is shown with the dotted line. The difference between both is due to the coupled reaction (p,d) effect which produces the change of the real and imaginary parts of the entrance channel potential shown in fig. 25. In principle, the full effective potential which should be used to reproduce the elastic scattering corresponds to the sum of the VCP shown in fig. 25, with the bare potential: $\lambda_V V^{JLM} + i\lambda_W W^{JLM} + V_{SO}^{JLM}$ ($\lambda_V = 1.0$ and $\lambda_W = 0.2$). Without the coupling effects, if we keep the initial JLM potential (fig. 23) or even modify the real and imaginary parts (fig. 21, bottom side), the elastic data is not reproduced. Mainly, the effective potential generated within CRC produces: i) a change of

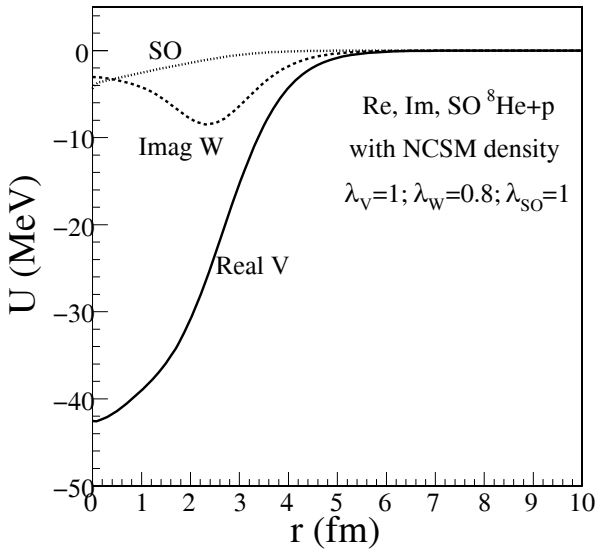

Fig. 23. The JLM microscopic potential (real, imaginary and spin-orbit parts) of ^{8}He on proton at 15.7 $A \cdot$ MeV. The calculations includes the NCSM densities (of $V_{3\text{eff}}$ type).

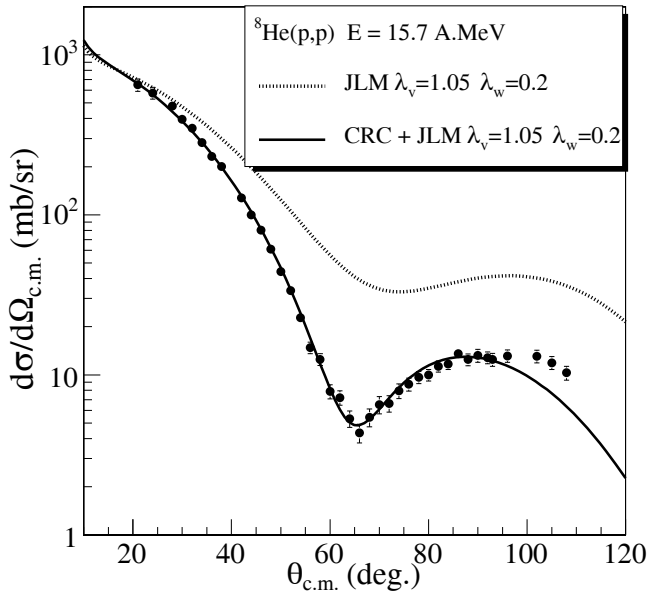

Fig. 24. Coupling effects of the (p,d) on the elastic scattering ^{8}He(p, p) at 15.7 $A \cdot$ MeV. The calculations and potentials are discussed in the text.

the real potential (adding VCP real term), ii) a change of the imaginary potential corresponding to a large fraction of the imaginary part usually calculated within the JLM framework. With the CRC coupling, we only need to keep $0.2W^{JLM}$ (fig. 24) and the remaining of the effective imaginary part is given through the (p,d) coupling.

In a further step, as will be explained in sect. 7, including also explicitly the (p,t) reaction with (p,p) and (p,d) in the coupled reaction scheme, we will see that all the data can be well reproduced [117].

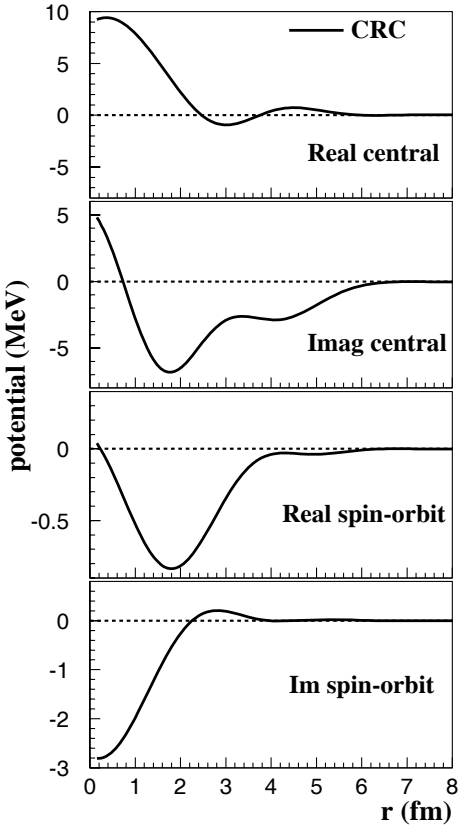

Fig. 25. Potential (VCP) obtained in ref. [116] created by the coupled reaction channel effects due to the one-neutron (p,d) transfer onto the elastic scattering ^{8}He(p, p) at 15.7 $A \cdot$ MeV.

Table 12. Parameters of the CH89 potential for the ^{8}He(p,p) scattering at 72 $A \cdot$ MeV. The real part was normalized by a factor $N_r = 0.8$ following the discussions given in the text. The radii are the reduced ones. The R_C value is fixed to 1.3 fm for ^{8}He.

U	$N_r * V_v$	r_v	W_v	W_S	r_w	r_{so}
	MeV	fm	MeV	MeV	fm	fm
^{8}He	30.66	1.137	7.042	5.349	1.120	0.74

6.6 Analysis of ^{8}He(p, p′) at 72 A · MeV

To discuss the extraction of the multipole moments and the test of the $B(E2)$ value using the (p, p′) data with the analysis of the proton elastic and inelastic scattering of ^{8}He, measured at RIKEN at 72 $A \cdot$ MeV [63], we will compare the results obtained using the two approaches discussed in sects. 4.2 and 4.3, the one with phenomenological deformed potentials and the model with microscopic density-dependent potentials.

In the first approach, the ^{8}He+p potential is calculated using the CH89 parameterization, with the prescription discussed in sect. 4.5 about the reduction of the real part of the potential. The parameters are given in table 12.

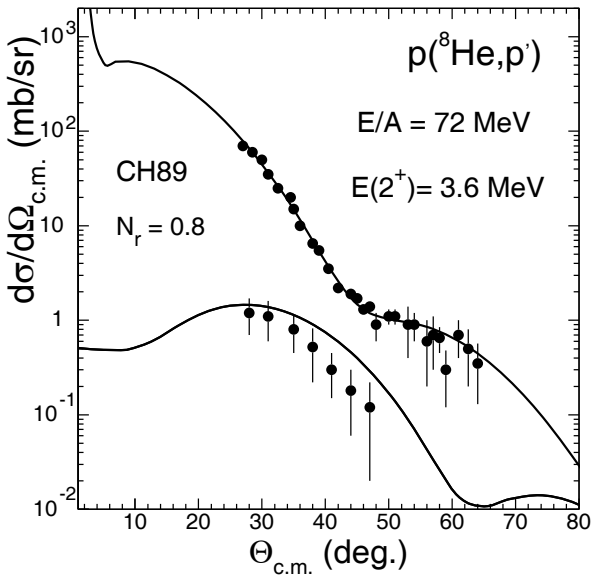

Fig. 26. Cross sections for the ^{8}He(p,p') at $72\,A\cdot$MeV, comparison of the data [63] to the calculations done with the deformed CH89 potential.

We present in fig. 26 the curves calculated with the ECIS coupled-channel analysis code [131] using the CH89 and the deformed potentials, assuming, as in ref. [63], that the deformation lengths for the nuclear and Coulomb potentials are equal. The extracted value is of the order of $b_c = 0.3$. With $r_0 = 1.3\,$fm, b_c corresponds to a $B(E2)$ value equal to $0.9\,e^2\cdot\mathrm{fm}^4$. In ref. [155], the predicted values for the unmeasured $B(E2)$ are given from the trend indicated by the "Global best fit" using the energies of the 2^+ states: from the 2^+_1 at 3590 keV, the $B(E2)$ value is indicated as: 7.2 (1.3) $e^2\cdot\mathrm{fm}^4$. However, this indication may be valuable in the case of discrete bound states for stable nuclei or close to the valley of stability; in the case of weakly bound nuclei having an unbound nuclear states and large matter radii, the value may be strongly overestimated.

For stable nuclei or close to the stability, the proton and neutron densities can be considered as homothetical and in the case of processes of small amplitudes, at energies between 10 to $100\,A\cdot$MeV, the inelastic reactions involving stable nuclei or close to the stability were successfully described with the deformed potentials, assuming equal deformation length for proton and neutrons and similarly for the nuclear and Coulomb parts, with $\delta = \delta_N = \delta_C$. But for nuclei with a large N/Z ratio, these assumptions are put under question, and *a priori* the values of the deformations of the nuclear and Coulomb potential parts should not be considered as equal, and as well the proton and neutron excitations cannot be taken as equal in the (p,p') studies. An independent extraction is needed, but, even in this case, in the next step, assumptions about the shape and nature of the excitations are needed to establish the relationships between the nuclear and Coulomb deformation lengths expressed with the b_n, b_p, in the case of the phenomenological deformed potential model.

Table 13. Moments and radii of the ^{8}He densities used for the (p,p') calculations with the definitions of the $M_{n,p}$ values indicated in the text and in eq. (7).

Density	M_p fm^2	M_n fm^2	M_n/M_p	$B(E2)$ $e^2\cdot\mathrm{fm}^4$
$4\hbar\omega V_{3\mathrm{eff}}$	0.501	6.67	13.3	0.251
Tassie	1.00	5.0	5.	1.
densvv	0.5	3.65	7.3	0.25

However, a microscopic density-dependent optical potential approach is required for a direct access to the amplitudes of the proton and neutron excitations via (p,p'): in the calculations, they can be expressed with several sets of the theoretical proton and neutron transition densities and these inputs can be tested by comparison to the (p,p') data, also the range of (M_p, M_n) values consistent with the (p,p') data can be extracted, and the relationship between the integrated M_n, M_p moments can be checked. It is important to note that the sensitivity of the (p,p') to the $B(E2)$ is weak because the (p,p') is dominated by the neutron excitation (there is a factor 3 between the interaction strengths of the neutrons and protons as shown in table 1); moreover, in ^{8}He, as seen in ^{6}He, the small separation energies of the neutrons combined to the neutron ratio favour the contribution of the neutron excitations. If now we consider the b_c value equal to 0.1 (corresponding to $B(E2) \simeq 0.1\,e^2\cdot\mathrm{fm}^4$) it is possible to describe also the (p,p') data, by taking different deformation strengths for nuclear and Coulomb parts, with the second curve. Since the $B(E2)$ to the 2^+_1 unbound state is not known experimentally, both the range of the M_p and M_n values associated to the proton and neutron transition densities should be searched, by comparing (p,p') data and calculations with various sets of transition densities, either given by theories or built to reproduce the data. The NCSM transition densities from 0^+ *gs* to 2^+, based on realistic NN and $3N$ interactions [70,71] are used below as a starting set for the (p,p') calculations. In fig. 27, the NCSM $V_{3\mathrm{eff}}$ p, n transition densities $\rho^{tr}_{p,n}$ are compared (second and third plots) to the density set noted "densvv" and to the Tassie-type densities, both built to reproduce the (p,p') data (fig. 28) with various $B(E2)$ values and M_n/M_p ratio. The parameters M_p, $B(E2)$ and M_n of these sets are displayed in table 13.

6.7 Sensitivity of the ^{8}He(p,p') to the $\mathrm{M_n}$ and $\mathrm{M_p}$ at 15.7 A · MeV

The (p,p') calculations were made at $15.7\,A\cdot$MeV using the two density sets *Tassie* and *densvv* of table 13; they are presented in fig. 29. As a test case to illustrate the weak sensitivity of the (p,p') process to the proton transition density and to the related $B(E2)$ transition strength value, the calculations were also done with various values for (M_p, M_n) moments, the curves are shown in fig. 30.

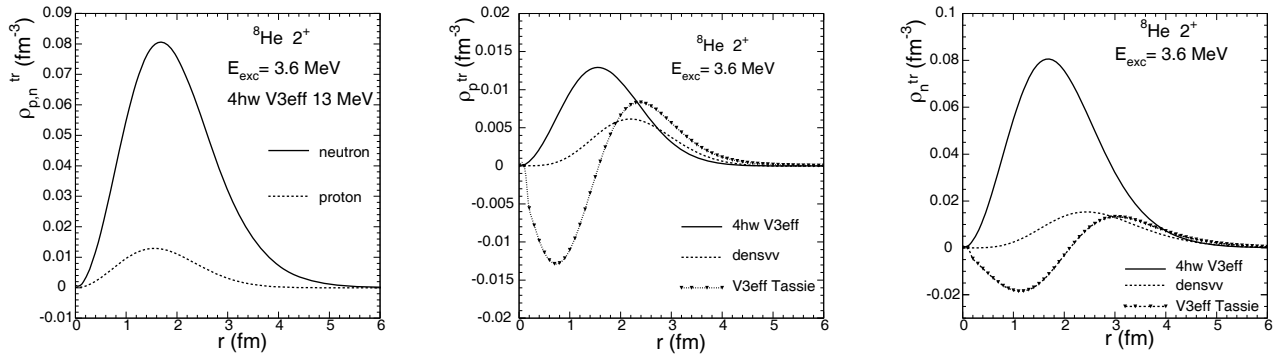

Fig. 27. Transition densities of ^{8}He used for the calculations of the inelastic proton scattering ^{8}He(p, p′) at 72 $A \cdot$ MeV. From left to right: the p, n transition densities $\rho_{p,n}^{tr}$ are calculated with the NCSM model including $V_{3\text{eff}}$ interaction; the second and third plots compare $\rho_{p,n}^{tr}$ densities for NCSM and phenomenological Tassie densities.

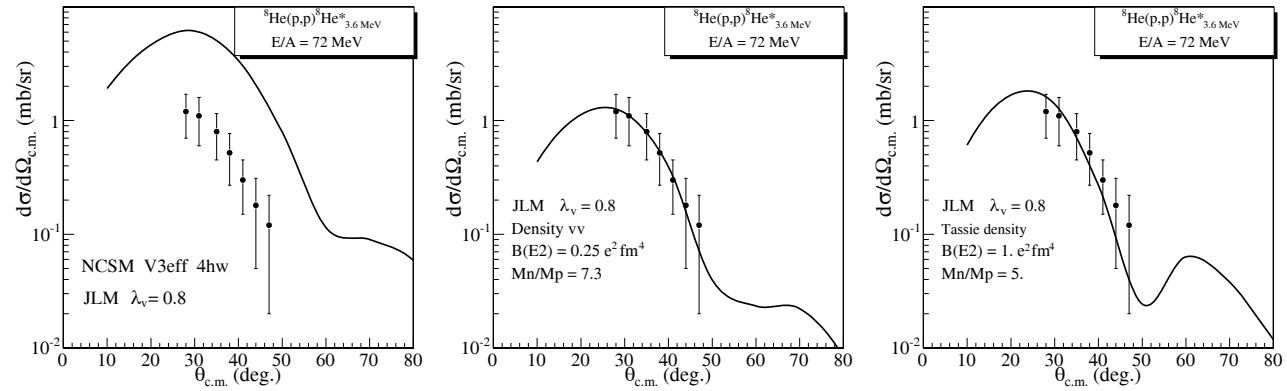

Fig. 28. Analysis of the inelastic scattering ^{8}He(p, p′) at 72 $A \cdot$ MeV.

Keeping the same M_n value (equal to 3.5) and varying the $B(E2)$ from 0.25 to 1 $e^2 \cdot$ fm^4 the corresponding curves (black full, thick dotted one) do not differ by more than 0.2 mb/sr. The variation of the (p, p′) cross sections are significantly large (nearly 20%) from red to thin dotted lines with the variation of the $(M_n)^2$ value of 20%. For the (p, p′) studies to unbound states, disentangling between the two cases are beyond the possibility of our present experimental technique from the point of view of both the statistical and the systematical error bars (due mainly to the background subtraction, and to the uncertainties related to the target thickness and energy straggling).

7 Discussion of the configurations obtained from the 1- and 2-n transfer reactions

7.1 Analysis of the (p,t) reactions using the ^{8}He beam

Initially, the wf of ^{8}He was built in the *COSMA* model as the simplified $\alpha + 4$n corresponding to a pure $(1p_{3/2})^4$ structure. From the analysis of the angular distributions for the ^{8}He(p,t)^{6}He reactions to the ^{6}He gs and 2^+ state at 15.4 $A \cdot$ MeV (E405S data shown by the crosses in fig. 31), it was shown that the ^{8}He gs also includes the $(1p_{3/2})^2$ $(1p_{1/2})^2$ neutron configuration [117]. Using the same configuration mixing, it was shown in ref. [117] that the (p,d) and (p,t) reactions available in the literature, measured at 50A [152] and at 63 $A \cdot$ MeV [153] (with an angular range from 5 to 30$^\circ_{c.m.}$ for the cross sections) could be also interpreted consistently and well reproduced within the CRC framework. The mixing between $(1p_{3/2})^2$ and $(1p_{1/2})^2$ states is consistent with the findings of the dineutron configurations obtained within various recent theory frameworks: AMD and HFB models. Within the AMD approach, the ground and excited states of ^{8}He were calculated [65] and it was shown that the mixing of the gs of ^{8}He has both the j-j (with $p_{3/2}$ closure) and the L-S (^{4}He + 2n + 2n) coupling features. By studying the motion of four neutrons around the ^{4}He core solved by superposing the wfs of AMD [65], the mixing of dineutron components in ^{8}He gs were also found. Within the HFB approach, using a α-core+4n model for ^{8}He and a density-dependent (DD) contact interaction between the valence neutrons, a strong dineutron correlation was also found in ref. [76], and the probabilities of the neutron configurations in the gs wave function are indicated to be: 34.9% of $(1p_{3/2})^4$ and 23.7% for $[(1p_{3/2})^2, (1p_{1/2})^2]$; other minor contributions are 10.7% for $[(p_{3/2})^2, (d_{5/2})^2]$ and 7.8% for $[(s_{1/2})^2, (p_{3/2})^2]$.

The calculations are also consistent with the extended data set results of E525S discussed in ref. [119] and presented in figs. 31 and 32. The (p,t) reactions were mea-

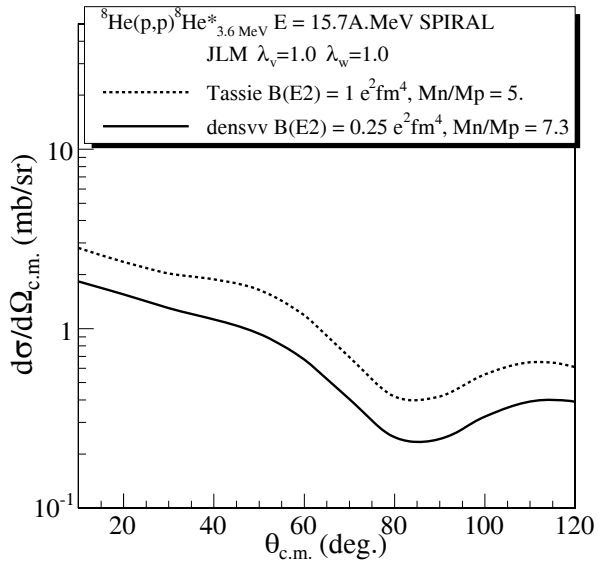

Fig. 29. Cross sections for ^{8}He(p, p′) at 15.7 $A \cdot$ MeV calculated using various sets of transition densities, with modified values of the moments M_p, M_n.

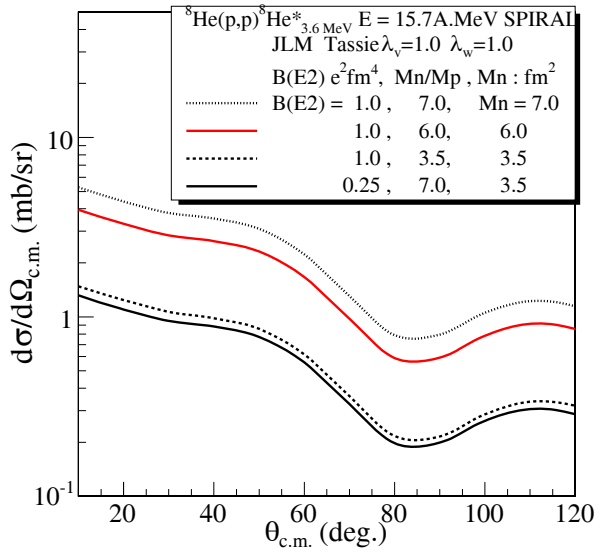

Fig. 30. The same as in the previous figure, to illustrate the sensitivity to $B(E2)$ and to M_n/M_p ratio.

sured to the new states, found above the known 2_1^+, at 2.6 and 5.3 MeV; (p,t) calculations were carried out for various angular transfer momenta and the ones corresponding to the best fit of the data are shown in fig. 32, corresponding to $L = 2$ and $L = 1$, respectively.

7.2 Spectroscopy of ^{6,8}He

The comparison of the (p, p′) results for the ^{6,8}He spectroscopy with the calculations is also useful to check the correlations proposed by the various models. As explained in sect. 4, the new spectroscopic data of ^{6,8}He were obtained using the missing mass method, from the direct reactions induced by the SPIRAL ^{8}He beam on proton target. The full analysis of the E_x spectra and the extraction of the ^{6}He resonances are explained in ref. [119]. The distribution of a resonance with the energy E_R and intrinsic width Γ_R can be defined as a Breit-Wigner parametrization:

$$f(E) = \frac{1}{\pi} \frac{\Gamma_R/2}{(E - E_R)^2 + (\Gamma_R/2)^2} \,. \tag{23}$$

In the analysis of the excitation energy spectra populated by the direct reactions, the distributions of the resonances are modelled as Breit-Wigner functions of width Γ folded with a Gaussian function, to take into account the spreading due to the experimental resolution, estimated of the order of 610 up to 720 keV (FWHM) for the (p,t) reaction. For ^{6}He, the resonant states were populated from the ^{8}He(p,t) reaction [119], above the known 2_1^+ state, obtained at 1.8(2) MeV, $\Gamma = 0.1 \pm 0.2$ MeV (consistent with the state at 1.8 MeV with $\Gamma = 113$ keV of the literature), two new resonances were observed: at $E^* = 2.6 \pm 0.3$ MeV, with an intrinsic width $\Gamma = 1.6 \pm 0.4$ MeV and at 5.3 ± 0.3 MeV with $\Gamma = 2 \pm 1$ MeV. corresponding, using the reaction analysis explained in sect. 7.1, to a 2^+ and to a $L = 1$ state, respectively. For ^{8}He, the E_x spectrum was obtained from the (p, p′) scattering induced by the ^{8}He beam and measured with the MUST array [118]. The first two resonant excited states of ^{8}He were obtained, the 2_1^+ found at 3.62 ± 0.14 MeV (width 0.3 ± 0.2 MeV), and the other one found at 5.4 ± 0.5 MeV (width 0.5 ± 0.3 MeV) [118]. In figs. 33 and 34, the spectroscopy for the He isotopes is presented, with the characteristics of the excited states below 10 MeV. The figures include our results and the data of the literature, in comparison with the calculations of the nuclear structure theories already discussed, and to the most recent ones. The values for the S_n energies correspond to the recent evaluations (AME2012), given in table 2; for ^{6}He it is 1.71 MeV[4]. For ^{6}He, the previous data were obtained from multi-nucleon transfer reactions in refs. [156–160]. The excitation energies were computed in ref. [21] within the GFMC framework, using the $2N$ (AV18) and $3N$ (IL2) interactions with parameters fitted to provide accurately the binding energies of ^{6,8}He. But this model cannot provide a description of the resonance parameters. The spectroscopy of ^{6}He was calculated in the NCSM framework with several versions of the nuclear interactions and size of the basis space adopted for p-shell nuclei [69,148] and also using CD Bonn NN-potential (2000) [84] or new TNI interactions [70,84]. However, the binding energy in this model is underestimated (as was shown in table 3). In fig. 33, the NCSM $V_{3\text{eff}}$ refers to the NCSM results obtained with the NN AV8' and the TNI TM99 interactions (in $6\hbar\omega$ space, $\hbar\omega = 14$ MeV), given in ref. [70], providing an improved E_b value, at 28.19 MeV. In all these calculations, the NCSM standard framework can provide the spectroscopy for discrete states, but not for resonant states.

[4] In the article [119] presenting the ^{6}He spectroscopic results, the plot was shown with the AME2003 value $S_n = 1.86$ MeV.

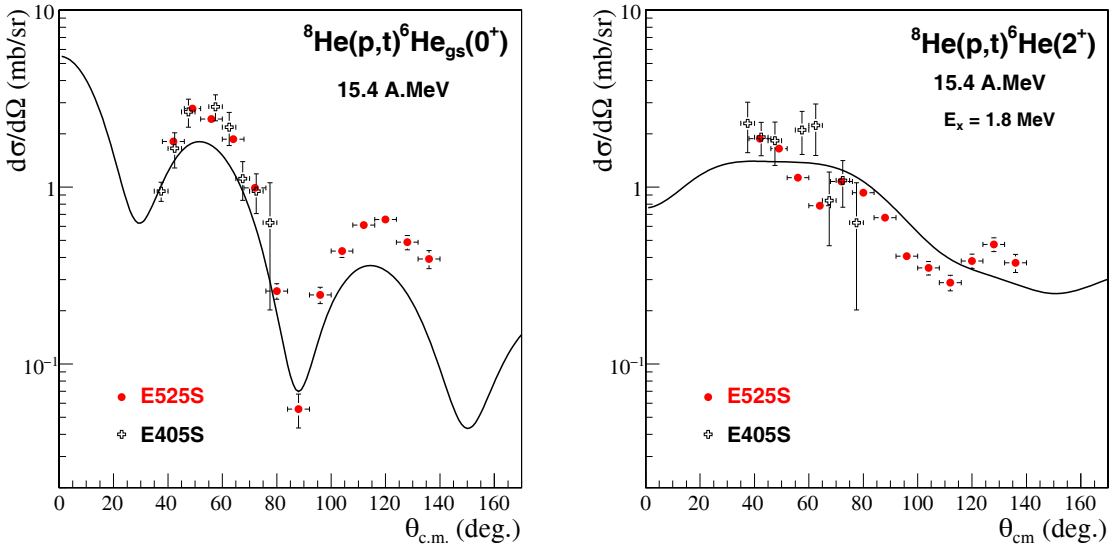

Fig. 31. Experimental cross sections for the ^{8}He(p,t) transfer at 15.4 $A \cdot$ MeV (E525S) [119] to ^{6}He *gs* and 2^+_1 state at 1.8 MeV, compared to the previous data set obtained at 15.7 $A \cdot$ MeV (E405S) [117] and to the reaction calculations explained in the text.

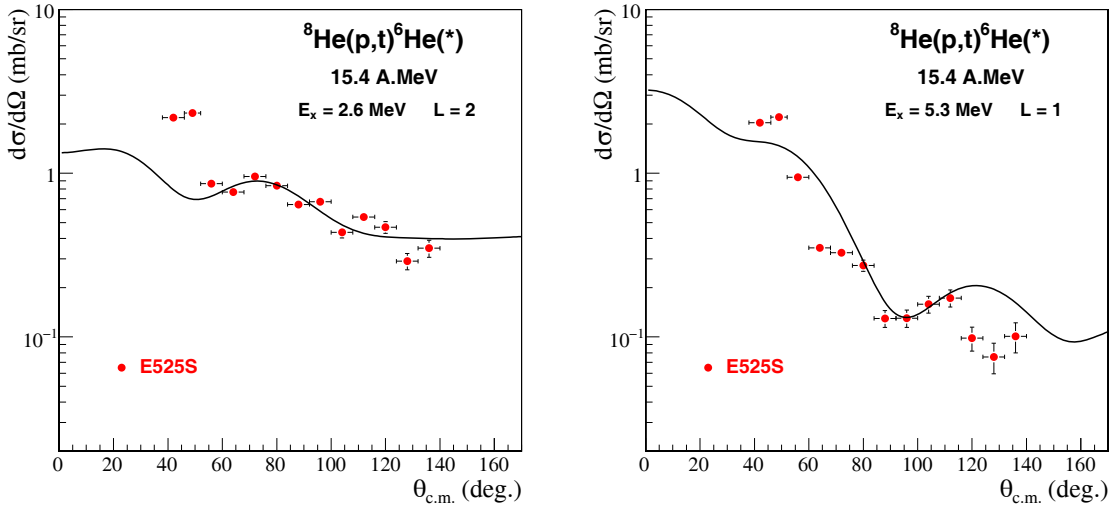

Fig. 32. Experimental cross sections for the ^{8}He(p,t) transfer at 15.4 $A \cdot$ MeV [119] to the new resonant states of ^{6}He: a 2^+ at 2.6 MeV, and a $L = 1$ state, possibly 1^+, at 5.3 MeV.

In fig. 34, the SPIRAL-MUST (p, p') results [118] are presented with the RIKEN ones at 72 $A \cdot$ MeV [63], and the measurements using invariant mass method: the value we found for the 2^+_1 state is consistent with the previous (p, p') data, and with the multi-nucleon transfer data obtained at HMI, in 1995 and 1999, respectively [161, 162], or with break-up [163] reactions obtained at GSI (1995). It is found in contrast with the other GSI data given in ref. [164] (2001).

The resonances predicted by various *ab initio* theories, like the QMC calculations [21] or the NCSM [70, 83], overestimate our results for ^{6,8}He. The crucial role of the continuum correlations and of the coupling of the bound and the scattering states, missing in most of these approaches, might explain why these theories fail in reproducing the unbound states. The low-lying spectroscopy is modified by these couplings. In the models treating them explicitly, like the GSM [25, 26], through the consistent description of the bound states and of the particle continuum, the *gs* of ^{6,8}He are found bound by the *CC* correlations, and the position of their 2^+_1 state is well predicted. To discuss the resonant excited states of ^{6,8}He, we examine the calculations given by the models which include the treatment of the resonant states: the GSM framework [25, 27, 87] and recent GSM with effective interactions for ^{6}He [86], the COSM [88, 90] and TOSM [91] models, and the *NCSMc* model including the *CC* treatment with RGM [92]. In the CSM [85], which includes also the particle continuum effects, the predictions for the first two resonant states are consistent with our data for ^{8}He, but not for ^{6}He.

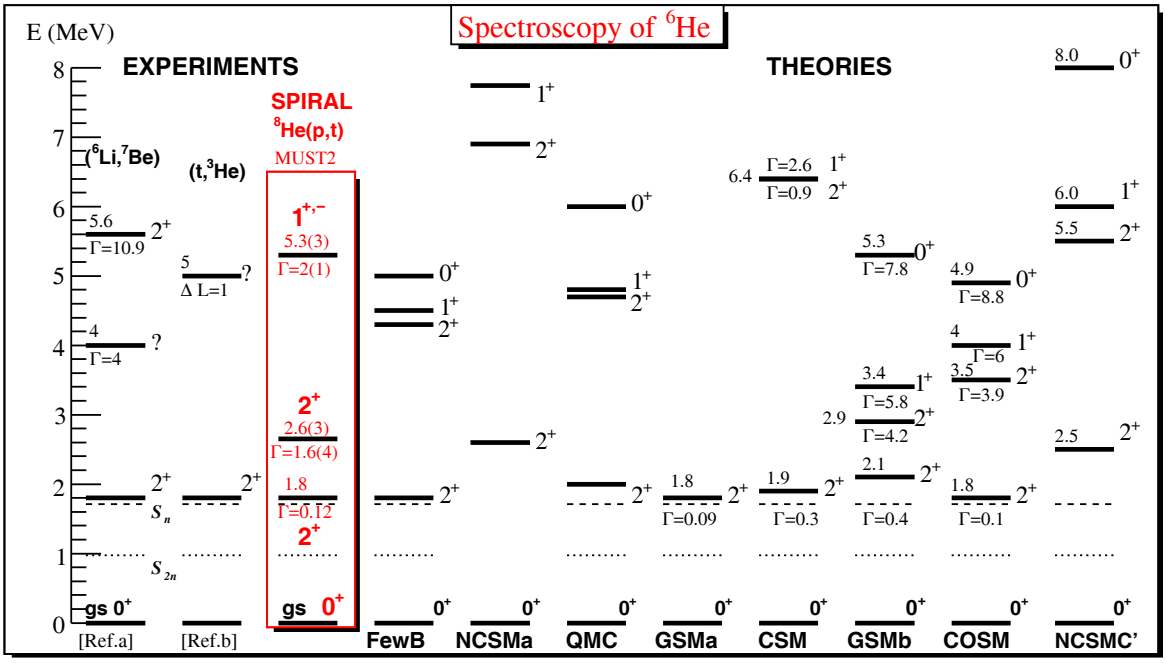

Fig. 33. Spectroscopy for ^{6}He below 10 MeV: comparison between the experimental results and the calculations from the microscopic models discussed in the text: the few-body model "FewB" [42], the QMC GFMC [21], the NCSM in ref. [70] noted NCSMa; the GSM, noted GSMa for ref. [27], GSMb for [86]; the CSM [85]; the COSM [88,89] and the NCSM including *CC* effects, "NCSMC" [92]. The ^{8}He(p,t) results [119] shown in the red frame were obtained with MUST2 at GANIL. The other data are from multi-nucleon transfer reactions [Refa] (in refs. [156,157]) and [Refb] (for [158–160]).

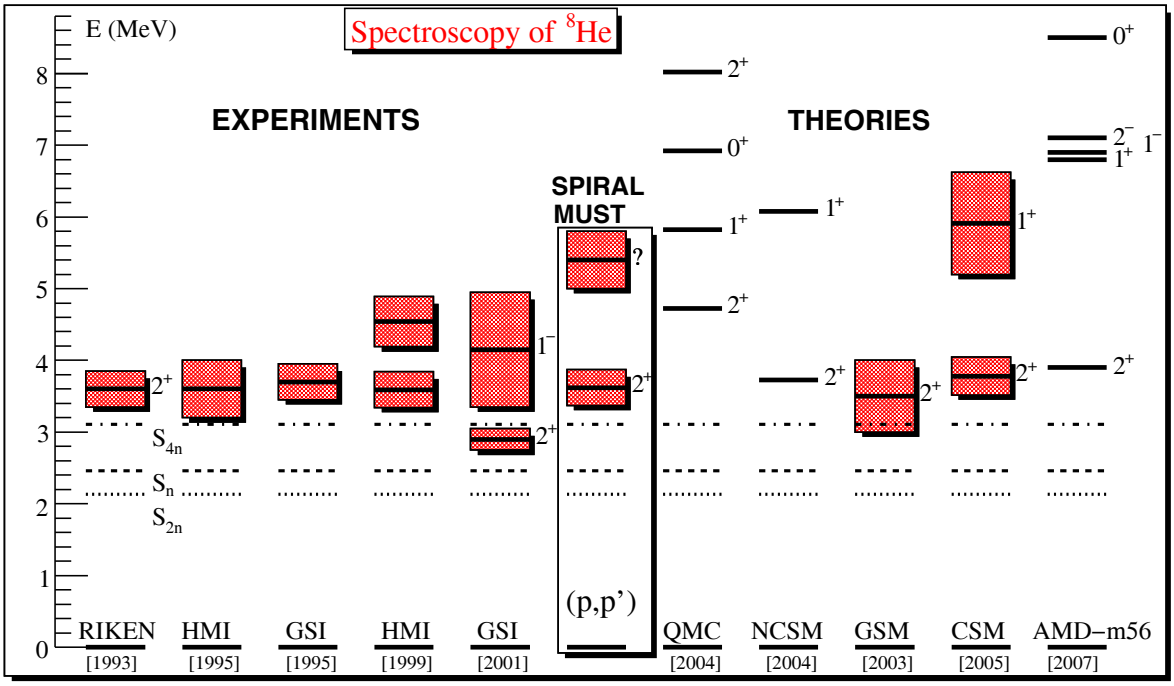

Fig. 34. Same as in fig. 33 for ^{8}He: (p, p′) data are from ^{8}He at 15.7 $A\cdot$MeV (SPIRAL) [118] and at 72 $A\cdot$MeV (RIKEN) [63]. The other references are explained in the text. The calculations of QMC are from ref. [21], NCSM [83], GSM [26], CSM [85] and AMD [65].

Several calculations were done for ^{6}He within the *NCSMc* model. One was developed to investigate the ^{7}He resonant states in ref. [92], adopting the procedure of the similarity-renormalization-group (SRG) evolved chiral next-to-next-to-next-to-leading order (N^{3}LO) NN potential; in this case, with the SRG parameter $\Lambda = 2.02\,\mathrm{fm}^{-1}$, realistic binding energies were obtained for ^{4}He (28.0 MeV) and ^{6}He (28.6 MeV), using the NCSM basis size of $12\hbar\Omega$ ($\hbar\Omega = 16$ MeV). However, as shown in fig. 33, the calculated states are found at larger energies compared to our experiment and to the results obtained within GSM technics. The sensitivity of the results to the parameters can be discussed: another NCSM+RGM calculations were done for ^{6}He, also within the SRG-N^{3}LO NN framework, but using $\Lambda = 1.5\,\mathrm{fm}^{-1}$ [165] and $13\hbar\Omega$ space ($\hbar\Omega = 14$ MeV); in this case the excited states were found at lower energies than the previous calculations, but ^{6}He was underbound, with S_{2n} found at 0.43 MeV. Both effective interactions and CC coupling, as in ref. [86] for the GSM, are needed to reach a qualitative agreement with the ^{6}He spectroscopy. On the other hand, the AMD-m56 calculations [65] provides a satisfactory understanding of the spectroscopy for both excited states in ^{8}He, this improvment may be attributed to the accurate treatment of the neutron correlations and excitations. The characteristics of the resonant states and the level spacing both for ^{6,8}He are very sensitive to the nucleon correlations used in the various frameworks, and progress is expected in the theories to include on the same footing the realistic interactions and the CC effects, without any core assumption and with good properties of diffusivity for the basis functions (for instance, WS functions instead of the Harmonic Oscillator ones used in the NCSM).

8 Conclusions, summary and perspectives

The results for the rms radii and moments obtained from the (p, p′) data can be now be compared with the structure calculations done within several microscopic models. We would like to discuss and confront the descriptions given by the approaches with *ab initio* type interactions, by the models which assume a core or by microscopic models which do not limit *a priori* the degree of freedom and the many-body correlations of the nucleons forming the nucleus, or by the frameworks with CC treatment.

8.1 Conclusions on the densities and on the correlations

8.1.1 Rms radii

Through the comparison between the models, and the results from the ^{6,8}He direct reactions, and using the r_p radii available in the literature, we have obtained the range of rms radii presented in table 14. In figs. 35–37, we present an overview of the rms radii for ^{4,6,8}He, with the values obtained experimentally and calculated within various frameworks. The plot for the rms radii of ^{4}He is included, because it is meaningful to check to which extent the same models, with various assumptions for the interactions and correlations, may describe consistently and accurately not only the rms radii for the weakly bound ^{6,8}He isotopes but also the strongly bound and compact ^{4}He nucleus. For the ^{4}He, the r_m value can be extracted (see the red square in fig. 35) using the r_p radius (experimentally well determined via the (e, e) probe, see last value r_{pp} extracted from 2008 evaluation of r_{ch}) and it is useful to note that the r_m value from the σ_I cross sections is overestimated, and unconsistent also with the calculations.

Table 14. Summary of the rms radii for ^{6,8}He extracted from the (p, p′) analysis presented in this article. The error bars reflects the sensitivity of the (p,p) data to the tested densities.

A	r_m	r_p	r_n	Δr	$\Delta r/r_m$
A	fm	fm	fm	fm	
^{6}He	2.51 (5)	2.00 (5)	2.72 (7)	0.72 (8)	0.29 (12)
^{8}He	2.50 (5)	1.95 (5)	2.67 (7)	0.72 (8)	0.29 (12)

For ^{6,8}He, in the rectangle frame of the figures, we give the values obtained from the (p, p′) analysis presented in this article, using as constraints: i) the experimental separation energies; ii) the proton rms radii deduced from the laser spectroscopy measurements (left part of the plots), and iii) the matter rms radii tested on the (p,p) elastic data. We have selected the models providing values close to the experiment ones and, from the (p, p′) analysis, we have tested several sets of nuclear density distributions given by the model calculations; finally we have deduced the r_m and r_n radii values shown in the red frame of figs. 36 and 37. The rms radii of the models discussed in this article are shown in the right part of the plots; large ranges of r_n values (see tables 6–11) can be seen, strongly dependent on the NN correlations and interactions used in the various theoretical frameworks. In conclusion of this work, we can now discriminate between the various models, and provide the rms radii values consistent with the observables of ^{6,8}He.

As can be seen in fig. 36, for ^{6}He, the r_m and r_n are underestimated by most of the models. Amongst the several densities generated by the FB models the $fc6$ density is closer to the data because it was selected as the one with the S_{2n} value closer to experiment. Within the FB-reaction model of refs. [96,97], the reanalysis of the reaction observables —σ_I and the proton scattering of ^{6,8}He at large ($700\,A \cdot$ MeV) incident energy— gives r_m radii values in agreement with the radii found in the (p, p′) analysis.

For ^{6,8}He, we have obtained $\Delta R > 0.5$, corresponding to the criteria of the halo or neutron-skin. The observables of the r_m radius and of the weak S_{4n} energy for ^{8}He were found consistent with the neutron-skin structure assumed for this nucleus within the few-body [36] and the 5-body *COSMA* model [43]. But other observables and analysis show that this picture is limited and does not correspond to the neutron extension in the ^{8}He nucleus.

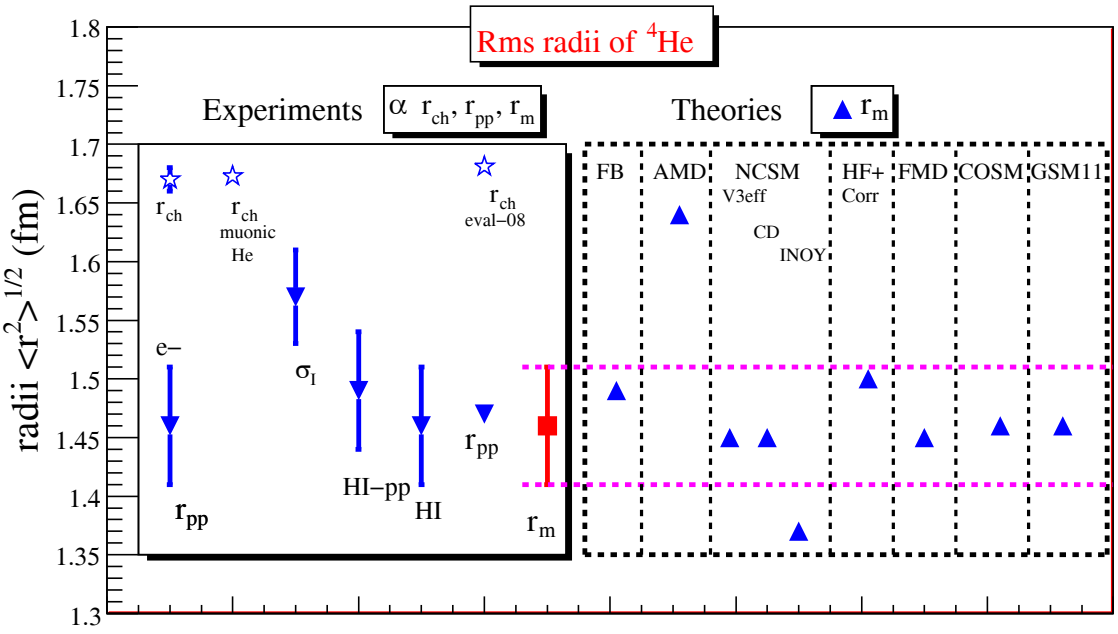

Fig. 35. Values of the rms radii obtained for ^{4}He from electron scattering, muonic He experiments, interaction cross sections and (p,p) data. The matter rms values of the microscopic models discussed in the text are given in the frame to the right. The charge, proton and matter radii are given with the star and triangle (down, up) symbols, respectively. The experimental values for the r_m matter radii and for the charge (and r_p) are given in tables 5 and 7. The r_m values and references for the model calculations are given in table 6; AMD is for AMD-m56 [65]; NCSM $V_{3\text{eff}}$, CD and INOY correspond to the calculations done for the p-shell nuclei using several interactions: effective 3-body one in ref. [70], CD Bonn 2000 and $3NF$ described in ref. [84], respectively; *HF corr* from ref. [72], FMD given in ref. [67], COSM is explained in [90], and GSM in [87]. The dashed magenta lines correspond to the range of the experimental r_m values consistent with the updated evaluation of data sets using the EM probe [44], to be compared to the theoretical ones.

From the analysis of the ^{8}He(p, p) and (p,t) within the CRC framework, we have obtained that the (p,p) data could be described using the ^{8}He *gs* densities predicted by the NCSM model, with neutron-skin features different from those proposed by the *COSMA* model. It means that the ^{8}He *gs* has a larger r_p radius and a smaller neutron-skin thickness than assumed in the $\alpha + 4$n model. This is consistent with the ^{8}He *gs* investigated via the (p,t) reactions, showing that the *gs* includes not only the $(1p_{3/2})^4$ but also the $(1p_{3/2})^2\ (1p_{1/2})^2$ neutron configuration [117]. Moreover, the elastic data are reproduced by the calculations performed with the ^{8}He + p JLM potential including the *gs* densities given by the NCSM model [70, 71]. It is not the case with the *COSMA* densities. We found *gs* densities having similar characteristics (in terms of rms radii) as the ones calculated within the HF model [72] and presented in sect. 6. Both the r_n radii discussed in our analysis and the mixing $(p_{3/2})\ (p_{1/2})$ in the ^{8}He *gs* are strong constraints to validate or not the nuclear models; from the overview of the microscopic calculations, it is interesting to note that the models providing consistent values and configurations for ^{8}He are the ones describing quantitatively the dineutron correlations as in the HFB combined to 5-body model [76] or with the configuration mixing in AMD [66]. Nevertheless, the value of the rms matter radius calculated in ref. [76], 3.23 fm, is not compatible with the experimental one; it is also inconsistent with all the other theoretical values. The reason why such an unrealistic r_m radius is obtained may be explained [166] by scrutinizing the various shell model configurations found in the HFB *gs* wave function for ^{8}He in ref. [76]; the probability of these configurations were given in sect. 7.1. The HFB model is built with the constraint on the value of the core +4n threshold close to the experimental value ($E = -3.112$ MeV) and, as discussed before, it provides the dominant configurations for ^{8}He *gs* in agreement with the ones found via the ^{8}He(p,t) analysis. But the spurious extension of the rms value may be attributed to the contribution of one of the shell model configuration, with the *s* orbital: $[(s_{1/2})^2, (p_{3/2})^2]$, even if it corresponds to a smaller probability (7.8%). It means that the experimental results, both the r_m value and the configurations found in the ^{8}He(p,t) analysis, represent a sensitive probe for the shell model configurations in the *gs* and can be used as constraints to check the validity of the calculations for the main contributions in the wave function[5].

[5] Calculations are on-going in the HFB framework to change the initial interaction parameters so as to reduce the spurious configuration, and to recalculate the ^{8}He r_m radius [166].

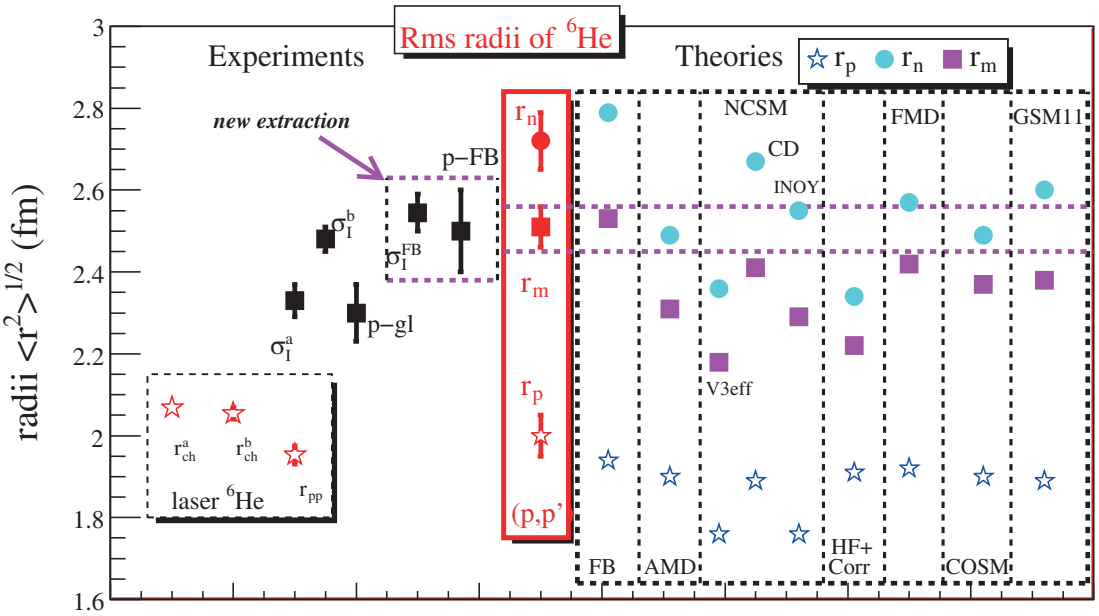

Fig. 36. Values of the rms radii obtained for ^{6}He from interaction cross sections and (p,p) data, and comparison to the values of the microscopic models discussed in the text. The charge (or p), n, matter radii are given with the star, circles and square symbols, respectively. The matter rms radii values are noted σ_I^a for ref. [48], σ_I^b [93], p-gl [94]. The FB (Few-Body) notations are used for the $fc6$ density set calculated within the 3-Body model of ref. [36] and also for the experimental values, σ_I^{FB} [96] and p-FB [97], to recall that the rms radii were extracted from the reanalysis of the reaction observables, within the FB framework, as was explained sect. 3.2, with the values given in table 5. The reaction model used the same 3-body wave function [36]. The AMD notation is for AMD-m56 [65]; NCSM $V_{3\text{eff}}$ corresponds to the calculations from ref. [70], CD to the ones done with the CD Bonn 2000 and $INOY$ with $3NF$ [84]. For the other models, the notations and the references are the same as in fig. 35. The experimental values and references are given in tables 5 (r_m) and 7 (r_{ch} and r_p) and the model calculations for ^{6}He are presented in table 6.

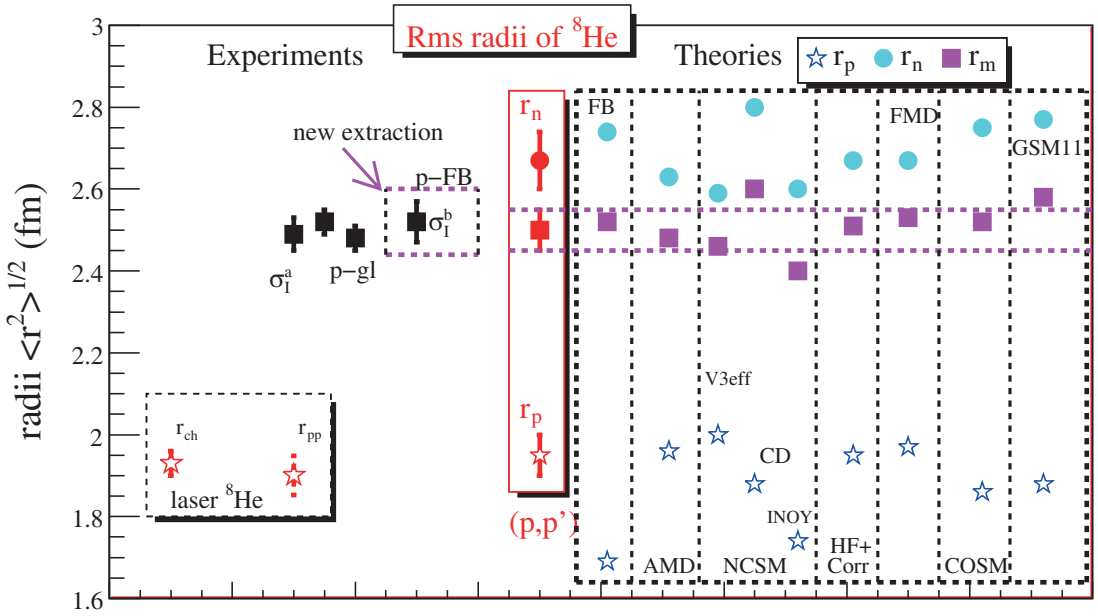

Fig. 37. The same as in fig. 36 for ^{8}He. The rms values and the references of the model calculations for ^{8}He are given in table 11.

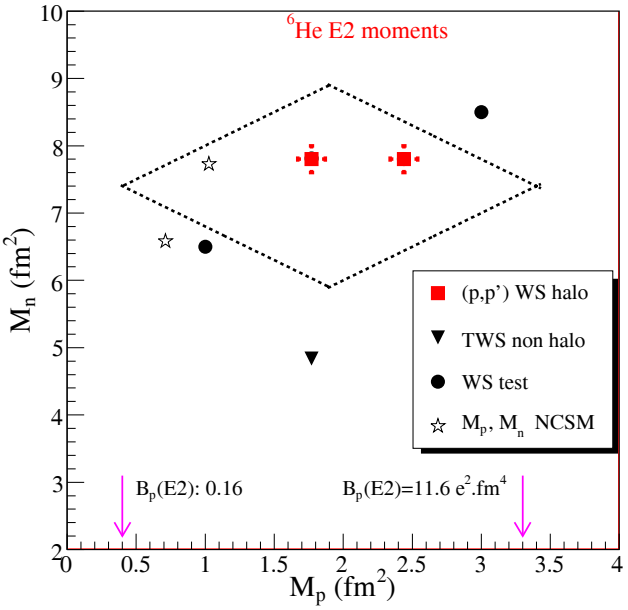

Fig. 38. The values are discussed in the text, and given in table 15. Test calculations (full circles) were made with a fixed value of the M_p moment taken equal to 1 or 3. The horizontal (vertical) arrows indicate the domain of extreme possible values for the M_n (M_p) moments. The values consistent with the (p, p′) data should be considered inside the losange, indicating the sets of possible (M_p, M_n) correlations.

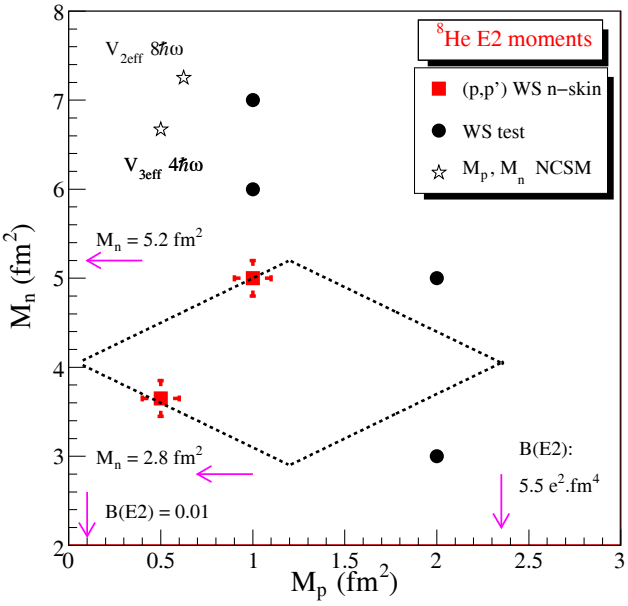

Fig. 39. The same as in fig. 38 for ^{8}He. The NCSM refers to the values obtained with the $V_{3\text{eff}}$ interaction. Full circles are tests calculations done for fixed values (M_p, M_n) corresponding to (1,6), (1,7) or (2,3) (2,5) fm^2.

But there is also a valuable comparison to be made, between the sets of r_m radii given by the theories and the experimental data: in the case of the AMD-m56 calculations, the r_m radius for ^{4}He is overestimated (1.64 fm) and $r_m(^6\text{He})$ is smaller (2.31) while $r_m(^8\text{He})$ value is in agreement (2.48). However, another calculation (v58) within AMD framework found $r_m(^4\text{He}) = 1.46$ fm but undestimate the radii (given at 2.23 and 2.24 fm) for ^{6,8}He. Similarly, in the case of the NCSM calculations done with the INOY interaction [84] including $3NF$, the binding energies are close to experiment, but the NN correlations are not under control, since the rms radii are underestimated for the ^{4,6,8}He isotopes. This is an indication about the need for a better understanding on the attractive/repulsive effects on the NN and NNN correlations: the ones playing a role in the size expansion of the ^{6,8}He nuclei also change strongly the α particle radius.

8.1.2 Multipole moments

As presented in sect. 2.2, we are sensitive to the $M_{n,p}$ multipole moments, and for the (p, p′) process, $b_n/b_p = 3$. From the (p, p′) microscopic analysis, for the 0^+ to 2_1^+ excitations, We have obtained several sets of the $M_{n,p}$ values for ^{6,8}He. To discuss the range and the correlations between the (M_p, M_n) values validated by the (p, p′), a summary of the results is presented in figs. 38 and 39 (absolute values are given). The losange frame corresponds to a domain of values for $(|M_p|+|M_n|)$ and $(|M_n|-|M_p|)$; inside the losange, the data are correlated at the 1σ level; outside, the values are excluded. The stars correspond to the densities given by the NCSM model for ^{6,8}He, and the full circles correspond to the test calculations, using Tassie densities, made with fixed values for (M_p, M_n) to check the domain of validity of the moments by comparison to the (p, p′) data.

The range of values obtained for the moments of ^{6,8}He are given in table 15. The meaningful values correspond to the combined pair (M_p, M_n), validated by the tests on the (p, p′) data, using Tassie densities; they have to be found in the smaller range indicated by the losange frame plotted in the figures; the corresponding M_n/M_p values are also given in table 15.

The neutron excitation calculated by the NCSM was not validated by the (p, p′) data. From the analysis done at 72 $A \cdot$ MeV and the study of the sensitivity of the (p, p′) to the M_n and M_p values we have shown that it was needed to modify the shape of the transition densities to reproduce the data, and that "diffuse" transition densities (peaked at larger radii than given by the NCSM) were more appropriate. In our phenomenological analysis we adopted the derivative of a 2pF function (Tassie-model) and the M_n value was adjusted to reproduce the (p, p′) distributions. However it is worthful to underline that the shape we found for the ^{6,8}He transition densities, is similar to one indicated within the GSM approach [25], diffuse and peaked around 2.5 fm.

If we now consider both the detailed spectroscopy and the rms radii for ^{6,8}He, few models give a satisfactory agreement with the whole data set. Initially, the ones having no *a priori* on the wf and including many-body degree of freedom had a limited description of the spectroscopy,

Table 15. Multipole moments for ^{6,8}He validated by the (p, p′) studies done at several incident energies following the relationships given in eq. (7).

A	M_p	$B(E2)$	M_n/M_p	M_n
A	$e \cdot \mathrm{fm}^2$	$e^2 \cdot \mathrm{fm}^4$		$e \cdot \mathrm{fm}^2$
^{6}He	1.9 ± 1.5	0.16–11.6	4.2 ± 1.2	7.4 ± 1.5
^{8}He	0.1–2.35	0.01–5.5	5.5 ± 2.1	4.0 ± 1.2

since they did not treat explictly the resonances of the unbound states. We have underlined the important effects that have to be included consistently in the theories, to reach a complete and accurate understanding of the weakly bound gs and of the unbound resonant states:

- excitation of all nucleons —all possible many-body degrees of freedom— as done within NCSM or HFB;
- Hamiltonians with realistic $2N$ and $3N$ interactions;
- CC effects as in CSM, GSM or COSM models.

However, up to now, most of the frameworks including the CC treatment assume a core, having the same quantum numbers of the α particle. This core is considered as inert (fixed size, no excitation). This assumption limits the calculations to the possible degrees of freedom of the valence neutrons with respect to the core and cannot provide quantitative results of the energy of the states and of the resonance width, since the many-body correlations are missing. New approaches were developed to include the particle-hole excitations of ^{4}He in the Coupled-Cluster theory [167] and the important role played by the $3p$-$1h$ excitations of ^{4}He in the accurate calculations of the gs and 2^+_1 of ^{6}He was underlined in this model. However, the most promising approach, to make a general microscopic treatment of the many-body wf, would be to establish a framework able to consider the interactions of all nucleons in the nuclear field, using $2N$ and $3N$ forces and including CC effects, without any assumption of a core. These last years, as discussed before, there were several attempts within the theoretical frameworks to improve the microscopic description of the light nuclei by including the TNI and extending them with the treatment of the coupling effects, most of them with a core assumption, for instance, the GSM including effective $3N$ interactions [86]. Another promising approach is the new NCSM with continuum, *NCSMc* model [92], which was applied to ^{6}He and expected to improve the description of the unbound states compared to the previous NCSM models. The ^{8}He data presented here would be also a good test case for this model, since we found that the (p, p′) calculations with the NCSM transition densities ovestimated the data. Both aspects, structure (rms radii, configurations) and spectroscopy of ^{6,8}He (extended up to 10 MeV) are important to check the validity of the new models. The objectives should be also to reach a consistent understanding of the r_p, r_n, r_m radii for all ^{4,6,8}He within all the new frameworks, like GSM [87] and *NCSMc* models.

8.1.3 Pairing correlations

The pairing correlations in ^{6,8}He are non observables; they depend upon the (assumed) reduction of the many-body wave function problem in terms of possible sub-systems, like core and dineutron(s) clusters. In general, they can be investigated theoretically by interpreting the calculations of the two-particle density $\rho_{2N}(r_1, r_2, \theta_{12})$, defined with the radial coordinates of two nucleons r_i $i = 1, 2$ and with θ_{12}, the opening angle between the radial vectors taken between the c.m. position and the two nucleons. These distributions can be compared to experiments which measure the fragments associated to the same few-body components. The definitions can be found in ref. [74], with $S = 0$ (the spin-singlet state of the 2N) and $S = 1$ (spin-triplet) components considered in the LS-coupling scheme. This model follows the guidelines established in the work done on the ^{11}Li pairing correlations [168], where a 3-body was assumed with a structureless core with the interaction adjusted to fit the S_{1n}. Most of the few-body models discussing the ^{6,8}He pairing correlations fit the separation energies. For instance, in refs. [74, 76], HFB calculations are performed using 3- and 5-body models (α core + i neutrons) for ^{6,8}He, respectively; the Density-Dependent δ interaction parameters are adjusted to reproduce the known properties of the gs, like the $S_{2\mathrm{n}}$ energies. With these assumptions of the cluster structure, the characteristics of the halo and neutron-skin for ^{6,8}He are discussed in terms of the dineutron and core-nn correlations of the wf, studied by looking at the 3-dimensional plots of the density distribution $\rho(r, \theta_{12})$ with $r_1 = r$, $r_2 = r$. It can be simplified into the model-dependent $\rho(r_{c-nn}, \theta_{12})$, function of the relative coordinate of the subsystems, (c for the core and n for the valence neutrons, r_i $i = 1, 2$) with $r = r_{c-nn}$, the distance between one of the neutron and the c core, and θ_{12} the opening angle between the radial vectors taken between the core and the two neutrons. It is the probability of finding the particles at a distance $r = r_{c-nn}$ from the core, with an angle θ.

It can be defined for ^{6}He (or with the transposed definition for the 2-dineutron in the case of ^{8}He) as

$$\rho(r, \theta) = \langle \Psi_{gs} | \delta(r_1 - r)\delta(r_2 - r)\delta(\theta_{12} - \theta) | \Psi_{gs} \rangle. \quad (24)$$

The distribution probabilities of the following quantities can be deduced (the definitions can be found in ref. [74]):

- distance between valence neutrons R_{nn} with $R^2_{nn} = \langle r^2_{nn} \rangle = \langle \Psi | (r_1 - r_2)^2 | \Psi \rangle$;
- the distance $R_{c-2\mathrm{n}}$ between an assumed core nucleus ($N = 2, Z = 2$) and the c.m. of two valence neutrons for ^{6}He (or two dineutrons in ^{8}He) the rms radius, $R_{c-2\mathrm{n}}$ with $R^2_{c-2\mathrm{n}} = \langle \Psi | (r_1 + r_2)^2/4 | \Psi \rangle$;
- the angular density $\rho_{nn}(\theta_{12})$ expressed as $4\pi \int r_1^2 \mathrm{d}r_1 \int r_2^2 \mathrm{d}r_2 \rho_{2N}(r_1, r_2, \theta_{12})$.

The correlation functions and their expectation values are sensitive to the microscopic inputs of the models; they are also correlated to the rms radii. Intrinsically, if the pairing effect is correctly taken into account, even if the $S_{2\mathrm{n}}$ is low, the extension of the wf should be limited due

Table 16. For different models of the gs wf of ^{6}He, discussed in the text, the calculated observables: S_{2n}, rms radii and the corresponding model-dependent values of the rms radii R_{nn} and $R_{c-(nn)}$ (fm) and of the angle θ_{nn} between neutrons.

Model	ref.	R_{nn} fm	$R_{c-(nn)}$ fm	θ_{nn} deg.
3-body HFB	[74]	4.62	3.63	66.3
3-body CSsM	[169]	4.70	3.49	67.9
GSM11	[87]	–	2.96	67.9
3-body HFB	[170]	3.75 (93)	3.88 (32)	$51.6^{+11.2}_{-12.4}$

to the "pairing anti-halo" effect explained in ref. [101]. It means that, for a given theory, not only the calculations of the binding energies or S_{2n} values have to be compared to the data, but also the rms radii values, to check the treatment of the pairing correlations. In general, once the characteristics of the r_p, r_n, r_m radii and configurations of the wfs are strongly constrained, the other geometrical parameters like the core-dineutron radii and angles, should be determined in a limited range of values. As a consequence, our experimental results for ^{6,8}He would correspond to a well defined sets of values for the angular correlations of core-neutrons, that may be inferred by comparison with the microscopic models in agreement with our data. Specific decompositions of the wavefunctions of ^{6,8}He were discussed within the AMD framework [66], the CScM (Complex Scaling Method) [169], the Few-Body technique HFB-FB [74,76] or GSM [87]. All these models found that the 2n in ^{6}He are strongly correlated, with a large R_{c-nn} and the main n configuration being $(p3/2)^2$ ($S = 0$ at $\simeq 90\%$); for ^{8}He, the 2n are less correlated, the $S = 0$ is also the dominant configuration ($\simeq 80\%$); it was underlined in ref. [74] that the HFB calculations indicate a mixing consistent with the results from the (p,t) transfer reactions, as discussed in sect. 7.1. In table 16 presenting the calculations of the R_{c-2n} and angle between neutrons, we have selected the models matching the criteria of the gs configurations and providing results close to the experimental results for the gs properties: the separation energies (fixed in HFB-FB or computed in the GSM), the rms radii (r_p found in agreement with experiments in GSM; the CScm gives consistent value for r_p, and for $r_m = 2.46$ fm [169]), the configurations of the gs. The Coulomb break-up technique has been widely used to discuss the 2n correlations in the halo nuclei and to infer the values of the R_{c-2n}, R_{nn} radii and θ_{nn} angles, as discussed in refs. [74,170]. Recently, the extraction of the 2n correlations from the 3-body Coulomb break-up reaction of ^{6}He was investigated theoretically in ref. [169], with the three-body scattering states calculated using the Cscm combined to the Lippmann-Schwinger equation. The interpretation of the Coulomb break-up results appears as ambiguous: in the 2D energy distributions and in the invariant mass spectra for the $E1$ transition, it remains difficult to disantangle the part related to the strength due to 2n correlations from the contributions due to another processes like the ^{5}He resonances in the FSI (final state interaction). The FSI processes act as a screening, preventing from a direct access to the 2n configurations —as far as the break-up processes are concerned. The last line of table 16 gives the values deduced from the experimental rms matter radii in ref. [170], using a 3-body model described as in ref. [74]. They are consistent with the results of the models already validated via the comparison to our experimental results on the rms r_m, r_n radii and on the n configurations. The mean value of the angle, $\langle\theta_{nn}\rangle$ was discussed in the various frameworks. However, its significance has to be questioned. If we consider the angular densities found in the GSM [87] and HFB [74], two maxima appear, around 30 and 138 deg, corresponding to the 2 main components: the dineutron (large R_{c-nn}, small R_{nn}) and the cigar-like (smaller R_{c-nn}, larger R_{nn}) configurations, which can be seen also clearly as two peaks in the 3D plots of the 2-body density. For ^{8}He, a similar behaviour is found for the position of the peaks [87]. When the angular densities present few-body components and at least two mean peaks —as is the case for halo or neutron-skin nuclei— the notion of the mean angle is not meaningful both experimentally (it is not an observable) and theoretically.

From this discussion, we can propose a straightforward method to have access to the correlations in the weakly bound nuclei and to check the theories: the direct process is to measure the rms matter radii via the (p,p) scattering and to obtain the neutron configurations from (p,d) and (p,t) transfer reactions; from these results, by comparison to nuclear models assuming a 3-body decomposition the c-nn, nn radii and θ_{nn} model-dependent quantities can be given.

8.2 Extracting nuclear structure information from elastic data

The authors of ref. [171] have studied the near-barrier elastic scattering data for light exotic nuclei (^{11}Li, ^{6}He, ^{11}Be) on heavy targets (Pb). These data are in contrast with the scattering scheme observed for stable systems. To reproduce the elastic scattering distributions, strong coupled effects were taken into account; they are shown to be due to different processes (depending on the projectile+target systems) like excitation or nucleon transfer or both [171], which can be included explicitly in the reaction framework. The $B(E2)$ value for the weakly bound nuclei like ^{6,8}He cannot be obtained via direct Coulomb excitation measurements using gamma-spectroscopy since the 2^+_1 is unbound. As discussed in ref. [171] (and references therein), several calculations were developed to calculate the strong coupling effects on the elastic data, using the main channel induced by the Coulomb coupling, expressed in terms of one structure parameter: the $B(E2)$ value. It has to be underlined that these calculations were performed in very few specific cases: stable nuclei, symmetric ones (^{16}O) or with small N/Z ratio (^{18}O), with bound 2^+ state, for which there is mainly the inelastic channel to take into account (no coupling to the 1n-transfer is needed). Quantitative results can be obtained with a good reproduction of the data, but these calculations rely

on several approximations, which have no theoretical justification. In particular, several of them can be questioned in the case of neutron-rich weakly bound nuclei, like ^{6,8}He, for which neutron and proton densities may develop different shapes, and behave differently with respect to the interaction with a light (proton) or heavy-Z target (like Pb). We would like to discuss and question the following ones:

- The transition potentials are calculated assuming similar deformation lengths for nuclear and Coulomb potentials, and as if the proton and neutron parts of the transition densities were similar (isoscalar approximation) [28]; this is not demonstrated *a priori*.
- The calculations done for elastic data on heavy target neglect the inelastic channels due to the excited states other than the 2^+, but several of these states are located below 10 MeV and may play a role in the inelastic couplings.
- The coupling to the continuum may be taken into account via the CDCC calculations, but this requires model-dependent parameters for the CC inputs and for the transition strengths to scattering states.
- The Q-reaction values of the 1n and 2n transfer channels are large and this is an indication of the strong coupling effects induced on the elastic channel, as was seen in the case of the ^{8}He + p data. How to describe the interplay between inelastic with transfer channels, and transfer to the continuum states? This is still under debate.

In the case of the light neutron-rich nuclei like ^{6}He, the calculations of the elastic process should take into account, to interpret the data, the main processes playing a role in the strong coupling effects: i) the possible ^{6}He excitations, like the main one from the 0^+ to 2^+ state; this requires the calculations of the transition amplitudes from a model. The assumed transition densities would correspond to a set of $M_{n,p}$ values (with M_p related to the $B(E2)$ value); ii) the spectroscopic amplitudes for the 1n- and 2n-transfer channels.

If we focus on these reactions, in a CRC mode, it means that we would need to develop a structure-reaction model assuming the interplay between these effects. Microscopically, we should consider neutron and proton transition densities from various structure models; they have not necessarily the same shape. The strong coupling effects may be related also to the neutron excitation part, and, depending on the interaction strength —related to the target and incident energy— we may expect different behaviour of the neutron and proton potential deformations. Due to the ambiguities related to the choice of the model-dependent transition potentials and of the spectroscopic amplitudes, the access to one specific quantity like the $B(E2)$ value appears to be not meaningful, since i) the excitation is dominated by the neutron excitation not only for the proton target but also for heavy-Z target; ii) in the case of strong coupling effects, the elastic distributions are sensitive, through the *VCP*, to a combination of virtual potentials; iii) the interplay between the possible excitation modes and transfer channels results in the correlations between nuclear parameters.

The path to improve our knowledge and to extract nuclear structure information for the exotic nucleus of interest —like ^{6,8}He— is to discuss the domain of validity of the relevant quantity, $M = |M_n + M_p|$ established on a consistent analysis of several data sets, combining: elastic data on proton and heavy-Z targets, 1-n and 2-n-transfer channels for these targets. The spectroscopy of excited states up to ~ 10 MeV has also to be considered in this scheme, to have an insight on the main inelastic channels possibly contributing to the VCP. In our analysis we have produced the range of (M_p, M_n) values which were tested using the (p, p$'$) data. The same kind of analysis should be performed for the elastic data on the heavy targets, with no *a priori* on the proton and neutron excitations, using microscopic transition potentials for the calculations of the inelastic channel coupled to the elastic one; also the transfer channels should be incorporated. With this method, the range of the allowed (M_p, M_n) values validated by the data can be also discussed and compared to our findings from the (p, p$'$).

8.3 Perspectives: New degrees of freedom, new probes

Transfer reactions with polarized targets should be used also to complete the spectroscopic information: by measuring the ($\boldsymbol{p}$, d) and ($\boldsymbol{d}$, p) angular distributions, the spin and parity of the new states found in the previous studies of exotic nuclei could be assessed. For instance, the ^{8}He($\boldsymbol{p}$, d) and ^{6}He($\boldsymbol{d}$, p) would be mandatory to conclude about the experimental spectroscopy found for ^{7}He [115].

We need also to obtain extended information about the nuclear gs and transition densities, not only integrated values, like rms radii and multipole moments, but the variation of the form factors as a function of the radial coordinate or of the transfer momentum. We have shown that the (p, p$'$) analysis combined with the experimental values of the rms charge radii has provided an insight on the matter and on the neutron rms radii with a sensitivity of ± 0.1 fm. We have observed that the ^{6,8}He(p, p$'$) cross sections are weakly sensitive to the M_p value. Another probe is needed to complete the picture on the proton excitation in the case of the 2^+ unbound states. In the long-term future, we could think about measuring the form factors from the (e, e') scattering to the 2^+_1 state of ^{6,8}He. We can imagine to carry out electron-nucleus collisions and to make (e, e') scattering measurements using radioactive beams with the new machines developed or foreseen:

- at RIKEN a new facility, SCRIT (*Self-Confining Radioactive Isotope Target*) [172], has been designed to make beam of electrons (accelerated in a ring) scatters off a "target" of radioactive ions stored in a trap; successful tests were made for Cs isotopes. At present the facility is limited to the long-lived ions ($T_{1/2} > 1$ ms) but further developments are expected to extend the measurements for isotopes with shorter lifetimes;
- at GSI, a storage ring electron-nucleus collider is foreseen within the ELISe project for *ELectron-Ion Scattering experiments* [173]; it will be developed along with the future facility FAIR.

This will provide benchmark data for the *ab initio* effective theories and for the many-body treatment of the correlations In the next years, the possibility to investigate the structure of hyper-exotic nuclei may also open new perspectives on the nuclear interaction. Exotic hypernuclei offer a new degree of freedom —strangeness— to constrain the nuclear structure theories [174]. A hypernucleus is a nucleus which contains at least one strange baryon (hyperon Y) in addition to the nucleons. The glue role of the Y (like Λ) in the nuclei gives an easier access, experimentally, to the neutron-rich regions of hypernuclei compared to the world of ordinary (non-strange) exotic nuclei: the $N\Lambda$ interaction is more attractive and the hypernucleus may be more stable against the neutron decay. Light nuclei are laboratories for the studies of nuclear interactions: exotic ones for $2N$ and $3N$; hyperexotic, like ${}^{7}_{\Lambda}$He, for the YN interactions. The $3/2^+$ and $5/2^+$ resonant states of the neutron-rich hypernucleus ${}^{7}_{\Lambda}$He are at present calculated within the framework of the $\alpha + \Lambda + n + n$ 4-body cluster model [175], using ^{6}He as the core nucleus on which the ${}^{7}_{\Lambda}$He structure is built. Experiments in this field are already operated at various international laboratories (for instance, investigations of the states of ${}^{7}_{\Lambda}$He are on-going at JLAB) or planned[6].

8.4 Perspectives on the structure and reaction frameworks

The aim of the analysis was to explain the structure and the excitations of the ^{6,8}He isotopes in order to better understand the nuclear correlations between core and neutrons, and more generally between nucleons in a very diffuse neutron-rich nuclear matter. The $(\mathrm{p}, \mathrm{p}')$ analysis were performed with the JLM potential, taking into account explicitly the coupling effects induced by the weak binding of the unstable nuclei on the interaction potential. The $(\mathrm{p}, \mathrm{p}')$ calculations were compared to the data, and various sets of gs and transition densities were tested to extract the rms radii and the ranges of multipole moments. These fundamental quantities, with the spectroscopy below 10 MeV, represent benchmarks to discriminate between the various scenarios for the core-neutron configurations and nuclear correlations in ^{6,8}He, proposed by the structure models. To understand the phenomena and to explain the specific properties observed for the structure and the reactions of these nuclei, the key parameter is the binding energy. The weak binding energies explain the reason why the wf are extended, leading to the observation of large rms matter radii. We have examined the theories matching the binding energy criteria (*i.e.* providing realistic calculations of the E_b for ^{4,6,8}He) and checked their ability to reproduce both the gs properties, the rms radii and the low-lying excited states. The results on the spectroscopy of the ^{8}He drip-line nucleus were obtained by $(\mathrm{p}, \mathrm{p}')$ and transfer reactions on proton. They were compared to previous separate measurements, and found consistent with the predictions made by the recent nuclear models including the continuum-coupling effects to the resonant and scattering states. But, as underlined by Henri Poincaré (1854–1912), *Science is facts; just as houses are made of stones, so is science made of facts; but a pile of stones is not a house and a collection of facts is not necessarily science*. Our goals are not to collect data on the structure and spectroscopy and to confront them one by one to various theories producing accurately one specific observable. Our objectives are to reach a better understanding and modelling of the exotic nuclei, and we need to examine how the models could be improved to produce a comprehensive view of structure and reaction observables. We have also checked the consistency between the various reaction data sets, comparing them to the reaction calculations carried out at different incident beam energies, using the same structure inputs. Through the comparison between experiment and theory, we have underlined the importance of the renewal of various theory concepts to be able to explain the whole set of observables for light nuclei, —spectroscopy, rms radii. To that respect, these nuclei can actually be seen as a complete laboratory to test the new models developed in the *ab initio* framework with realistic nuclear forces. Today, the appropriate microscopic models appear to be the ones combining the contributions from the $3NF$ and the CC many-body correlations. In the future, making again a systematic comparison between the nuclear observables and the calculations for the light nuclei, we should be able to check the microscopic inputs and the validity of the assumptions made on the nuclear interactions including $2NF$ and $3NF$ contributions from the chiral EFT [177]; we could also expect to reach a deeper understanding of the modelling of these forces. This comparison will also offer new possibility to test the impact of the realistic forces with N^3LO $3N$ or $4N$, for which no calculation exists at present beyond the few-body systems (^{4}He) or the nuclear matter [177].

The microscopic frameworks developed to calculate the nuclear properties were initially built on phenomenological interactions. With the recent evolutions in the theory field, the chiral EFT interactions [178] can be implemented in the structure calculations and the comparison to the experimental observables is expected to give a direct insight on the nuclear forces. Using chiral interactions rather than phenomenological ones represents a fundamental advance in the field, since through these calculations a direct link to the first principles is possible in terms of the QCD theory. it should be also possible to reach a more direct understanding on the many-body correlations. As discussed completely in ref. [178], through this approach it is possible to reach a more direct understanding on the many-body correlations; the advantages will be quantitative, for the treatment of the many-body interacting nuclear system, with better controlled errors, and well defined power-counting for two- and higher-body forces.

Up to now, the halo states were treated using effective interactions, and the $3NF$ effects were also treated in a phenomenological way. The advances are now possible in

[6] Under operation at MAMI, JLAB, USA; FINUDA at DAΦNE; J-PARC, Japan; projects: SPHERE at JINR, Russia; PANDA; hypernuclei with Heavy Ion Beams (HypHI) at the GSI-FAIR [176].

the *ab initio* framework using the chiral Effective Field Theory (EFT) interactions. The goals are to reproduce, accurately, the nuclear binding energies as well as the nuclear radii and to reach a complete description of the halo states from first principles, using the $2NF$ and $3NF$ from the chiral EFT. The comparison to the *gs* observables of ^{6,8}He isotopes would provide insight on the $3NF$ chiral interactions [179,180]. Calculations and theory development are on-going towards this objective. Recently, the *gs* energies of the ^{4,6,8}He were calculated using renormalization group evolved chiral interactions in ref. [179] combined to the HH method for ^{6}He and the CC one for ^{8}He. The r_p and r_m radii for ^{6}He were also obtained [180], with the correct asymptotic behavior of the wf and the extended r_m radius, as expected for the halo structure.

The evolution of the reaction models towards a structure-reaction framework is also needed; it should include both the nuclear structure description and the calculations of the nuclear amplitudes; the objective would be to reach a comprehensive description of the whole sets of observables, and to determine the microscopic parameters and effects which play a crucial role for an accurate spectroscopy. With this reaction model at hand, we would calculate the excitation spectra populated at the incident energy of a given experiment, and we could then produce the cross sections for the transfer reactions to the nuclear states described by the structure model inputs. There are paths for such developments with, on the one hand, the recent calculations of the ^{40}Ca (p,p) and (p,d) reactions within the coupled-cluster theory [181] using interactions from chiral EFT, and, on the other hand, the works done on the non-local dispersive optical potential to describe properties above and below the Fermi energy [182].

This treatment is crucial for the reaction observables of the exotic nuclei, since their weak binding energies result in small threshold energies (for instance S_n, S_{2n} energies less than 2–3 MeV) and their continuum states are lying closer to the *gs* than in the case of their stable well-bound isotope. As a consequence, during the reaction processes, the probability for the transfer to continuum states is increased compared to other direct reactions to bound states, like elastic scattering or transfer to discrete states. Within a complete reaction-structure framework, the coupling to the scattering states could also be treated consistently with the coupling to other main channels and possible excitation processes; they would be included in the coupling reaction scheme, to carry out the calculations of the (p,p) (p,d) (p,t) reactions with the (p, p') treated on the same footing.

We thank H. Sagawa, I. Thompson and P. Navrátil for giving us the tabulated files of the nuclear densities discussed in the text, from the HFB, 3-body, NCSM models respectively. The works on the coupled reaction channel studies were performed within the framework of several projects of the ESNT, *Espace de Structure et de réactions Nucléaires Théorique* (`http://esnt.cea.fr`), this support is gratefully acknowledged. We would like to thank the referees for giving us important insight and useful comments on several discussions of this review.

References

1. H. Yukawa, Proc. Phys. Math. Soc. Jpn. **17**, 48 (1935).
2. I. Tanihata *et al.*, Phys. Lett. B **160**, 380 (1985).
3. P.G. Hansen, B. Jonson, Europhys. Lett. **4**, 409 (1987).
4. I. Tanihata *et al.*, Phys. Rev. Lett. **55**, 2676 (1985).
5. I. Tanihata *et al.*, Prog. Part. Nucl. Phys. **35**, 505 (1995).
6. B. Jonson, Phys. Rep. **389**, 1 (2004).
7. M. Mayer, J.H.D. Jensen, *Elementary Theory of Nuclear Shell Structure* (Wiley, New York, 1955).
8. T. Otsuka *et al.*, Phys. Rev. Lett. **87**, 082502 (2001).
9. T. Otsuka *et al.*, Phys. Rev. Lett. **95**, 232502 (2005).
10. K. Ikeda, N. Tagikawa, H. Horiuchi, Prog. Theor. Phys. Suppl. Jpn., Extra Number, 464 (1968).
11. W. von Oertzen, M. Freer, Y. Kanada En'yo, Phys. Rep. **432**, 43 (2006).
12. W. von Oertzen, Z. Phys. A **357**, 355 (1997).
13. W. von Oertzen, Phys. Scr. T **88**, 83 (2000).
14. K. Ikeda, H. Horiuchi, S. Saito, Prog. Theor. Phys. Supplement **68**, 1 (1980).
15. J. Fujita, H. Miyazawa, Prog. Theor. Phys. **17**, 360 (1957).
16. T. Otsuka *et al.*, Phys. Rev. Lett. **105**, 032501 (2010).
17. G. Hagen, M. Hjorth-Jensen, G.R. Jansen, R. Machleidt, T. Papenbrock, Phys. Rev. Lett. **108**, 242501 (2012).
18. J.D. Holt, J. Menendez, A. Schwenk, Eur. Phys. J. A **49**, 39 (2013).
19. S.C. Pieper, V.R. Pandharipande, R.B. Wiringa, J. Carlson, Phys. Rev. C **64**, 014001 (2001).
20. R.B. Wiringa, S.C. Pieper, Phys. Rev. Lett. **89**, 182501 (2002).
21. S.C. Pieper, R.B. Wiringa, J. Carlson, Phys. Rev. C **70**, 054325 (2004).
22. V. Somà, A. Cipollone, C. Barbieri, P. Navrátil, T. Duguet, Phys. Rev. C **89**, 061301 (2014).
23. P. Navrátil, V.G. Gueorguiev, J.P. Vary, W.E. Ormand, A. Nogga, Phys. Rev. Lett. **99**, 042501 (2007).
24. J. Dobaczewski, N. Michel, W. Nazarewicz, M. Ploszajczak, J. Rotureau, Prog. Part. Nucl. Phys. **59**, 432 (2007).
25. N. Michel, W. Nazarewicz, M. Ploszajczak, K. Bennaceur, Phys. Rev. Lett. **89**, 042502 (2002).
26. N. Michel, W. Nazarewicz, M. Ploszajczak, J. Okolowicz, Phys. Rev. C **67**, 054311 (2003).
27. N. Michel, W. Nazarewicz, M. Ploszajczak, Phys. Rev. C **82**, 044315 (2010).
28. G.R. Satchler, *Direct Nuclear Reactions* (Clarendon Press, Oxford University Press, 1983).
29. D.R. Tilley, C.M. Cheves, J.L. Godwin, G.M. Hale, H.M. Hofmann, J.H. Kelley, C.G. Sheu, H.R. Weller, Nucl. Phys. A **708**, 3 (2002).
30. G. Audi, A.H. Wapstra, C. Thibault, Nucl. Phys. A **729**, 337 (2003).
31. G. Audi, M. Wang, A.H. Wapstra, F.G. Kondev, M. MacCormick, X. Xu, B. Pfeiffer, Chin. Phys. C **36**, 1287 (2012).
32. G. Audi, F.G. Kondev, M. Wang, B. Pfeiffer, X. Sun, J. Blachot, M. MacCormick, Chin. Phys. C **36**, 1157 (2012).
33. D.R. Tilley, J.H. Kelley, J.L. Godwin, D.J. Millener, J. Purcell, C.G. Sheu, H.R. Weller, Nucl. Phys. A **745**, 155 (2004).
34. R.J. Glauber, *Lectures in Theoretical Physics*, Vol. **I** (Interscience, New York, 1959).

35. I. Tanihata *et al.*, Phys. Lett. B **206**, 592 (1988).
36. J.S. Al-Khalili, J. Tostevin, I. Thompson, Phys. Rev. C **54**, 1843 (1996).
37. M.V. Zhukov, B.V. Danilin, D.V. Fedorov, J.M. Bang, I.J. Thompson, J.S. Vaagen, Phys. Rep. **231**, 151 (1993).
38. S.N. Ershov *et al.*, Phys. Rev. C **56**, 1483 (1997).
39. P.G. Hansen, A.S. Jensen, B. Jonson, Annu. Rev. Nucl. Part. Sci. **45**, 591 (1995).
40. A.S. Jensen, K. Riisager, Phys. Lett. B **480**, 39 (2000).
41. A. Krasznahorkay, N. Paar, D. Vretenar, M.N. Harakeh, Phys. Scr. T **154**, 014018 (2013).
42. B.V. Danilin *et al.*, Phys. Rev. C **55**, 577 (1997).
43. M.V. Zhukov, A.A. Korsheninnikov, M.H. Smelberg, Phys. Rev. C **50**, R1 (1994).
44. I. Sick, Phys. Lett. B **116**, 212 (1982).
45. H. De Vries, C.W. De Jager, C. De Vries, At. Data Nucl. Data Tables **36**, 495 (1987).
46. M. El-Azab Farid, G.R. Satchler, Nucl. Phys. A **438**, 525 (1985).
47. G.R. Satchler, W.G. Love, Phys. Rep. **55**, 183 (1979).
48. I. Tanihata, D. Hirata, T. Kobayashi, S. Shimoura, K. Sugimoto, H. Toki, Phys. Lett. B **289**, 261 (1992).
49. Y. Ogawa, K. Yabana, T. Suzuki, Nucl. Phys. A **543**, 722 (1992).
50. Y. Suzuki, T. Kido, Y. Ogawa, K. Yabana, D. Baye, Nucl. Phys. A **567**, 957 (1994).
51. W. Mittig, Nucl. Phys. A **553**, 473c (1993).
52. A. Bohr, B.R. Mottelson, *Nuclear Structure*, Vol. **1** (Benjamin, 1969).
53. A.M. Bernstein, V.R. Brown, V.A. Madsen, Phys. Rev. Lett. **42**, 425 (1979).
54. A.M. Bernstein, V.R. Brown, V.A. Madsen, Phys. Lett. B **103**, 255 (1981).
55. R.C. Barrett, D.F. Jackson, *Nuclear Sizes and Structure* (Clarendon Press, Oxford, 1977).
56. The Particle Data Group (W.M. Yao *et al.*), J. Phys. G **33**, 1 (2006).
57. The Particle Data Group (K. Nakamura *et al.*), J. Phys. G **37**, 075021 (2010).
58. P.E. Hodgson, *Nuclear Reactions and Nuclear Structure* (Clarendon Press, Oxford, 1971).
59. J.J. Kelly *et al.*, Phys. Lett. B **169**, 157 (1986).
60. L.B. Wang *et al.*, Phys. Rev. Lett. **93**, 142501 (2004).
61. P. Mueller *et al.*, Phys. Rev. Lett. **99**, 252501 (2007).
62. M. Brodeur *et al.*, Phys. Rev. Lett. **108**, 052504 (2012).
63. A.A. Korsheninnikov *et al.*, Phys. Lett. B **316**, 38 (1993).
64. Y. Kanada-En'yo, H. Horiuchi, Prog. Theor. Phys. Suppl. **142**, 205 (2001).
65. Y. Kanada-En'yo, Phys. Rev. C **76**, 044323 (2007).
66. Y. Kanada-En'yo, H. Feldmeier, T. Suhara, Phys. Rev. C **84**, 054301 (2011).
67. T. Neff, H. Feldmeier, Nucl. Phys. A **738**, 357 (2004).
68. T. Neff, H. Feldmeier, R. Roth, Nucl. Phys. A **752**, 321 (2005).
69. P. Navrátil, B.R. Barrett, Phys. Rev. C **57**, 3119 (1998).
70. P. Navrátil, W.E. Ormand, Phys. Rev. C **68**, 034305 (2003).
71. P. Navrátil, densities from private communication.
72. H. Sagawa, Phys. Lett. B **286**, 7 (1992) Densities from Private communication.
73. H. Sagawa, Nucl. Phys. A **543**, 575 (1992).
74. K. Hagino, H. Sagawa, Phys. Rev. C **72**, 044321 (2005).
75. K. Hagino, H. Sagawa, T. Nakamura, S. Shimoura, Phys. Rev. C **80**, 031301 (2009).
76. K. Hagino, N. Takahashi, H. Sagawa, Phys. Rev. C **77**, 054317 (2008).
77. N.K. Timofeyuk, Phys. Rev. C **69**, 034336 (2004).
78. B.S. Pudliner *et al.*, Phys. Rev. C **56**, 1720 (1997).
79. R.B Wiringa, S.C. Pieper, J. Carlson, V.R. Pandharipande, Phys. Rev. C **62**, 014001 (2000).
80. E. Epelbaum, Prog. Part. Nucl. Phys. **57**, 654 (2006).
81. E. Caurier, P. Navrátil, W.E. Ormand, J.P. Vary, Phys. Rev. C **64**, 051301 (2001).
82. E. Caurier, P. Navrátil, W.E. Ormand, J.P. Vary, Phys. Rev. C **66**, 024314 (2002).
83. P. Navrátil, W.E. Ormand, Phys. Rev. Lett. **88**, 152502 (2002) and P. Navrátil, private communication (2004).
84. E. Caurier, P. Navrátil, Phys. Rev. C **73**, 021302 (2006).
85. A. Volya, V. Zelevinsky, Phys. Rev. Lett. **94**, 052501 (2005).
86. G. Hagen, M. Hjorth-Jensen, J.S. Vaagen, Phys. Rev. C **71**, 044314 (2005).
87. G. Papadimitriou, A.T. Kruppa, N. Michel, W. Nazarewicz, M. Ploszajczak, J. Rotureau, Phys. Rev. C **84**, 051304 (2011).
88. T. Myo, K. Kato, K. Ikeda, Phys. Rev. C **76**, 054309 (2007).
89. T. Myo, R. Ando, K. Kato, Phys. Rev. C **80**, 014315 (2009).
90. T. Myo, R. Ando, K. Kato, Phys. Lett. B **691**, 150 (2010).
91. T. Myo, A. Umeya, H. Toki, K. Ikeda, Phys. Rev. C **84**, 034135 (2011).
92. S. Baroni, P. Navrátil, S. Quaglioni, Phys. Rev. Lett. **110**, 022505 (2013).
93. A. Ozawa, T. Suzuki, I. Tanihata, Nucl. Phys. A **693**, 32 (2001).
94. G.D. Alkhazov *et al.*, Phys. Rev. Lett. **78**, 2313 (1997).
95. J.S. Al-Khalili, J.A. Tostevin, Phys. Rev. Lett. **76**, 3903 (1996).
96. J.A. Tostevin, J.S. Al-Khalili, Nucl. Phys. A **616**, 418c (1997).
97. J.S. Al-Khalili, J.A. Tostevin, Phys. Rev. C **57**, 1846 (1998).
98. J. Wurzer, H.M. Hofmann, Phys. Rev. C **55**, 688 (1997).
99. P. Descouvemont, C. Daniel, D. Baye, Phys. Rev. C **67**, 044309 (2003) and references therein.
100. A. Adahchour, P. Descouvemont, Phys. Lett. B **639**, 447 (2006).
101. K. Bennaceur, J. Dobaczewski, M. Ploszajczak, Phys. Lett. B **496**, 154 (2000).
102. A. Ong, J.C. Berengut, V.V. Flambaum, Phys. Rev. C **82**, 014320 (2010).
103. F.E. Wietfeldt, M. Huber, T.C. Black, H. Kaiser, M. Arif, D.L. Jacobson, S.A. Werner, Physica B **385**, 1374 (2006).
104. J.L. Friar, J. Martorell, D.W.L. Sprung, Phys. Rev. A **56**, 4579 (1997).
105. R. Pohl *et al.*, Nature **466**, 213 (2010).
106. E. Borie, G.A. Rinker, Phys. Rev. A **18**, 324 (1978).
107. I. Sick, Phys. Rev. C **77**, 041302 (2008).
108. The MUST Collaboration (Y. Blumenfeld *et al.*), Nucl. Instrum. Methods A **421**, 471 (1999).
109. The MUST2 Collaboration (E.C. Pollacco *et al.*), Eur. Phys. J. A **25**, 287 (2005).
110. W.N. Catford *et al.*, Nucl. Instrum. Methods A **614**, 439 (2010).

111. M.S. Wallace *et al.*, Nucl. Instrum. Methods A **583**, 302 (2007).
112. S. Ottini *et al.*, Nucl. Instrum. Methods A **431**, 476 (1999).
113. A. Lagoyannis *et al.*, Phys. Lett. B **518**, 27 (2001).
114. L. Giot *et al.*, Phys. Rev. C. **71**, 064311 (2005).
115. F. Skaza, V. Lapoux, N. Keeley, N. Alamanos, E.C. Pollacco, F. Auger, A. Drouart, A. Gillibert, D. Beaumel, E. Becheva, Y. Blumenfeld, F. Delaunay, L. Giot, K.W. Kemper, L. Nalpas, A. Obertelli, A. Pakou, R. Raabe, P. Roussel-Chomaz, J.-L. Sida, J.-A. Scarpaci, S. Stepantsov, R. Wolski, Phys. Rev. C **73**, 044301 (2006).
116. F. Skaza, N. Keeley, V. Lapoux, N. Alamanos, F. Auger, D. Beaumel, E. Becheva, Y. Blumenfeld, F. Delaunay, A. Drouart, A. Gillibert, L. Giot, K.W. Kemper, R.S. Mackintosh, L. Nalpas, A. Pakou, E.C. Pollacco, R. Raabe, P. Roussel-Chomaz, J.-A. Scarpaci, J.-L. Sida, S. Stepantsov, R. Wolski, Phys. Lett. B **619**, 82 (2005).
117. N. Keeley, F. Skaza, V. Lapoux, N. Alamanos, F. Auger, D. Beaumel, E. Becheva, Y. Blumenfeld, F. Delaunay, A. Drouart, A. Gillibert, L. Giot, K.W. Kemper, L. Nalpas, A. Pakou, E.C. Pollacco, R. Raabe, P. Roussel-Chomaz, K. Rusek, J.-A. Scarpaci, J.-L. Sida, S. Stepantsov, R. Wolski, Phys. Lett. B **646**, 222 (2007).
118. F. Skaza, V. Lapoux, N. Keeley, N. Alamanos, F. Auger, D. Beaumel, E. Becheva, Y. Blumenfeld, F. Delaunay, A. Drouart, A. Gillibert, L. Giot, E. Khan, L. Nalpas, A. Pakou, E. Pollacco, R. Raabe, P. Roussel-Chomaz, K. Rusek, J.-A. Scarpaci, J.-L. Sida, S. Stepantsov, R. Wolski, Nucl. Phys. A **788**, 260c (2007) article in preparation, for the detailed ^{8}He(p, p$'$) analysis.
119. X. Mougeot, V. Lapoux, W. Mittig, N. Alamanos, F. Auger, B. Avez, D. Beaumel, Y. Blumenfeld, R. Dayras, A. Drouart, C. Force, L. Gaudefroy, A. Gillibert, J. Guillot, H. Iwasaki, T. Al Kalanee, N. Keeley, L. Nalpas, E.C. Pollacco, T. Roger, P. Roussel-Chomaz, D. Suzuki, K.W. Kemper, T.J. Mertzimekis, A. Pakou, K. Rusek, J.-A. Scarpaci, C. Simenel, I. Strojek, R. Wolski, Phys. Lett. B **718**, 441 (2012).
120. R.L. Varner, W.J. Thompson, T.L. McAbee, E.J. Ludwig, T.B. Clegg, Phys. Rep. **201**, 57 (1991).
121. J.R. Beene, D.J. Horen, G.R. Satchler, Nucl. Phys. A **596**, 137 (1996).
122. M. Watson, Phys. Rev. **105**, 1338 (1957).
123. A.K. Kerman, H. McManus, R.M. Thaler, Ann. Phys. (NY) **8**, 551 (1959).
124. F.A. Brieva, J.R. Rook, Nucl. Phys. A **281**, 317 (1972).
125. J.P. Jeukenne, A. Lejeune, C. Mahaux, Phys. Rev. C **15**, 10 (1977).
126. J.P. Jeukenne, A. Lejeune, C. Mahaux, Phys. Rev. C **16**, 80 (1977).
127. J.S. Al-Khalili, F.M. Nunes, J. Phys. G: Nucl. Part. Phys. **29**, R89 (2003).
128. J.S. Petler *et al.*, Phys. Rev. C **32**, 673 (1985).
129. S. Mellema, R. Finlay, F. Dietrich, F. Petrovich, Phys. Rev. C **28**, 2267 (1983).
130. T. Tamura, W.R. Coker, R. Rybicki, Comput. Phys. Commun. **2**, 94 (1971).
131. J. Raynal, Phys. Rev. C **23**, 2571 (1981).
132. I.J. Thompson, Comput. Phys. Rep. **7**, 167 (1988).
133. N. Alamanos, F. Auger, B.A. Brown, A. Pakou, J. Phys. G **24**, 1541 (1998).
134. E. Khan *et al.*, Phys. Lett. B **490**, 45 (2000).
135. C. Jouanne, V. Lapoux, F. Auger, N. Alamanos, A. Drouart, A. Gillibert, G. Lobo, A. Musumarra, L. Nalpas, E. Pollacco, J.-L. Sida, M. Trotta, Y. Blumenfeld, E. Khan, T. Suomijärvi, T. Zerguerras, P. Roussel-Chomaz, H. Savajols, A. Lagoyannis, A. Pakou, Phys. Rev. C **72**, 014308 (2005).
136. V. Lapoux, N. Alamanos, F. Auger, V. Fékou-Youmbi, A. Gillibert, F. Marie, S. Ottini-Hustache, J.-L. Sida, D.T. Khoa, Y. Blumenfeld, F. Maréchal, J.-A. Scarpaci, T. Suomijarvi, J.H. Kelley, J.-M. Casandjian, M. Chartier, M.D. Cortina-Gil, M. Mac Cormick, W. Mittig, F. de Oliveira Santos, A.N. Ostrowski, P. Roussel-Chomaz, K.W. Kemper, N. Orr, J.S. Winfield, Phys. Rev. C **66**, 034608 (2002).
137. V. Lapoux *et al.*, Phys. Lett. B **517**, 18 (2001).
138. M.E. Brandan, G.R. Satchler, Phys. Rep. **285**, 143 (1997).
139. H. Feshbach, Ann. Phys. **5**, 357 (1958).
140. H. Feshbach, *Theoretical Nuclear Physics* (Wiley, New York, 1992).
141. Y. Sakuragi *et al.*, Prog. Theo. Phys. **70**, 1047 (1983).
142. Y. Sakuragi, Phys. Rev. C **35**, 2161 (1987).
143. A.A. Korsheninnikov *et al.*, Nucl. Phys. A **617**, 45 (1997).
144. R. Wolski *et al.*, Phys. Lett. B **467**, 8 (1999).
145. S.V. Stepantsov *et al.*, Phys. Lett. B **542**, 35 (2002).
146. V. Lapoux *et al.*, Phys. Lett. B **658**, 198 (2008).
147. N. Keeley, V. Lapoux, Phys. Rev. C **77**, 014605 (2008).
148. P. Navrátil, B.R. Barrett, Phys. Rev. C **54**, 2986 (1996).
149. S. Karataglidis *et al.*, Phys. Rev. C **61**, 024319 (2000).
150. T. Aumann *et al.*, Phys. Rev. C **59**, 1252 (1999).
151. K. Rusek, K.W. Kemper, R. Wolski, Phys. Rev. C **64**, 044602 (2001).
152. A.A. Korsheninnikov *et al.*, Phys. Rev. Lett. **82**, 3581 (1999).
153. A.A. Korsheninnikov *et al.*, Phys. Rev. Lett. **90**, 082501 (2003).
154. R.S. Mackintosh, Scholarpedia **7**, 12032 (2012) doi:10.4249/scholarpedia.12032 and references therein.
155. S. Raman, C.W. Nestor, Jr., P. Tikkanen, At. Data Nucl. Data Tables **78**, 1 (2001).
156. J. Jänecke *et al.*, Phys. Rev. C **54**, 1070 (1996).
157. S. Nakayama *et al.*, Phys. Rev. Lett. **85**, 262 (2000).
158. H. Akimune *et al.*, Phys. Rev. C **67**, 051302 (2003).
159. T. Nakamura *et al.*, Phys. Lett. B **493**, 209 (2000).
160. T. Nakamura *et al.*, Eur. Phys. J. A **13**, 33 (2002).
161. W. von Oertzen, Nucl. Phys. A **588**, 129c (1995).
162. H.G. Bohlen *et al.*, Prog. Part. Nucl. Phys. **42**, 17 (1999).
163. T. Nilsson *et al.*, Nucl. Phys. A **583**, 795 (1995).
164. K. Markenroth *et al.*, Nucl. Phys. A **679**, 462 (2001).
165. C. Romero-Redondo, S. Quaglioni, P. Navrátil, G. Hupin, Phys. Rev. Lett. **113**, 032503 (2014).
166. H. Sagawa, private communication; discussions in April 2015.
167. G.R. Jansen, M. Hjorth-Jensen, G. Hagen, T. Papenbrock, Phys. Rev. C **83**, 054306 (2011).
168. G.F. Bertsch, H. Esbensen, Ann. Phys. (NY) **209**, 327 (1991).
169. Y. Kikuchi, K. Kato, T. Myo, M. Takashina, K. Ikeda, Phys. Rev. C **81**, 044308 (2010).
170. K. Hagino, H. Sagawa, Phys. Rev. C **76**, 047302 (2007).
171. N. Keeley, K.W. Kemper, K. Rusek, Eur. Phys. J. A **50**, 145 (2014).

172. T. Suda, M. Wakasugi, Prog. Part. Nucl. Phys. **55**, 417 (2005).
173. A.N. Antonov *et al.*, Nucl. Instrum. Methods A **637**, 60 (2011).
174. E. Hiyama, T. Yamada, Prog. Part. Nucl. Phys. **63**, 339 (2009).
175. E. Hiyama, M. Isaka, M. Kamimura, T. Myo, T. Motoba, Phys. Rev. C **91**, 054316 (2015).
176. T.R. Saito *et al.*, Int. J. Mod. Phys. E **19**, 2656 (2010) doi: 10.1142/S021830131001723X.
177. H.-W. Hammer, A. Nogga, A. Schwenk, Rev. Mod. Phys. **85**, 197 (2013).
178. E. Epelbaum, H.-W. Hammer, Ulf-G. Meissner, Rev. Mod. Phys. **81**, 1773 (2009).
179. S. Bacca, A. Schwenk, G. Hagen, T. Papenbrock, Eur. Phys. J. A **42**, 553 (2009).
180. S. Bacca, N. Barnea, A. Schwenk, Phys. Rev. C **86**, 034321 (2012).
181. G. Hagen, N. Michel, Phys. Rev. C **86**, 021602 (2012).
182. M.H. Mahzoon, R.J. Charity, W.H. Dickhoff, H. Dussan, S.J. Waldecker, Phys. Rev. Lett. **112**, 162503 (2014).

Dr. Hab. Valérie Lapoux is a nuclear physicist working at CEA Saclay in the field of the direct nuclear reactions induced by radioactive beams. Most of her experimental works have been done since 2001 at the GANIL facility using the MUST2 array (`must2.cea.fr`) and also, since 2010, at RIKEN. Her works are focused on the interpretations of the reaction observables of the exotic unstable nuclei, in collaboration with theorists gathered in the framework of the ESNT laboratory (`esnt.cea.fr`), to obtain insight onto the nuclear forces at play to produce the fascinating structure properties of the atomic nucleus.

Dr. Nicolas Alamanos is Research Director at CEA Saclay. He has been Director of the Saclay Nuclear Physics Division and President of GANIL's Scientific Council. He is currently Deputy Director of the Institute of Research into the Fundamental Laws of the Universe (IRFU). He is a member of GANIL's Directorate committee, of GANIL/SPIRAL2 Scientific Council, Chairperson of the International Advisory Committee of the Institute of Nuclear and Particle Physics of "Demokritos", Scientific counselor of the European program "CEA-Euro talents", Secretary of the Joint (DSM-IN2P3) committee CCT-PNHE, Chairperson of the governing board of the European project "CHANDA", CEA representative member of (NuPECC). He is a member or evaluator of many committees —ANR (France), ARISTEIA (GRECE), FRS-FNRS (Belgium), STFC (England). He is a Member of many bilateral coordination committees, various steering, or In-Kind committees. From January 2013 he has been nominated Editor-in-Chief of the *European Physical Journal A* for the experimental physics section and Managing Reviews Editor for the experimental physics section. He is also the Editor of the Scholarpedia Encyclopedia of Nuclear Physics. Since 2009 He is a member of the GSI-GENCO community.